ARE FRACTALS WORTH THEIR SALT?

THE KOCH SNOWFLAKE RF SURFACE COIL: EXPLORING THE ROLE OF FRACTAL GEOMETRIES IN ^{23}NA-MRI

BY
CAMERON E. NOWIKOW, B.Eng.

A THESIS
SUBMITTED TO THE SCHOOL OF BIOMEDICAL ENGINEERING
AND THE SCHOOL OF GRADUATE STUDIES
OF MCMASTER UNIVERSITY
IN PARTIAL FULFILMENT OF THE REQUIREMENTS
FOR THE DEGREE OF
MASTER OF APPLIED SCIENCE

Master of Applied Science (2020) McMaster University
(Biomedical Engineering) Hamilton, Ontario, Canada

TITLE:	The Koch Snowflake RF Surface Coil: Exploring the Role of Fractal Geometries in ^{23}Na-MRI
AUTHOR:	Cameron E. Nowikow B.Eng. (Electrical & Biomedical Engineering), McMaster University, Hamilton, Canada
SUPERVISOR:	Dr. Michael D. Noseworthy
NUMBER OF PAGES:	x, 91

Abstract

Intra-cellular sodium (^{23}Na) concentration is directly related to cellular health. Thus, sodium magnetic resonance imaging (MRI) can provide metabolic information on tissue health that a routine clinical (proton) MRI cannot. ^{23}Na-MRI could be a valuable tool to assist physicians in the diagnosis, prognosis, and monitoring of a variety of pathologies. However, due to factors that include quantum mechanical limitations and biological restrictions, the signal-to-noise ratio (SNR) of a sodium scan is much lower than that of a standard proton scan, which limits the practicality of ^{23}Na-MRI in a clinical setting. This project looks to improve the viability of ^{23}Na-MRI and focuses on an often overlooked facet of MRI development, the radio frequency (RF) coil.

Fractal antennas have been used in telecommunication systems for years, and are generally exploited for their compact nature, allowing for the same performance of a larger antenna, in a smaller space. They have also been shown to be capable of a wider transmission bandwidth (BW) than a standard antenna and with MRI applications they have been shown to provide a small SNR increase in proton imaging. It is hypothesized that a surface coil with a Koch snowflake fractal geometry can provide increased SNR for a sodium MRI scan, compared to that of a standard circular geometry coil, by producing a more homogeneous magnetic field in both space and frequency.

To test the hypothesis two coils, one circular and the other a Koch snowflake fractal, were simulated. The simulated magnetic fields were compared on their homogeneity and magnitude before the two coils were constructed and implemented with a variety of sodium MRI scans. B_1^+ maps were acquired to measure RF field homogeneity, and SNR was determined for both coil geometries. The coils were also tested for their homogeneity over varied transmit BWs by comparing images with various field of view (FOV) sizes. Finally the coils were compared for clinical viability in a test of healthy human knee imaging.

The circular coil had a more homogeneous B_1^+ field than the fractal at depths between 10-40mm, and had a higher SNR in its produced images. The circular coil acquired more signal *in vivo* which provided a higher detail image, but the fractal coil's SNR was higher due to reduced noise. The fractal coil performed better over a wider BW which indicates that further research should be conducted into the applications of fractal coils in multi-nuclear MRI scans.

To Mom & Dad

Acknowledgements

First and foremost in my long list of thank yous, I would like to extend my utmost gratitude towards my supervisor Dr. Michael Noseworthy for not only letting me be a part of his lab, but for his continued support and guidance, lending countless opportunities to grow myself both academically and professionally. The second thank you goes to Dr. Natalia Nikolova for her never ending knowledge of simulation and her generosity in lending access to an necessary software license and a nonessential but welcome server which no doubt saved me endless hours of work. I would like to extend another big thank you to Norm Konyer for all of his help for all things RF and to everyone in the Imaging Research Centre who helped me along the way. I would also like to express my gratitude towards Dr. Pedram Yazdanbakhsh and as well to Cersensa Inc., along with MITACS, for funding for this project.

There are way, way too many of you to name everyone individually but a huge tip of the cap is in order for all my lab mates! You all made this thesis essentially worth writing. From sleeping on top of a bathroom in Montreal, to eleven hour road trips with no A/C in August, to almost getting absolutely negated by bikes in Rotterdam, to perhaps indulging in one (or two) too many drinks during scotch night, every one you guys all made my Master's really #RAD and honestly truly enjoyable. Thank you for all the insightful discussions and all the helpful advice. Specifically, a special thanks to Paul Polak for everything sodium related, I could not have done this without your help. And now to thank all my friends who've been here since the beginning, I could not do this without you guys! From the endless hours of COD, to hockey game into Sunday night fantasy football game, from beers and poutine before class, to our collective knowledge of absolutely nothing, y'all made grad school fun.

Finally, the biggest thanks of them all goes to my family and loved ones as, undoubtedly, without your continued love and support this two year Master's project wouldn't be at all possible.

Thank you all and cheers,

Cam

Contents

List of Figures

List of Tables

Chapter 1

Introduction

Sodium (symbol ^{23}Na) is the most abundant cation in the human body, existing usually as Na^+, and has been recognized as one of the most deterministic elements regarding the health of homeostasis in mammals [1]. The ion functions as an electrolyte and provides balance to the organism through osmoregulation and pH regulation [1, 2]. While the mechanisms behind sodium's role in homeostasis are complex, they can be understood through simple thermodynamics and osmosis. Water will move across the cell membrane, and between tissues, from areas of high water concentration (pure water), to areas of low concentration (water containing dissolved solute). With sodium being the main ionic solute in the body, it dictates where water should be in the tissue [3].

^{23}Na exists both intra and extra-cellularly, at concentrations of 10-15mM and 140-150mM respectively. The difference in sodium levels inside versus outside the cell results in a concentration gradient that is essential for cellular functionality and vitality. ^{23}Na is involved in cell physiology because of this trans-membrane gradient: in action potential propagation, muscular contractions, heart activity, and renal activity to name a few. Healthy cells maintain the sodium concentration gradient easily, but any changes to cell metabolism or any damage to the cell membrane will lead to increases in intra-cellular sodium concentrations [2]. This means sodium concentrations are very sensitive to the health of the cell and the integrity of its membrane. And it is this control of sodium concentration in the cell that directly indicates the health and vitality of the cell.

Sodium ions can transverse the cell membrane using several different mechanisms including [1–4]: Na^+ channels, Na^+/Ca^+ exchange, Na^+/H^+ exchange, Na^+/HCO_{3-} co-transporter, $Na^+/K^+/2Cl^-$ co-transporter, and Na^+/Mg^+ exchange. The most important mechanism in the maintenance of the gradient however, is the Na^+/K^+-ATPase.

Both an enzyme and an ion transporter, Na^+/K^+-ATPase, more commonly

known as the sodium-potassium pump (or sodium pump), is vital to the maintenance of the trans-membrane sodium concentration gradient as it is responsible for the bulk of the sodium ion removal from the intra-cellular compartment [1]. Using adenosine triphosphate (ATP) hydrolysis, the sodium pump can exchange three intra-cellular sodium ions for two extracellular potassium ions. The sodium pump is found within the membrane of every mammalian cell (and most eukaryotic cells) and the regulation of this large Na^+ (and K^+) concentration gradient is the largest energy expenditure of all cells sitting at around 30% for general cells and upwards to 70% for neurons [1, 3]. However, if the cellular demand for ATP exceeds the cellular production of ATP, or if there is abnormal sodium-potassium pump activity, intra-cellular sodium concentrations increase, which causes water to enter the cell increasing the osmotic pressure. The eventual result: cell death.

The functionality of the Na^+/K^+-ATPase, and the correlated sodium concentrations, have been linked to numerous pathologies [2, 5]. Using magnetic resonance imaging (MRI), it is possible to not only image the sodium in the body but even quantify it. ^{23}Na-MRI can provide direct biochemical information on tissue viability that other imaging modalities (including any standard clinical MRI) cannot. Sodium imaging can assist physicians in the diagnosis, prognosis, and monitoring of a variety of diseases and traumas including but not limited to [2, 5]:

- strokes,
- minor traumatic brain injuries (mTBI),
- tumors,
- degenerative brain disorders,
- mental illness,
- diabetes,
- osteoarthritis

^{23}Na-MRI is not without challenges, which therefore limits clinical use. In chapter 2 an explanation of the key obstacles associated with ^{23}Na-MRI is provided. The remainder of the thesis then focuses on possible solutions to getting ^{23}Na-MRI one step closer to clinical utility.

Chapter 2

Background

To explain the some of the obstacles of ^{23}Na-MRI, and the theory behind the proposed solution to these obstacles, a basic understanding of an MRI system is needed. An MRI scanner is composed of several complex subsystems, each with a unique function, that work in parallel to obtain an MR image. The four main subsystems of the scanner are the main magnet, the gradient system, the radio frequency (RF) system, and the control system. Each are necessary in their own right for an MRI to function as a viable imaging modality, however the MR signal begins and ends with the RF system.

The RF system is responsible for both the excitation and acquisition of the MR signal. When tissue enters the MRI it obtains a slight magnetization. The magnetization is induced in any atom that has the quantum mechanical property called spin (described in more detail below). Using an RF pulse from what is called an RF transmit (Tx) coil, we can cause the magnetization vector of the tissue to "tip" (i.e. energy gets absorbed by the tissues). Once tipped this magnetization is able to generate an RF signal of its own (as the energy gets released to the system) which can be detected by another RF coil, called an RF receive (Rx) coil. The signal detected by the Rx coil is the raw MR signal that, after some filtering and decimation, is used to generate images. The RF system is the first and last step towards obtaining an MR signal, which is why it is the focus of this project [6].

The remainder of this chapter provides more detail on the physics behind the generation/acquisition of the raw MR signal and how it pertains to the RF system. Additionally these details will be used in the context of imaging ^{23}Na as opposed to the clinical standard, ^{1}H (the proton).

It is important to note that there are two ways in which to describe the physics of MRI. Using quantum mechanics the whole of MRI can be explained, however it is math heavy and hard to conceptualize/visualize. Classic Newtonian mechanics can also be used, which is easier to visualize, but can only accurately describe around 95% of MRI. In this thesis the majority of the

explanations will be through classical mechanics, with a touch of quantum mechanics to explain the parts the classic description fails with.

2.1 Nuclei in a Magnetic Field

2.1.1 Quantum Spin

It is through the interaction between the main magnetic field of the scanner (denoted B_0) and select nuclei that creates this slight magnetization that tissue obtains when it enters the MRI. The only nuclei that interact with the field are ones with the quantum property called "spin". Quantum spin (or simply spin, denoted S) describes the intrinsic angular momentum of a particle and is a property of all fundamental particles (quarks, leptons, and force particles). Atomic nuclei are made up of protons and neutrons, both of which are made up of their own unique configuration of quarks. The collective spins of the quarks gives both protons and neutrons a spin of their own. If a nucleus has either an odd number of protons, an odd number of neutrons, or an odd number of both protons and neutrons, the nucleus will have the property of spin as well. The only nuclei without spin are the ones with an even number of both protons and neutrons [7].

Spin was determined to be a quantum value by Stern and Gerlach in the early 1920's, a few years before the concept of spin was even proposed by Uhlenbeck and Goudsmidt in 1925! For a more in-depth exploration of quantum spin than what follows please take a look at [7, 8]. Spin describes the set of discrete angular momenta that (in the case of MRI) the nucleus can occupy and those values are given by Equation 2.1.1:

$$S^2 = s(s+1)\hbar^2 \tag{2.1.1}$$

where $\hbar$ is the reduced Planck's constant ($\hbar = h/2\pi$), and s is the spin number of the nucleus ($s = 0, 1, 2, ...$ or $s = \frac{1}{2}, \frac{3}{2}, \frac{5}{2}, ...$). The spin number of a nucleus describes how many spin states it can occupy (# of spin states $= 2s + 1$). So if $s = \frac{1}{2}$, then the nucleus would have 2 spin states, meaning that nucleus has two different, but discrete values for its intrinsic angular momentum.

One of the consequences that arises from a nucleus having spin, is that the nucleus will also have an associated magnetic moment. The relationship between the spin vector ($\mathbf{S}$) and the associated magnetic moment ($\boldsymbol{\mu}$) is given by Equation 2.1.2 [8, 9]:

$$\boldsymbol{\mu} = \gamma \mathbf{S} = \gamma s \hbar \tag{2.1.2}$$

where γ is the gyromagnetic ratio of the nucleus. This ratio is a constant with units of rad/T·s and is another intrinsic property of nuclei with spin. Interestingly this constant has not been derived analytically, but only experimentally

determined. Just as there are different discrete values of angular momentum that a nucleus can occupy, there are discrete values paired with the magnetic moment of the nucleus, where the number of magnetic moment values are equal to the number of spin states.

Once placed inside an external magnetic field, nuclei with an associated magnetic moment will experience two processes [8]:

1. Zeeman Splitting
2. Precession

It is because of this magnetic moment that arises from spin that allows for nuclei to interact with an externally applied magnetic field. And from that interaction, it is possible to image the nuclei. If a nucleus has non-zero spin, and therefore a magnetic moment, it can (in theory) be visualized with an MRI. The most common nuclei to be imaged clinically using MRI is the hydrogen nucleus, or simply, the proton. And while it is overwhelmingly the most common, it is not the only viable nuclear option. Other nuclei having spin include deuterium (^{2}H), lithium (^{7}Li), nitrogen (both ^{14}N and ^{15}N), carbon (^{13}C), fluorine (^{19}F) and sodium (^{23}Na) also have spin (to name only a few). Since the hydrogen nucleus is both the clinical standard and has the easiest physics to explain (due to a an $s = \frac{1}{2}$), the following sections of the chapter will be focusing on proton MRI before ending the chapter with a section on how it differs when imaging sodium.

2.1.2 Zeeman Splitting

In the absence of an external magnetic field there is no discernible difference between the spin states of the nucleus. However, predictably, when a nucleus that has an associated magnetic moment enters the presence of the B_0 field, that magnetic moment will align with the field, either parallel or anti-parallel. In MRI the main field is arranged along the z-axis, in the direction of negative to positive, and so the magnetic moment of the nucleus will align either in the positive or negative z-direction.

$$\mathbf{B} = B_0\hat{z} \tag{2.1.3}$$

When a nucleus enters the B_0 field, energy is introduced into the system and creates an energy difference between the spin states. The spin states are referred to as either "spin up" or "spin down" and correlate to their alignment with the field. The lower energy spin state corresponds to the spin state that is parallel with the field, and the higher spin state is the state that is anti-parallel

to the field [8].

$$\Delta E = \hbar\omega_0 = -k_b T \ln \frac{P_{\text{m=-1/2}}}{P_{\text{m=+1/2}}} \tag{2.1.4}$$

For a spin 1/2 nuclei there are two energy states it can occupy when placed in a magnetic field. The ratio between the two states is described by a Boltzmann distribution which says that there are going to be a few more spins in the low energy state (i.e. aligned with the field) than in the high energy state (i.e. opposed to the field).

2.1.3 Precession

The potential energy that a magnetic dipole has in an external magnetic field is given by [8, 9]:

$$E = \boldsymbol{\mu} \cdot \mathbf{B} \tag{2.1.5}$$

From (2.1.2) we get the potential energy of the dipole:

$$E = \gamma s\hbar \cdot B_0 \tag{2.1.6}$$

If we take the proton which has a spin number of 1/2, the energy difference between the two spin states in an external magnetic field is equal to:

$$\Delta E = E_{\text{s=1/2}} - E_{\text{s=-1/2}} \tag{2.1.7}$$

$$\Delta E = \frac{1}{2}\gamma\hbar B_0 - (-\frac{1}{2}\gamma\hbar B_0) \tag{2.1.8}$$

$$\Delta E = \gamma\hbar B_0 \tag{2.1.9}$$

Combining (2.1.4) and (2.1.9) we get the expression:

$$\omega_0 = \gamma B_0 \tag{2.1.10}$$

Much like a spinning top when nudged, a nucleus with spin will start to precess around the field when placed inside a magnetic field. Because of the nuclear magnetic moment, the external magnetic field introduces a torque which causes this precession. The average magnetic moment of the nucleus is still aligned with the field. A key note is that the precession happens at a very specific frequency (which can be proven either through quantum or classical mechanics), which introduces the most important equation in MR physics, the Larmor equation (Equation 2.1.10) where ω_0 is the frequency of precession, called the *Larmor frequency*. This frequency is very important as

it is the frequency the the RF pulses need to be in order to generate the signal, and as well the NMR signal being detected is also at Larmor frequency. This equation also relates magnetic field to frequency and by spatially changing the magnitude of the magnetic field the equation then relates spatial position with frequency (more later).

2.1.4 The Magnetization Vector

The magnetization vector (denoted $\mathbf{M}$) is a way to make the quantum mechanical description of MRI "take a back seat", and move towards the more intuitive and simpler classical mechanical description. Both Zeeman splitting and precession play a role in the formulation of $\mathbf{M}$ and how it behaves. The magnetization vector of a sample of tissue is given by the averaging of all the magnetic moments produced by the nuclei in the volume and is given by [8]:

$$\mathbf{M} = \frac{1}{V}\sum_{V} \boldsymbol{\mu}_i \tag{2.1.11}$$

Looking back to Zeeman splitting and Equation 2.1.4, there is a relationship between the energy difference of the spin states, ΔE and the ratio between the two possible spin states, $P_{\text{m=-1/2}}/P_{\text{m=+1/2}}$. If this ratio is solved for a certain B_0, it can be shown that there will be a few more spins in the lower energy spin state (parallel with the field) as opposed to the higher energy spin state (anti-parallel with the field) and so the average of these spin states over a volume means that $\mathbf{M}$ is also aligned with the B_0 field. This ratio is called the Boltzmann distribution.

Much like the individual magnetic moments precess around the field, the magnetization vector precesses as well, at the Larmor frequency of the nucleus in question. And so $\mathbf{M}$ looks something like Figure 2.1. The angle between $\mathbf{M}$ and the vertical axis in reality is much smaller.

This is the beginning of the classical description of MRI, the averaging of all individual magnetic moments, and creating a net magnetization whose responses to a stimulus can be described using Newtonian mechanics like torque rather than more complicated energy levels.

2.2 Introducing the RF System

2.2.1 RF Pulses

The function of the RF system is to manipulate the magnetization vector ($\mathbf{M}$) of the tissue in order for the magnetization to be detected. At equilibrium, the $\mathbf{M}$ of the tissue in an MRI is aligned with the main B_0 magnetic field

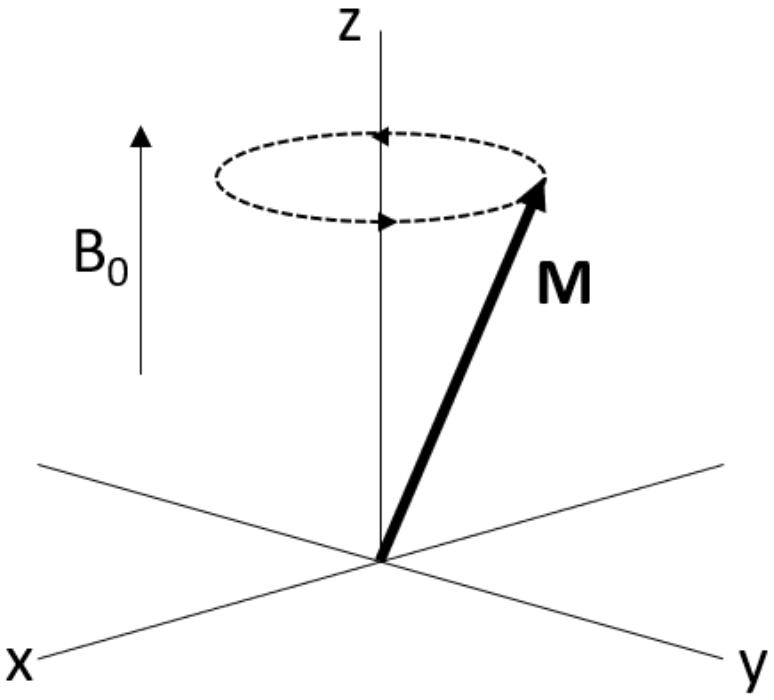

Figure 2.1: **Magnetization Vector** The precession of the magnetization vector (**M**) inside an external magnetic field (B_0)

which is by convention in the positive z-direction. For the magnetization to be detected, there needs to be a projection of the vector onto the xy-plane. The spins contributing to **M** can be excited by an RF pulse oscillating at the Larmor frequency, which allows their magnetization to be "tipped" into the transverse xy-plane. The RF pulse is a small magnetic field denoted B_1^+ and if it is either (i) on for long enough, or (ii) strong enough, the magnetization vector of the spins will stop aligning with the B_0 field and begin to align with the B_1^+ field. This has to do with the amount of energy being deposited into the tissue. We need to overcome the energy given by equation 2.1.4. The amount of energy deposited is proportional to the area under the curve of the RF pulse. The more energy, the further the magnetization tips, and this tip angle defined by the angle between **M** and the z-axis and is given by [10]:

$$\theta = \gamma \int_0^T B_1^+(t)dt \tag{2.2.1}$$

where θ is the tip angle in radians, T is the length of time of the pulse, and $B_1^+(t)$ is the envelope (i.e the shape) of the RF pulse. There are numerous

types of pulses that can be used in MRI experiments and an exploration into all of them would be quite lengthy and so for further discussion into all the types of RF pulses consult [10], as the following will only briefly introduce two kinds of pulses: the hard and soft pulse, as they are the most common and simplest. While there are advantages and disadvantages to all RF pulses, they all have unique defining characteristics in the form of a maximum amplitude, a pulse length, a bandwidth, and a slice profile.

The hard pulse is a RECT function in the time domain. Any pulse that is time varying is called a "soft" pulse. Hard pulses are generally used when no spatial selection is required as they have a large excitation bandwidth and an impractical slice profile (a SINC). They can have a very short pulse length and are ideal for 3D acquisitions [10].

The standard soft pulse used is a windowed SINC function in the time domain. These pulses are used far more often than a hard pulse because they are spatially selective as they have a narrow bandwidth with a clean rectangular slice profile which can reduce partial voluming effects in the resultant image. They tend to have a longer pulse length and a higher maximum amplitude than a hard pulse which may cause issues depending on the restrictive parameters of a particular MRI scan [10].

2.2.2 Relaxations and the Bloch Equations

As the RF pulse is applied the magnetization vector tips down from the z-axis towards the xy-plane, however it is still oscillating at the Larmor frequency and so the path the vector takes is a nutating spiral as it continues to oscillate as it tips. Once there is any component of the magnetization vector projected on to the xy-plane, the magnetization can be detected, however only once the RF pulse is turned off due to the strength of the signal that is generated by the magnetization is orders of magnitude smaller than the RF pulse power (about 10,000 times smaller).

Once the RF pulse is turned off and the magnetization vector has been tipped, due to simple thermodynamics (energy has been put into the system, and that energy needs to be dissipated by the system), the magnetization vector will tend to "relax" back to thermal equilibrium. There are two mechanisms that contribute to the magnetization going to equilibrium; longitudinal and transverse relaxation.

Longitudinal relaxation, also called spin-lattice relaxation, is the process of the magnetization vector "recovering" from the transverse xy-plane back to the z-axis to re-align with the B_0 field. As time progresses after the termination of the RF pulse, at which magnetization in the transverse plane is maximal, the projection of $\mathbf{M}$ in the transverse plane decreases. This recovery process is independent of the Larmor frequency and can be modeled as the differential

equation (2.2.2),

$$\frac{dM_z}{dt} = \frac{1}{T_1}(M_0 - M_z) \tag{2.2.2}$$

where M_0 is the net magnetization, M_z is the magnetization in the z-direction, and T_1 is the time constant that describes the rate of relaxation.

Transverse relaxation, also called spin-spin relaxation, is a process that exists solely in the transverse xy-plane and is due to the interactions of spins with each other, as well as the inhomogeneities of the external B_0 field. The individual magnetic moments of the spins interact with one another, tugging and pulling the adjacent magnetic moments near them. From the Larmor equation (2.1.10), the oscillation frequency of the individual magnetic moments are directly proportional to the field strength that is being experienced by the nucleus. Due to a wide array of factors, the B_0 field is not perfectly homogeneous in any one location, resulting in a range of oscillation frequencies inside a volume. Since the magnetization vector is an average, its frequency will tend towards B_0, but the individual spins will be at different frequencies. These two interactions in a finite length of time will resemble the spins dephasing from one another. As time progresses the individual magnetic moments will dephase, resulting in a "fanning out" of magnetic moments. On a macroscopic scale, this means the net magnetization in the transverse plane will be reducing as the spins spread out equally in all directions in the xy-plane resulting in the reduction in the net magnetization vector. If we define our transverse magnetization as:

$$\mathbf{M}_T = M_x\hat{x} + M_y\hat{y} \tag{2.2.3}$$

The transverse magnetization can be related to the relationship between the angular momentum of a magnetic moment and an external magnetic field, and incorporating a decay rate brought on by the dephasing spins (given by T_2) into the equation the differential equation that describes transverse magnetization is:

$$\frac{d\mathbf{M}_T}{dt} = \gamma\mathbf{M}_T \times \mathbf{B} - \frac{1}{T_2}\mathbf{M}_T \tag{2.2.4}$$

Combining (2.2.2) and (2.2.4) we get the expression that describes the magnetization vector after the RF pulse turns off:

$$\frac{d\mathbf{M}}{dt} = \gamma\mathbf{M} \times \mathbf{B} + \frac{1}{T_1}(M_0 - M_z)\hat{z} - \frac{1}{T_2}\mathbf{M}_T \tag{2.2.5}$$

This equation is known as the Bloch equation and can be broken down into x, y, and z components before being solved to describe the kinetics of the magnetization vector after an RF pulse. Note that this is assuming a static

field in the z direction.

$$\frac{dM_z}{dt} = \frac{(M_0 - M_z)}{T_1} \tag{2.2.6}$$

$$\frac{dM_x}{dt} = \omega_0 M_y - \frac{M_x}{T_2} \tag{2.2.7}$$

$$\frac{dM_y}{dt} = -\omega_0 M_x - \frac{M_y}{T_2} \tag{2.2.8}$$

With the bounds that $M_z(\infty) = M_0$ and $M_x(\infty) = M_y(\infty) = 0$ the Bloch equations can be solved resulting in:

$$M_z(t) = M_z(0)e^{-\frac{t}{T_1}} + M_0(1 - e^{-\frac{t}{T_1}}) \tag{2.2.9}$$

$$M_x(t) = e^{-\frac{t}{T_2}}(M_x(0)\cos\omega_0 t + M_y(0)\sin\omega_0 t \tag{2.2.10}$$

$$M_y(t) = e^{-\frac{t}{T_2}}(M_y(0)\cos\omega_0 t - M_x(0)\sin\omega_0 t \tag{2.2.11}$$

where $M_z(0)$ relates to the net magnetization M_0 by the cosine of the tip angle θ and $M_x(0) + M_y(0)$ relate to the net magnetization through the sine of the tip angle. Both relaxation processes are not mutually exclusive, they are both happening at the same time and contribute to the signal strength at any time, t.

2.2.3 Signal Detection and the FID

Both T_1 and T_2 relaxation times are measured in milliseconds and can be experimentally determined. Different tissues have different relaxation times and as a result will change the signal strength of their respective tissue in the MRI image, which provides the unique MRI contrast. The raw MR signal is a mixture of all the magnetization vectors in the imaged object, and different tissues have different relaxation times as well as spin densities, which means when the signal is sampled at a given time $t = \tau$, every tissue will have a different magnetization vector and therefore a different signal - all of which are mixed together to form something called a free induction decay (FID) signal.

From Faraday's Law of Induction, an electromotive force (emf) is induced in a coil through which there is a changing magnetic flux. The magnetization vector of our tissue is a kind of oscillating magnetic field, (denoted B_1^-) and if there is a coil perpendicular to the main magnetic field, a voltage will be

induced in it once the RF pulse stops.

$$emf = -\frac{d\Phi}{dt} \tag{2.2.12}$$

where Φ is the magnetic flux through the coil and is defined as an integral of the magnetic field over the surface area of the coil.

$$\Phi = \int_{coil\ area} \mathbf{B} \cdot d\mathbf{S} \tag{2.2.13}$$

To relate this to MRI, it needs to be shown how the magnetization vector has an associated magnetic field. This arises from the concept of effective current density:

$$\mathbf{J}_M(\mathbf{r}, t) = \boldsymbol{\nabla} \times \mathbf{M}(\mathbf{r}, t) \tag{2.2.14}$$

From the effective current density, a vector potential can be found:

$$\mathbf{A}(\mathbf{r}) = \frac{\mu_0}{4\pi} \int d^3r' \frac{\mathbf{J}(\mathbf{r}')}{|\mathbf{r} - \mathbf{r}'|} \tag{2.2.15}$$

And from that a magnetic field can be calculated:

$$\mathbf{B} = \boldsymbol{\nabla} \times \mathbf{A} \tag{2.2.16}$$

Through Stoke's Theorem, and the manipulation of equations it can be shown the the resultant emf which is the voltage of the raw signal is given by:

$$emf = -\frac{d}{dt} \int_{sample} d^3r \mathbf{M}(\mathbf{r}, t) \cdot \mathfrak{B}^{receive}(\mathbf{r}) \tag{2.2.17}$$

Knowing how the magnetization vector behaves after an RF pulse inside a constant external field we get an expression for our raw MR signal (please refer to [8] for a full derivation):

$$s(t) \propto \omega_0 \int d^3r M_-(\mathbf{r}, t) \mathfrak{B}^*_-(\mathbf{r}) \tag{2.2.18}$$

where M_- is the complex transverse magnetization and $\mathfrak{B}_-$ is the complex magnetic field induced in the coil. As the transverse magnetization is oscillating at the Larmor frequency, the resultant signal will also be oscillating at the Larmor frequency. The resultant signal obtained by what is known as a "pulse-acquire" sequence (i.e. the most basic of all MRI experiments) where after application of an RF pulse the resultant exponentially deacaying envelope is known as an FID and resembles Figure 2.2. The FID is a decaying exponential modulated with the Larmor frequency. This signal is a mixture of all magnetization vectors present in the tissue being probed, and so while

generally the signal is at Larmor frequency, there is modulation (due to T_2 interactions) as not all the spins are exactly at Larmor frequency. The slower the decay constant the longer the FID (and hence the longer the T_2, while when decay is rapid the FID is short leading to rapid loss of signal amplitude (i.e. for short T_2s). A further addition to this loss of phase coherence occurs when the magnetic field homogeneity is reduced (i.e. increased ΔB_0). The contribution of both T_2 and ΔB_0 is reflected in a parameter called T_2*:

$$\frac{1}{T_2{}^*} = \frac{1}{T_2} + \gamma \Delta B_0 \tag{2.2.19}$$

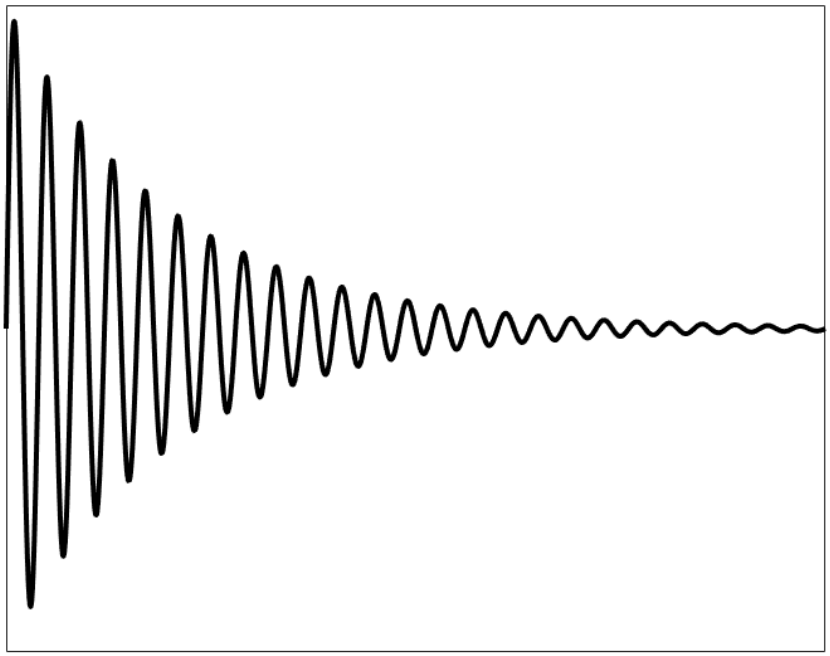

Figure 2.2: **Free Induction Decay Signal** The free induction decay (FID) signal induced in a coil from a simple MR experiment

2.3 Radio Frequency Coils

2.3.1 Design and Characterization

The RF system is composed of a control unit, a pulse generator, multiple amplifiers, transmit/receive switches, ADCs and DACs, but the components

of the RF system that are directly involved in the transmission of the RF pulse and then the detection of the MR signal are the RF coils. The coils themselves are essentially just antennas, as they send and receive signals, and are called "RF" coils because they work in the radio frequency range (widely defined as 20kHz to 300GHz). There are many types of coils used in MRI including solenoid and saddle coils but the three main types of coils most frequently used are the surface coil, birdcage coil, and phased-array coil, each with their own applications [6, 11].

The simplest coils are transmit/receive types consisting of a copper loop (the most common are loops however they can also be monopoles or dipoles) with a selection of soldered capacitors connected to a $\lambda/2$ coaxial cable, while the more complicated coils are receive-only with multiple elements complete with built-in pre-amplifiers, active and passive detuning circuits, inductors, and multiple channels.

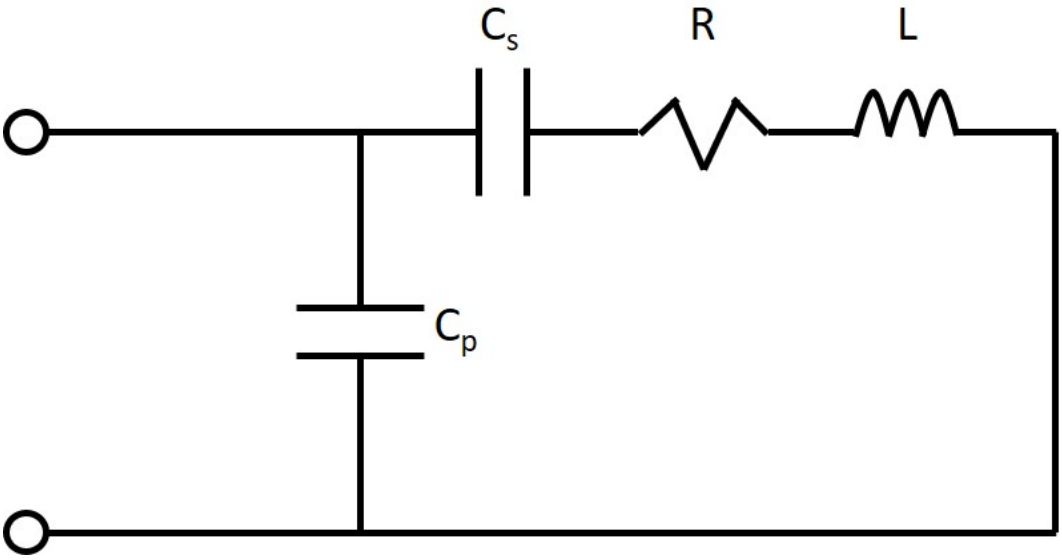

Figure 2.3: **A simple RLC Circuit** An RF coil is essentially an RLC circuit with a parallel capacitance C_p, a series capacitance C_s, a resistance R, and an intrinsic inductance L.

Any RF coil stripped of its "bells and whistles" is just an RLC circuit with two resonant frequencies given by:

$$\omega_1 = \frac{1}{\sqrt{LC_s}}, \qquad \omega_2 = \sqrt{\frac{C_p + C_s}{LC_pC_s}} \tag{2.3.1}$$

Of note, this applies to the simplest type of coil, the surface coil. Volume coils such as birdcage coils have multiple nodes leading to more complex

designs beyond the scope of this thesis. The resonant frequencies are the wavelengths that the coil is sensitive to. Based on constructive and deconstructive interference, the resonant frequencies are the frequencies where the phase is zero at both "nodes" of the circuit so that the signals don't cancel each other out but rather add together. Frequencies outside of the resonant frequencies tend to cancel each other out when they propagate through the circuit, leaving no signal exiting the circuit.

2.3.2 Tuning and Matching (S and Z parameters)

For a RF coil to be effective in an MRI experiment it needs to be tuned to the Larmor frequency of the nucleus being probed (see equation 2.1.10). That is to say that $\omega_1 = \omega_0$. Generally the second resonant frequency ω_2 is ignored as it is more challenging to work with (it won't cause any interference either as it tends to be a lot larger than ω_1 and is outside of the bandwidth of ω_1).

In order to experimentally determine the resonance of a circuit, a vector network analyzer (VNA) is required. This system is used to determine and display the network characteristics of the circuit connected to it. The two characteristics that are beneficial to determine in MRI RF coil design are called scattering and impedance parameters. They can be determined for multi-port networks, but the following description of these parameters for simplicity's sake is going to be of single-port networks (i.e. a surface coil). For a further discussion of impedance and scattering parameters of multiple port networks please consult [12] (although the premise can be easily enough extrapolated). The VNA can calculate these parameters over a range of frequencies and from these parameters the resonance of the circuit can be identified.

Scattering Parameters

Scattering parameters (also called s-parameters) are defined as (2.3.2) and describes the so-called scatter (S, not to be confused with quantum spin), or reflectance of the voltage that enters the port (V^-) versus the voltage that gets reflected back from the port (V^+).

$$V_1^-(\omega) = S_{11}(\omega)V_1^+(\omega) \tag{2.3.2}$$

In the case of the RLC circuit that is the RF coil, ω_1 can be determined as it has the frequency where the s-parameter is minimal (ideally 0). This means that at ω_1 the circuit allows the majority of the signal through the port (i.e. resonance). It is the goal of the coil designer to get $S_{11}(\omega_1 = \omega_0) < -10\text{dB}$ to say that the coil is on resonance at the Larmor frequency.

Impedance Parameters

Resonance is not the only important characteristic that needs determined. The other is impedance which, unless you are proficient at reading Smith charts, is difficult to obtain from an s-parameter plot. Impedance parameters (also called z-parameters) are defined as (2.3.3) and relates the voltage of a port (V) to its current (I), effectively describing the impedance "seen" by the port.

$$V_1(\omega) = Z_{11}(\omega)I_1(\omega) \tag{2.3.3}$$

By definition, resonance of a circuit is when the phase of the impedance of the circuit is 0°. This means, as previously mentioned, that there is no deconstructive interference of the signal at that frequency. The resonant frequency of the RLC coil is such that $\angle Z_{11}(\omega_1) = 0°$.

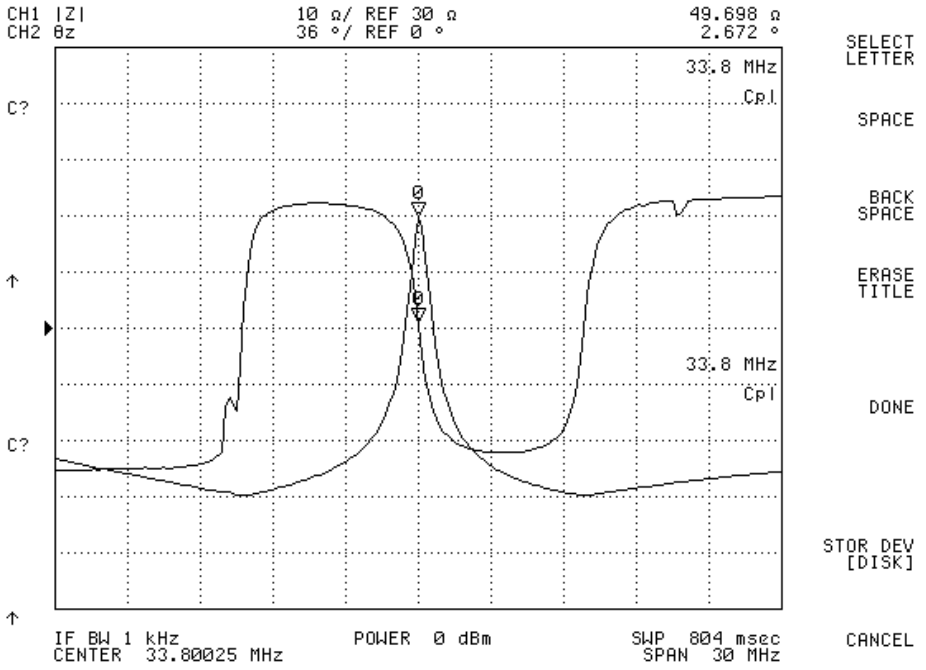

Figure 2.4: **Sample $\mathbf{Z_{11}}$ Parameter Plot** Taken from a VNA, showing the z_{11} of a coil tuned to 33.8MHz

But as stated, resonance is not the only important characteristic. The coil needs to be connected to the MRI somehow and generally that is through a coaxial cable. There needs to be minimal reflectance of the signal from the

coil to the cable and vice versa, which requires impedance matching between the cable and coil. Both the MRI and coaxial cable have a characteristic impedance of 50Ω and so the coil needs to be matched to 50Ω as well. To determine the characteristic impedance of a circuit at resonance, the magnitude of the impedance can be looked at, and the goal of the coil designer is to get $|Z_{11}(\omega_0)| = 50\Omega$.

Figure 2.4, shows a typical z-parameter display from a VNA, where the curve with the sharper peak is the magnitude and the wavey curve is the phase. Resonance is where there is a zero-crossing in phase (there will usually be multiple), and where there is a high impedance magnitude peak so that reflectance from the coaxial cable is minimized. In this sample case, the zero-crossing with a 50Ω peak is at 33.8MHz. (Note S_{11} can be calculated from the z-parameters (normalized to source impedance): $S_{11} = \frac{Z_{11}-1}{Z_{11}+1}$) [12].

2.3.3 B_1^+ Field of a Surface Coil

Of the three types of RF coils, surface coils are the simplest as they consist of a single element (usually a loop) with no pre-amplifiers or detuning circuits as they tend to be transmit/receive. They are easier to tune and match as there is no coupling between elements, and they also tend to be smaller which requires fewer capacitors and ultimately less soldering.

The nature of the surface coil is that it produces a very local, but heterogeneous B_1^+ field that drops off quickly ($\sim$ within a radius) as you move away from the coil plane. This can be shown through the derivation of the local magnetic field produced by a surface coil. Consider a current loop in the xz-plane of radius R, with its axis pointing in the positive y-direction. Using Biot-Savart's Law the field along any point on the y-axis from an element of current is given by:

$$d\mathbf{B} = \frac{\mu_0 I d\mathbf{L} \times \mathbf{r}}{4\pi r^3} \tag{2.3.4}$$

Both the dB_x and dB_z rotate around the y-axis as the current moves, and this leads to a net field of 0 in both the x- and z-direction, and so only dB_y is needed to be solved for.

$$dB_y = \frac{\mu_0}{4\pi}\frac{I}{r^3} dL \sin\theta \tag{2.3.5}$$

By substituting $\sin\theta = \frac{R}{\sqrt{y^2+R^2}}$ and integrating we get the magnetic field at any point along the y-axis:

$$B_x = B_z = 0 \tag{2.3.6}$$

$$B_y = \frac{\mu_0}{2} \frac{R^2 I}{(y^2 + R^2)^{\frac{3}{2}}} \tag{2.3.7}$$

As shown in (2.3.7), $B_y \propto \frac{1}{y}$ which means as you move away from the loop, the field strength reduces, which results in an intrinsic heterogeneous magnetic field. For a derivation of the magnetic field at any given point $P(x, y, z)$, consult [11], but the result of a reduced field over distance remains the same.

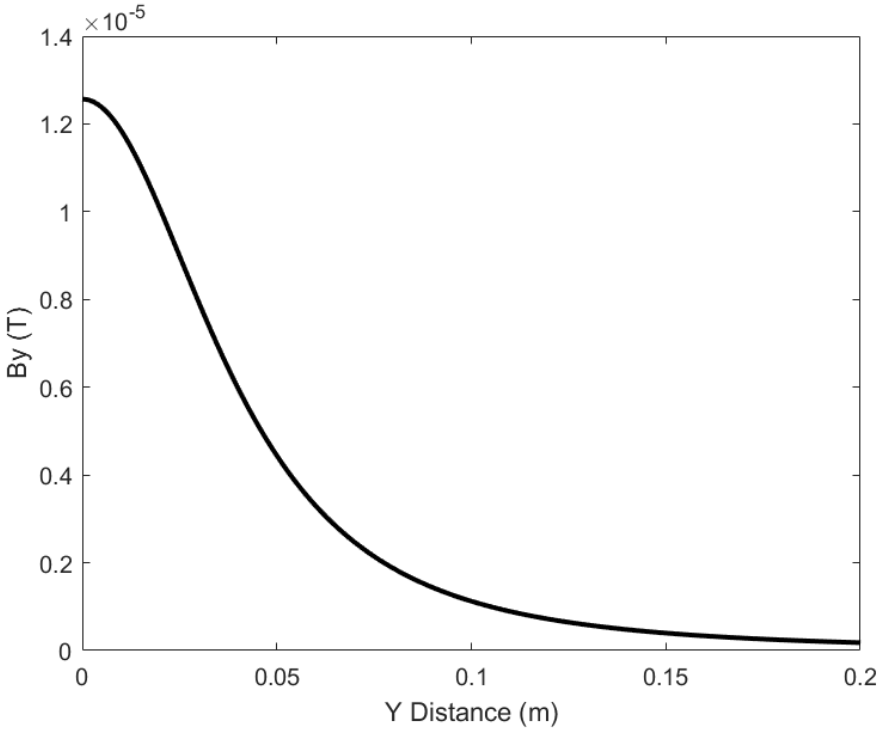

Figure 2.5: **Field of a Surface Coil** The field of a surface coil as modelled by Equation 2.3.7 for a coil with a 5cm radius, carrying a current of 1 Ampere.

2.4 Pulse Sequences and K-Space

Up until this point, an MRI experiment consists of pulsing RF into the subject/patient inside a static external magnetic field, and detecting the resultant signal produced by the magnetization of the subject. While this returns an FID, it is not an image. To obtain an image in MRI, something called a pulse sequence is applied. A pulse sequence consists of four main components:

1. RF Excitation Pulse

2. Slice Selection Gradient
3. k-space Navigation Gradients
4. Readout Gradient and Signal Detection/Sampling

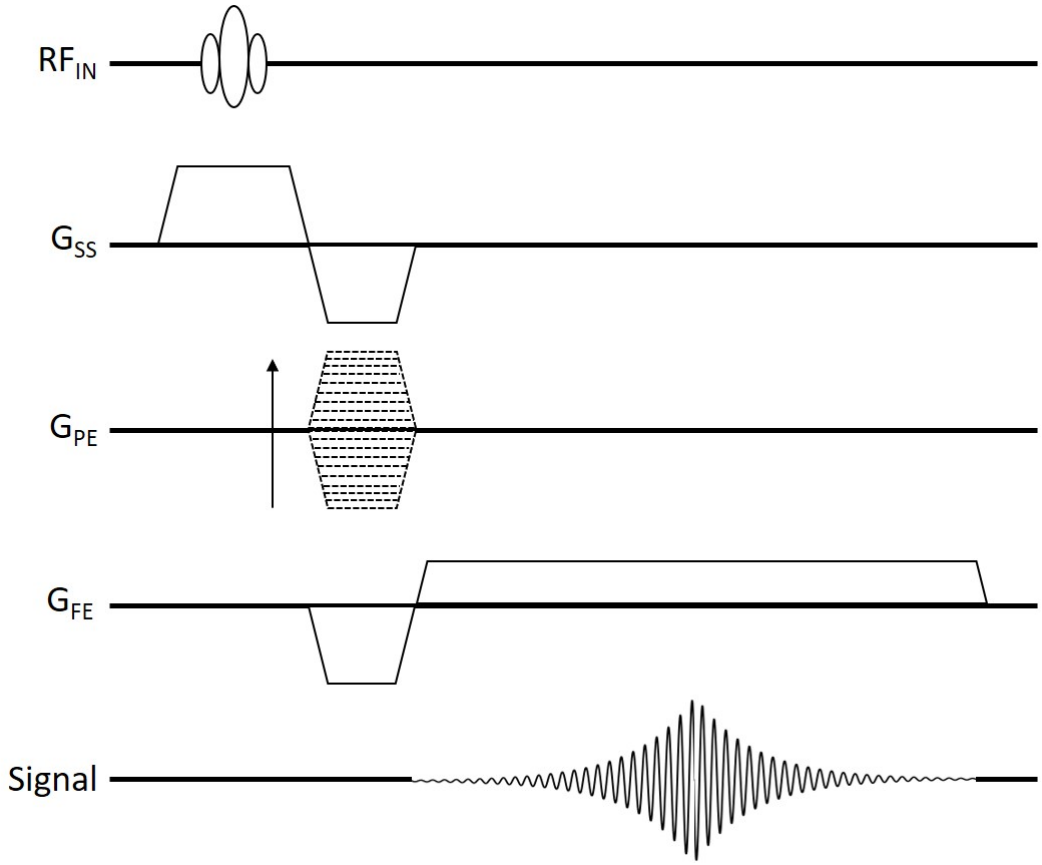

Figure 2.6: **Generalized Pulse Sequence** The standard pulse sequence has all of these components. This particular example is that of a 2D gradient echo pulse sequence.

The excitation RF pulse and slice selection gradient occur concurrently and are responsible for spatially localizing the spins in a slice of interest. The navigation gradients (called frequency encoding (FE) and phase encoding (PE) gradients) allow the sequence to "fill" data space called k-space (discussed in further detail later), and lastly the readout gradient (also by convention called a frequency encoding gradient) is applied during signal sampling to fill k-space with the raw MR signal.

2.4.1 Spatial Localization

If tissues within a MRI scanner are pulsed with RF and a readout is immediately applied to sample the FID no image will result. This would simply result in an NMR spectrum of the entire sensitive volume within the scanner. Spatial localization is required, which is done through the application of three orthogonal magnetic field gradients.

Application of gradients is a way to encode desired spatial features within the phase and frequency information of the MRI signal. From the Larmor equation (2.1.10), the frequency of the signal will change with field strength. The signal can then be localized to a sample of tissue as opposed to the entire volume. As an example, consider a linear magnetic field gradient (given in units of mT/m, or more generally field amplitude per unit distance) applied in the direction of the B_0 field which results in a field:

$$B_z(z) = B_0 + zG_z \tag{2.4.1}$$

This results in spatially localized Larmor frequencies in the z-direction:

$$\omega(z) = \omega_0 + \gamma z G_z \tag{2.4.2}$$

This gradient, combined with a RF pulse that has a specified transmit bandwidth $\Delta\omega_{RF}$ results in a "slice" of tissue Δz that gets excited as opposed to the whole volume:

$$\Delta\omega_{RF} = \omega_2 - \omega_1 \tag{2.4.3}$$

and from (2.4.2):

$$\Delta\omega_{RF} = (\omega_0 + \gamma z_2 G_z) - (\omega_0 + \gamma z_1 G_z) \tag{2.4.4}$$

$$\Delta\omega_{RF} = \gamma G_z(z_2 - z_1) \tag{2.4.5}$$

This results in slice size of:

$$\Delta z = \frac{\Delta\omega_{RF}}{\gamma G_z} \tag{2.4.6}$$

Generally, during slice selection, the bandwidth of the RF pulse is fixed. This is either because a specific pulse is needed for the MRI experiment, or because of system safety limits. Therefore, the strength of the gradient (i.e. slope) is altered to achieve a desired slice thickness (i.e. image resolution in the z-direction). Only spins within the selected slice are detected.

2.4.2 Introduction to K-Space

The purpose of the PE and FE gradients are to "navigate" through data space (called k-space). Once the slice has been selected the goal of the PE and FE gradients is to permit sampling of all desired locations within k-space. K-space represents the spatial frequencies within the location being imaged. In the case of a simple single slice 2D gradient echo pulse sequence (Fig. 2.6) k-space represents the 2D spatial frequencies inside the slice of tissue that was excited. Much like a 1D signal in time can be decomposed into its sinusoidal components, a 2D image can be decomposed into its 2D sinusoidal components which are just sine waves propagating over an angle through the centre (i.e. zero point). The sine waves that make up an image can be summarized in a 2D matrix with coefficients that represent the magnitude and phase of the wave at each direction (represented by the vector from the origin of k-space to the location in the matrix). It should be noted that the centre of k-space has the maximal signal. This represents the bulk energy of the image, or the low spatial frequency information of the slice.

Most pulse sequences do not acquire data as FIDs. The gradients are used to "refocus" the signal as an "echo". This can been seen in the basic pulse sequence (Fig. 2.6). For the basic sequence an echo is preferred to effectively provide enough time to spatial encode the data and fill k-space. FID-based acquisitions are used when T_2s are very short, or when wants to take advantage of the conjugate symmetry of k-space to accelerate image acquisition.

Once a slice is selected the PE gradient is incremented in magnitude over multiple steps and each step is followed with a frequency encoding gradient readout (and concurrent application of the ADC to digitize incoming data). The beginning of encoding a slice is always the centre of k-space. A negative x- or y-gradient takes the system to -ve x or y, respectively in k-space. The reciprocal is true for a positive magnitude gradient. To fill a slice, using the example of the basic pulse sequence, the sequence is applied incrementally until the slice is filled. Image resolution is dictated by number of PE steps and the readout bandwidth. SO, if there are 256 phase encoding steps with 256 points along the FE gradient then the resultant image is 256x256. The units of k-space are 1/cm.

This results in a signal in k-space that looks like this (in a 2D slice):

$$s(k_x, k_y) = \int_x \int_y m(x, y) e^{-i2\pi(k_x x + k_y y)} dx dy \tag{2.4.7}$$

where

$$k_x = \frac{\gamma}{2\pi} \int_0^{t_x} G_x(\tau_x) d\tau_x, \qquad k_y = \frac{\gamma}{2\pi} \int_0^{t_y} G_y(\tau_y) d\tau_y \tag{2.4.8}$$

This signal in k-space is just the Fourier transform of the image $m(x, y)$ and so to obtain the image back from k-space an inverse Fourier transform integral can be used:

$$m(x, y) = \int_x \int_y s(k_x, k_y) e^{i2\pi(k_x x + k_y y)} dk_x dk_y \tag{2.4.9}$$

2.4.3 K-Space Trajectories and Pulse Sequences

The gradients, pulses, and their timings can all be altered in order to obtain different contrasts and to optimize certain aspects of the sequence (length of time, signal, resolution, etc.). By adjusting gradient timing after the RF pulse will change how much the spins dephase due to T_2 (i.e. recall the longer one waits to sample the more signal dephasing has occurred). This timing is called the echo time (TE). By adjusting the timing of the next increment of the PE gradient effectively selects how many spins have returned to thermal equilibrium along the Z-direction (i.e. parallel to B_0). In other words the number of spins recovered due to T_1 relaxation. This timing is called the repetition time (TR).

By changing pulse sequence TE and TR image contrast is modulated due to the varied T_1 and T_2 times between tissue types. By having a short TE and short TR the primary contrast is derived from the differences in T_1 times between tissues, whereas if both the TR and TE are long the contrast is primarily due to the differences in T_2 times between tissues. An additional kind of contrast can be produced if the TE is short and the TR is long, and this will produce a contrast based off of the spin density of the tissue.

The gradients do not have to be implemented in the way shown in Fig. 2.6, there are many 2D and 3D acquisitions with varying numbers of RF pulses and varied RF pulse types. In addition, although most pulse sequences are acquired in a rectilinear fashion (to be able to take advantage of the Fourier transform) it is not a necessity. Some sequences increment in spokes and can take advantage of the Radon transform, or filtered back projection to do image reconstruction (like CT scanning). Also, non-Cartesian sequences can be applied and data then reconstructed to image space using a non-uniform Fast Fourier transform (NUFFT). Since gradients "move" around k-space the different patterns and implementations of the gradients are named "k-space trajectories". Each trajectory has its own purpose, whether to be optimized for speed, resolution, or signal. Generally k-space trajectories act in a Cartesian system as it allows for simple image reconstruction but non-Cartesian trajectories can also be implemented including spiral, radial, and pseudo random type trajectories.

2.5 The Challenges of ^{23}Na-MRI

Sodium is a quadrupolar nucleus (spin 3/2) with a gyromagnetic ratio of 11.262 MHz/T. The 3/2 spin results in four energy levels that the sodium spins can occupy and six transition states (ΔE's). The quadrupolar nature allows the nucleus to interact with the electronic configuration of its molecular environment in a variety of ways. ^{23}Na exists in four main types of environments, (type-a) crystal-like, (type-b) powder-like, (type-c) semi-solid, (type-d) aqueous, where each environment provokes a unique NMR response from the sodium nuclei [2, 13]. In the semi-solid regime (i.e. biological tissues), this interaction results in a biexponential T_2 relaxation, where the short T_2 is on the order of 0.5-5ms which is on the order of one magnitude smaller than the T_2 values of the proton in various tissues. Table 2.1 shows the T_2 values of some tissues at 3T of sodium and the proton.

Tissue	$T_{2,proton}$ (ms)	$T_{2,short}$ (ms)	$T_{2,long}$ (ms)
Brain WM	56-69	0.8-3	15-30
Brain GM	71-99	0.8-3	15-30
CSF	171-200	–	55-65
Cartilage	27-45	0.5-2.5	10-30
Muscle	32-50	1.5-2.5	15-30

Table 2.1: **T_2 Values of Various Tissues at 3T** The T_2 values of the proton and the sodium nucleus for a variety of tissues at 3T. Values taken from [2, 14, 15].

Due to this short biexponential T_2 relaxation, the MR signal decays away quite fast and to be able to image before there is no signal, ultrashort echo time (UTE) pulse sequences are required to acquire the data. While a gradient echo sequence with a non-selective hard pulse can be used to get a TE of $\sim$ 2-4ms, to get TE times less than one millisecond k-space navigation must be altered.

Some common methods to transverse k-space more quickly are radial stack of stars, radial projection reconstruction (PR), 3D cones or twisted projection imaging (TPI) [16–18]. However, with the non-Cartesian methods of k-space trajectories, alternate approaches to image reconstruction are needed as the standard Fourier transform cannot be directly used. The traditional method is to re-grid the data onto a Cartesian system before using a standard fast Fourier transform (FFT), but recently a more common method of using a non-uniform fast Fourier transform (NUFFT) has been implemented [19].

While sodium provides one of the higher NMR signals in the body, the typical ^{23}Na-MRI image has a signal-to-noise ratio (SNR) that is thousands of times lower than that of a ^{1}H-MRI. From (2.2.18) the signal of an FID is directly proportional to ω_0, and as sodium has a γ that is $\sim$ 25% of that of

hydrogen, there is an initial drop in signal by a factor of 4 before even taking into consideration the concentration sodium is several thousand times lower than that of the proton as well.

The lack of signal combined with the challenge of even being able to acquire the signal from the fast decay that results in a deprivation of SNR. It is this lack of SNR that justifies the push for improvements to get higher quality ^{23}Na-MRI images in order to make ^{23}Na-MRI clinically relevant. This lack of SNR can be seen in Figure 2.7.

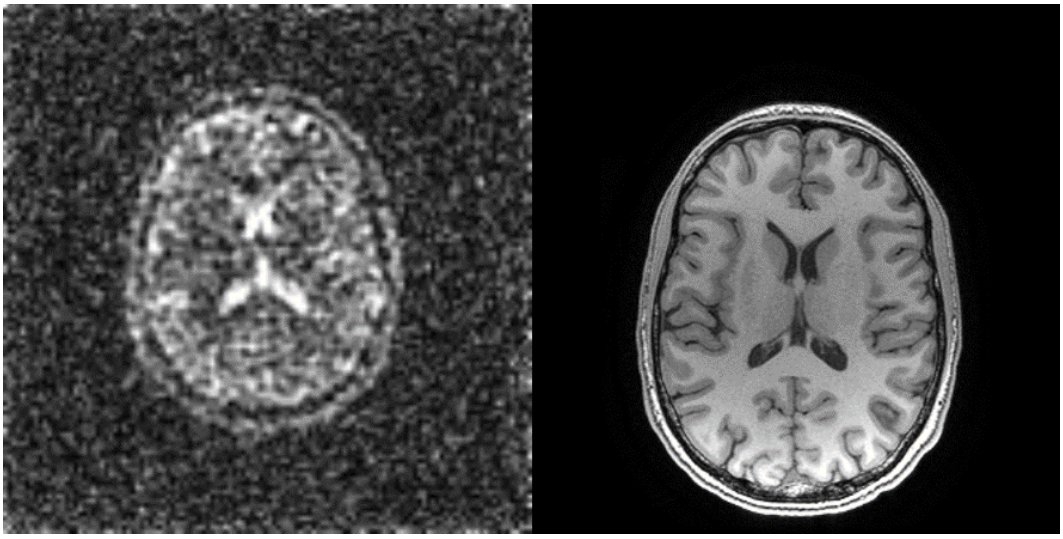

Figure 2.7: **Sodium Brain vs. Proton Brain** The difference in image quality between a brain image using a sodium imaging sequence (left) and a standard T1-weighted clinical proton sequence (right). These are of the same slice and of the same person's brain.

There are many ways to go about trying to improve the image quality of ^{23}Na-MRI, whether it be in new k-space trajectories, pulse sequence design, new reconstruction methods, or new approaches to image filtering, but an often overlooked component of MRI when looking to improve signal is the RF system. And that is why the focus of this project *is RF hardware*, or more specifically RF coils.

Chapter 3

Hypothesis and Objectives

Fractal geometry antennas have been implemented in telecommunication systems for years and were a hotbed of research in the late 90's and early 00's. Since then the vigor towards fractal antennas has decreased but still is a focus of many research groups and industries worldwide. Fractal geometries have been studied by mathematicians dating back to the early 1900's, and fractal antennas have been around since the 40's, although the term "fractal" was not used until Benoit Mandelbrot coined the term in 1983 [20, 21].

A fractal geometry is a pattern that is comprised of self-similar elements. A fractal can be decomposed into parts that are each a scaled-down copy (or at least similar to) of the overall structure. Antenna design has been predominately Euclidean in geometry, and as such, the radiation patterns have been Euclidean as well. Fractal geometries are an extension of Euclidean geometry, however things scale differently in the fractal dimension[2, 21–23]. For example, if you were to scale a square antenna's wire frame perimeter by 2, (from 1x1 to 2x2) then the surface area of that antenna scales by 4 (from 1 to 4). This is not consistent with fractal loops, where the first few generations define the surface area, and after that the perimeter can increase while hardly affecting the area!

Fractal antennas are usually exploited for their compact nature. In antenna theory, the strength of the produced field is proportional to the length of the antenna, and so fractal geometries have a greater effective size in a smaller space [12]. But this is not the only benefit of a fractal antenna. A single element fractal antenna can behave as though it is multiple elements as each subsection of the fractal can act as its own element. This results in a wider bandwidth than that of a standard single element diople, monopole, or loop. It has also been shown that designing phased-array antennas are a lot easier to do with fractal elements as they prove to be easy to tune and match as their mutual inductance is reduced compared to other antenna elements of similar sizes. In addition, the phased array fractal antenna has an even wider

bandwidth (BW) than a single element fractal. So called "shaped" antennas also produce higher gain and field strength [21, 22, 24].

Most research into fractal antennas focus on the far field applications as usually antennas are designed for long distance communication (multiple λ away) and as such the resultant conclusions do not look into the near field applications of such designs. However, MRI RF coils operate in the near field realm, where the field patterns being optimized exist within one or less wavelengths.

MRI RF coils, especially those designed for lower fields (i.e. <3T) and for the so called X-nuclei (i.e. non-proton nuclei), are classified in antenna theory as "electrically small" coils as the physical size of the coil tends to be $\sim \lambda/10$ or smaller. This poses a limitation, as generally speaking, electrically small antennas are poor radiators with narrow bandwidths [12, 21]. In the far field, the radiation pattern of an electrically small antenna of a loop with a specific radius will remain relatively constant regardless of geometry, however MRI RF coils operate in the near field, where the field patterns of the antenna will not be independent to geometry.

Due to the near field nature of MRI RF coils, the field patterns can be analyzed using Biot-Savart's Law which indicates that the field strength of a single loop element is inversely proportional to distance. Thus, the field generated by a MRI surface coil is inherently heterogeneous. However, since near field geometry plays a factor, there could potentially be a coil geometry that produces a more homogeneous field over a volume than that of a standard circle/loop design.

There exist hundreds upon hundreds of fractal geometries but the most explored in electromagnetic antenna theory are (i) Koch, (ii) Minkowski, (iii) Cantor, (iv) torn square, (v) Mandelbrot, (vi) Caley tree, (vii) monkey's swing, (viii) Sierpinski gasket, and (ix) Julia. This thesis will look at a Koch snowflake geometry as it is a fairly straightforward design to implement and has been shown to have positive results when it comes to MRI RF coil design [21, 22, 24, 25]. A Koch snowflake is created by combining three Koch curves to form a triangle as can be seen in Figure 3.1.

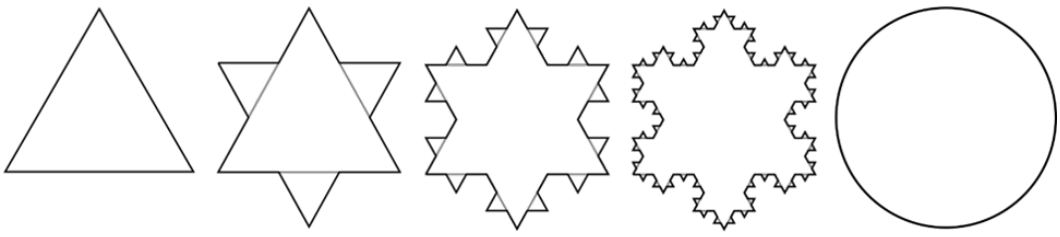

Figure 3.1: **Koch Snowflake Generations** The first four generations of a Koch snowflake geometry, compared to a circle of same radius

Thus, hypothetically, a fractal geometry surface coil can overcome the limitations of electrically small coils by offering a wider uniform transmit bandwidth, providing more image uniformity over a volume, as well as a stronger field compared to that of a standard circular surface coil.

It is hypothesized that an RF surface coil for ^{23}Na-MRI with a Koch snowflake fractal geometry will produce ^{23}Na images with a higher SNR and uniformity, compared to results from a standard circular RF geometry surface coil, by generating a more homogeneous B_1^+ field over both frequency and space.

To test the hypothesis, a "two stage" investigation was performed - first with simulation, and second with the construction and operation of the coils with the following objectives in mind:

Stage One: Simulation

1. Determine a suitable Koch snowflake generation geometry.
2. Simulate tuning and matching of both the Koch snowflake and standard circular coils, both of the same radius, as similarly as possible (ideally identically) by using the S and Z parameters.
3. Run the simulations, saving the magnetic field data for both coils to analyze and compare the simulated B_1^+ field produced by both.

Stage Two: Coil Construction and Testing

1. Design PCBs for both coils.
2. Tune and match both coils to 33.8MHz and 50Ω, respectively. Ideally both coils tune and match identically to permit the most accurate comparison.
3. Design and build a phantom to test the coils on.
4. Perform a routine ^{23}Na imaging scan to get SNR measurements.
5. Run a B_1^+ mapping sequence to experimentally determine field homogeneity.
6. Run a standard ^{23}Na imaging scan with various receive bandwidths to determine field homogeneity over a wider BW.
7. Test and compare the functionality of the coils *in vivo*.

Chapter 4

Materials and Methods

4.1 Coil Design and Simulation

The first step in the process was to design and test the coil geometries in simulation. But before simulation could begin, the design parameters of the coils needed to be determined. Furthermore, the most effective generation of the Koch snowflake, and an understanding as to whether it could be physically built, needed to be planned before determining the effectiveness of the parameters through simulation. Listed below are all of the design and simulation parameters that were used along with the rationale behind the decisions.

Coil Design Parameters:

- Coil diameter: A diameter of 90mm (∼3.5") was chosen, because (i) standard clinical surface coils have a range of diameters from 3-6", and (ii) a standard PCB is 10x10cm in size and the coil must fit on it.
- Copper strip width: Initially the width of the copper strip that forms the loop of the coil was chosen to be 5mm, which is standard, however in order to create a higher generation fractal geometry that width needed to be reduced to 3mm (wide enough to mount capacitors on but narrow enough to allow for a third generation Koch curve).
- Copper strip thickness: While technically the copper strip has a thickness, it is of an order of magnitude smaller than the other coil dimensions and so to save computational power and time, in simulation the thickness was assumed as infinitesimally thin.
- Koch snowflake generation: With the diameter and copper strip width determined, the "largest" generation of Koch snowflake that could be implemented was a third generation.

- Substrate material: Rogers RO4350 was the initial substrate chosen. But after looking into affordable PCB substrates, FR4 was the final selection (the change in substrate did not affect simulation results).
- Substrate thickness: The substrate thickness in simulation was chosen to be 5mm.
- Capacitive breaks: The number of capacitive breaks on a surface coil is an optimization problem between the reduction of the electric field and the loss of signal from the lossy components (safety versus signal), but the rule of thumb is one break per inch of the coil diameter (plus a matching capacitor in parallel) and so 5 capacitors were used in the design of each coil (4 tuning and 1 matching).

Simulation Parameters:

- Solution: A driven modal solution was chosen for network and field analysis
- Setup: A single solution frequency of 33.8MHz was chosen with 20 passes and a maximum ΔS of 0.02 was selected. A fast frequency sweep from 26MHz to 38MHz was implemented with a step size of 0.3MHz.
- Boundaries: A finite conductivity boundary was applied to the geometry of the copper strip, with copper being the chosen material to model conductivity off of. Five lumped RLC boundaries with only capacitive values were applied to the breaks in the copper.
- Excitations: A single lumped port with a characteristic impedance of 50Ω was used, and placed in parallel to the matching capacitor.
- Coil loading: To emulate a traditional sodium phantom, the coils were loaded with 0.9% w/v saline (and this is where the fields were analyzed). An air box was also placed above the phantom.

The two coils with the chosen design elements were simulated using ANSYS HFSS [26]. HFSS is a high frequency electromagnetic solver that implements a finite elements method (FEM) to solve for SYZ parameters, as well as the visualization of electromagnetic fields among other applications. An FEM solver uses Maxwell's equations to solve for the electromagnetic consequences of a structure by decomposing the problem into smaller finite triangular components called a mesh [27]. Shown in Figure 4.1 are the geometries that were modelled in HFSS.

Once the coil geometries are modelled into the simulation software, the capacitor values need to be determined to tune and match the coil to 33.8MHz

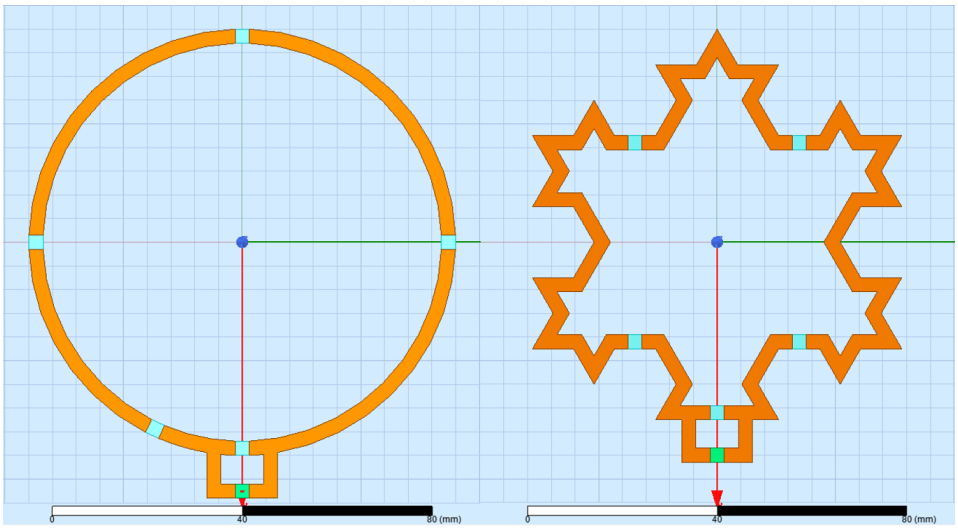

Figure 4.1: **Coil Geometries** The geometries of the two coils being compared, inputted into HFSS. The orange loops are copper, the blue squares are capacitors, and the green square is the lumped port.

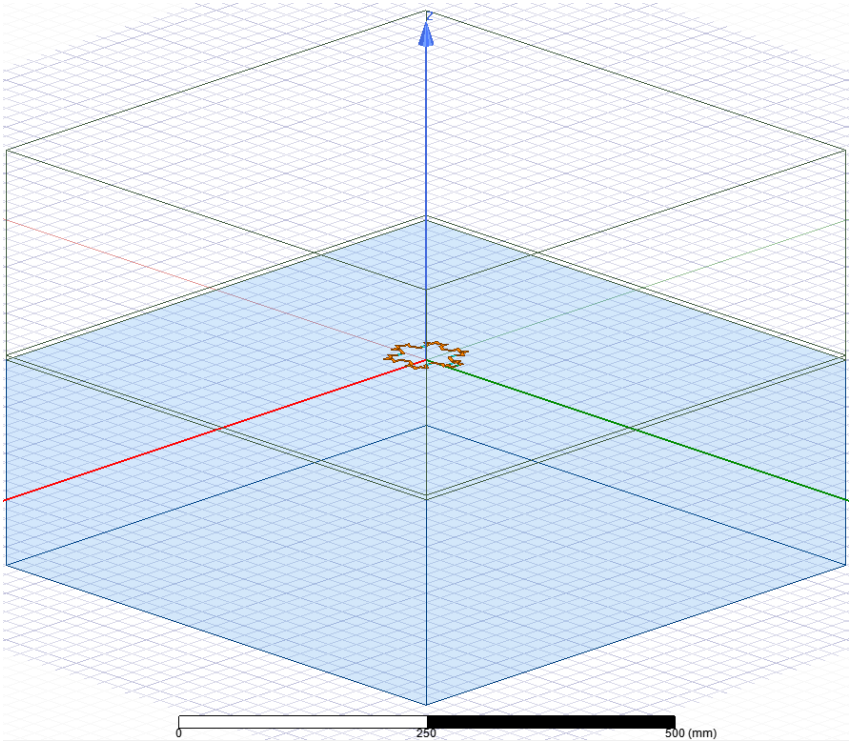

Figure 4.2: **Simulation Model** The entire simulation model can be seen here, with the coil mounted on the substrate with a sodium load below and an air box above.

and 50Ω. This can be done through either the built-in HFSS optimizers or manually. From Section 2.3.2, either s or z parameters can be used to make sure the right capacitor values are chosen. Figure 4.3 shows the z_{11} and s_{11} parameters of the circular and fractal coil. Table 4.1 shows resultant capacitor values and z-parameters at the desired tuning of 33.8MHz.

Coil Geometry	C_m (pF)	C_n (pF)	real(z_{11}) (Ω)	imag(z_{11}) (Ω)
Circle	317	595	49.8899	-0.2611
Fractal	443	699	49.8634	-0.0162

Table 4.1: **Tune and Match of the Simulated Coils** Capacitive values along with the impedance values at resonance.

With the desired tune and match achieved, data from the resultant simulated magnetic fields from each coil could be analyzed. Using the saline load as the medium in which the fields were produced, the magnetic field data was extracted from HFSS using the built in Fields Calculator at a resolution of 1x1x1mm. The total volume extracted spanned a 10x10x12cm region, to encompass the entirety of the field.

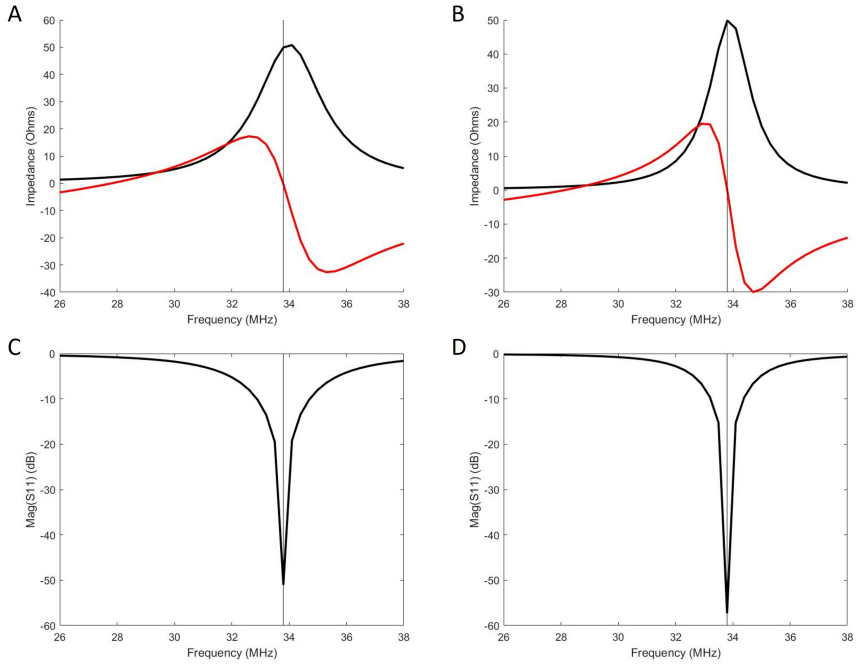

Figure 4.3: **Simulation Z_{11} and S_{11} Parameters** The z_{11} parameters (A,B) and the s_{11} parameters (C,D) of the circular (A,C) and fractal (B,D) coils. The z_{11} parameter plots show the real (black) and imaginary (red) components of the parameter (s_{11} is just the magnitude).

4.2 Coil Construction

The next stage in the process was to build the physical manifestation of the coils that were simulated. The coil geometries were exported from HFSS as a .dxf file and inputted into a printed circuit board (PCB) design software, called KiCad [28]. Now the simplest, and most traditional surface coil is a loop made by copper tape or cut from a copper sheet and adhered to a substrate, but with the intricacies of the fractal design, and a desire to keep the similarities between the two coils as high as possible (i.e. copper thickness and width) it was decided that the coils were to be manufactured on PCBs. For the purposes of this project, the PCBs were a single layer 10x10cm, 2mm thick FR4 substrate with the respective coil geometries etched into the top with 3mm wide copper. The resultant PCBs are shown below in Figure 4.4 and were manufactured by Elecrow (https://www.elecrow.com/).

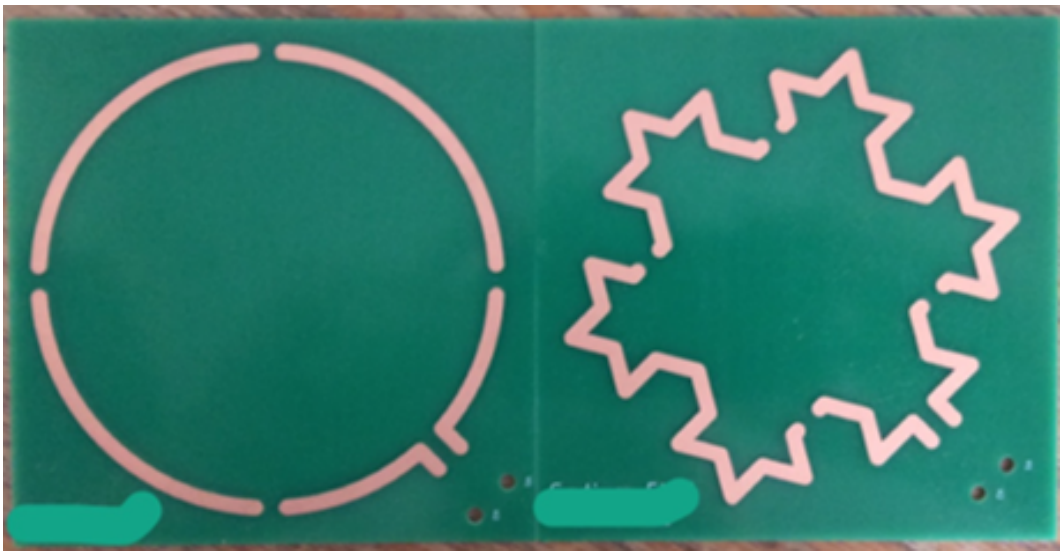

Figure 4.4: **PCBs of the Coils** Circular coil on the left and the Koch snowflake fractal coil on the right.

The next step was to tune and match the copper loops into functioning resonant RF coils. As discussed in Section 2.3, the simplest RF coil consists of a copper loop, some capacitors, and a coaxial cable. The copper loop serves two purposes, the first is to be the conductor that carries the current around the coil so that it isn't just an open circuit, and the second is to act as the inductor. Inductors are typically very lossy circuit components and it is best if they can be avoided. Inductors are just looped conductors and so a single loop coil is effectively a low energy inductor. The resistance in the coil results because copper is not a perfect conductor and there are losses as the signal propagates through the coil. The C_p is called the "matching" capacitor as it

does not affect ω_1 and can be used to alter the impedance of the circuit. The C_s is called the "tuning" capacitor as it is the only variable in the circuit that can be changed to change the resonant frequency.

Like in simulation, determination of the capacitor values was an experimentally iterative process, but unlike simulation there are optimizers to reduce time and effort and must be done manually. The iterative process had 7 steps and involved use of an Agilent 4395A VNA (Figure 4.5). For the purposes of tuning and matching the VNA was set to impedance mode and displayed the magnitude and phase of the z_{11} parameters):

1. Short all capacitive breaks in the coil except for one, where a known capacitor value is soldered. This was to determine the intrinsic inductance of the coil. Connect the coil to the VNA via a coaxial cable. By expanding the frequency range determine the first zero-crossing in phase. By using Equation 2.3.1, with the frequency of the zero-crossing and the known capacitance, the inductance of the loop can be calculated. The calculated inductance for the two coils were determined to be $L_{circle} = 190$nH and $L_{fractal} = 227$nH respectively.

2. Again by using Equation 2.3.1, this time by setting frequency to the Larmor frequency of ^{23}Na at 3T (33.8MHz), and the inductance to L, solved above, the capacitance required to tune the coil was determined. By multiplying the determined C_s by the number of breaks, the capacitor value at each break was calculated (C_n). The calculated C_n values were $C_{n_circle} = 468$pF and $C_{n_fractal} = 392$pF respectively.

3. The C_n value capacitors were soldered onto the breaks of the coils and, with the VNA, examined for phase zero-crossing and peak impedance magnitude. Ideally the phase is 0° with magnitude of 50Ω at 33.8MHz. However, in practice this is almost never the case.

4. The tuning capacitors are adjusted to shift the resonant frequency. Increase C_n to decrease the resonance and vice versa to increase the resonance. Adjust the matching capacitor to change the impedance seen at resonance. And while theoretically these will not affect each other, they do in practice.

5. Repeat steps 2 and 3 until the coils are tuned to 33.8MHz and matched to 50Ω.

6. Once tuned, it is important to note that loading the coil will shift the resonant frequency and lower the impedance and so steps 2-4 needed to be repeated but this time with the coil loaded with a phantom (ideally the one that would be imaged).

7. Once completely tuned and matched to 33.8MHz and 50Ω, the final step of attaching the coaxial cable is required. In theory the coaxial cable should be $\lambda/2$ in length, however at this resonant frequency that would mean a cable of around 4.57 meters which is too long for the MRI scanner. Any cable of a length not at $\lambda/2$ will cause a shift in the resonant frequency, so the shortest possible length of cable was chosen in hopes to reduce that shift. An 45.7cm cable was soldered onto both the circle and fractal coil. This length was chosen as it was the shortest the cable could be while still allowing for the coil to be able to reach the phantom from connection to the MRI.

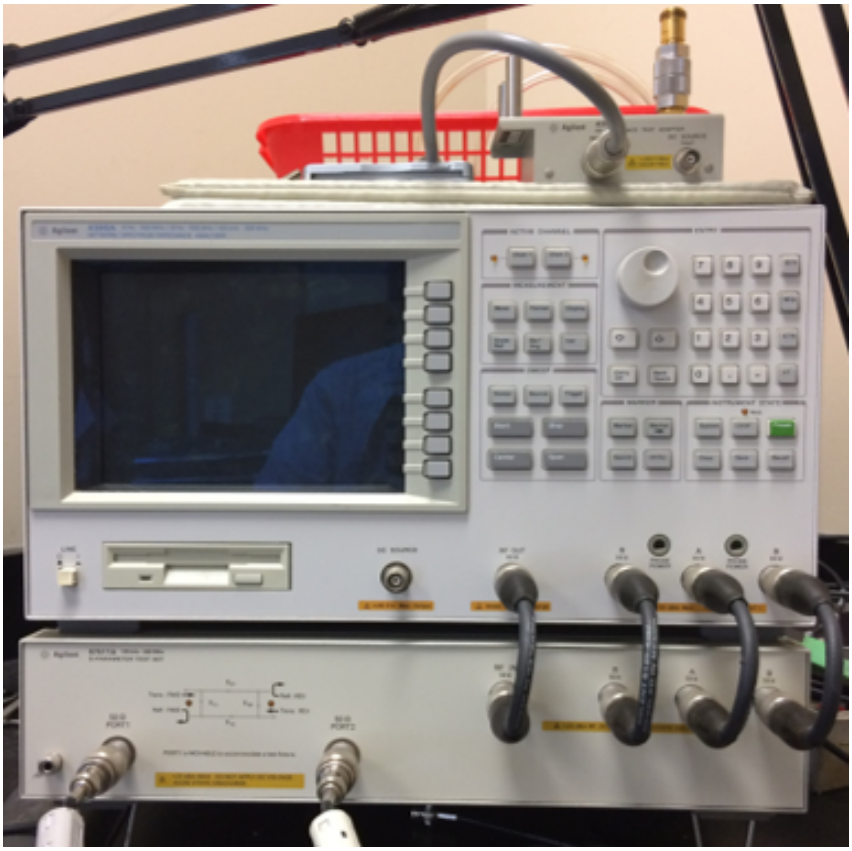

Figure 4.5: **Lab VNA Setup** Shown is the Agilent 4395A VNA. The top box is the network analyzer, the bottom box is the s-parameters kit (not used) and the box above the system is the disconnected impedance test kit.

The resultant z_{11}-parameters and s_{11}-parameters of the two coils after tuning and matching to a saline load are shown in Figure 4.6 and 4.7. The tune and match of both loaded coils were deemed acceptable enough to proceed with the experiments.

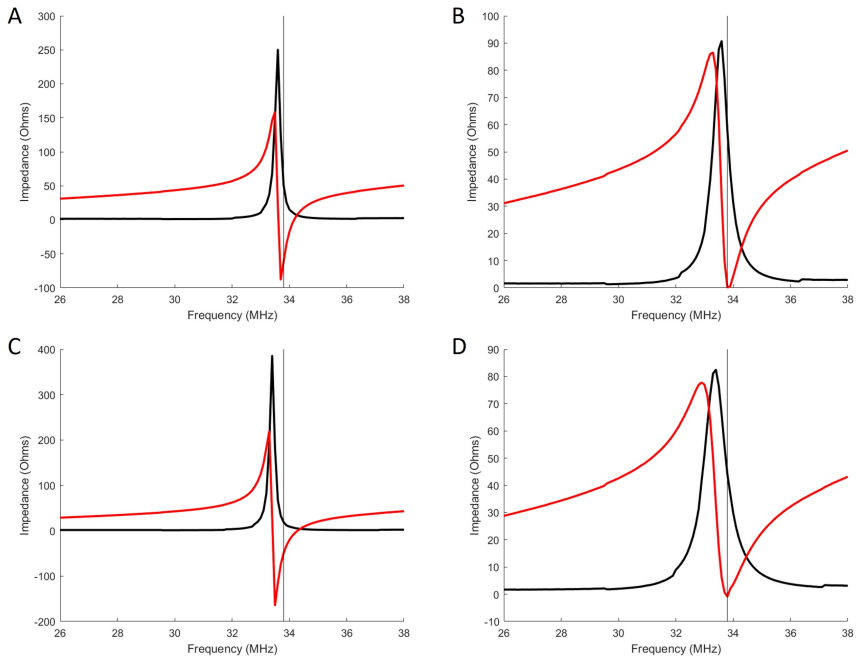

Figure 4.6: **Z_{11}-Parameters** Shown are the z_{11}-parameters of both the fractal (A,B) and the circle (C,D) in unloaded (A,C) and loaded (B,D) forms. The real (black) and imaginary (red) are shown.

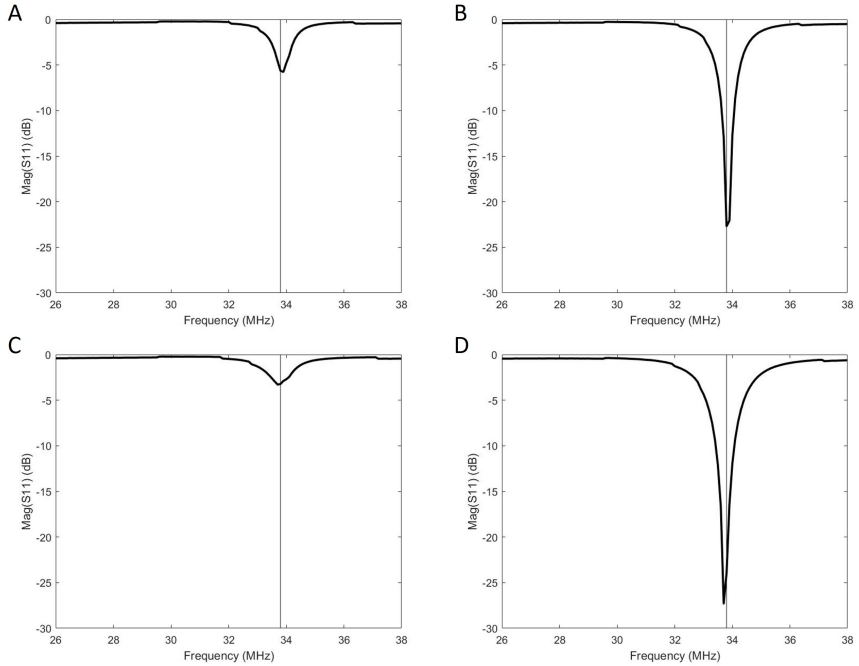

Figure 4.7: **S_{11}-Parameters** Shown are the s_{11}-parameters of both the fractal (A,B) and the circle (C,D) in unloaded (A,C) and loaded (B,D) forms.

4.3 Experimental Setup

A General Electric (GE) MR750 3T magnet was used for the testing of the two surface coils. The software version at the time of the tests was DV25. The scanner is located in the Imaging Research Centre (IRC) of St. Joseph's Healthcare in the Fontbonne building of the Charlton campus in Hamilton, Ontario. Since non-proton imaging is not generally what the MRI does, an additional piece of hardware is required so that the MRI can use the sodium coils. A sodium transmit/receive (T/R) switch was required to allow for RF power to be sent to and from the coils.

Another experimental setup point of note is what was being imaged. Called a phantom, the chosen imaging subject for the experiments was a watertight box filled with 0.9% w/v saline (NaCl). The phantom was constructed in order to provide a homogeneous sample in which the two coils could be accurately compared. The saline was created by mixing 4L of distilled water with 36g of NaCl. The plastic box with a flat top was sealed using marine sealant.

The phantom was placed on the MRI bed on top of a 4" thick piece of foam to elevate the phantom closer to magnet isocentre. A cotton cloth was placed on top of the phantom to give a slight bit of separation between the phantom and the coil to help with loading. The coil was then placed on the center of the phantom, connected to the T/R switch and then covered with a folded up sheet, the weight of which kept the coil from moving. Once in place, the coil/phantom were placed in to the centre of the MRI (i.e. isocentre) where the main magnetic field is most homogeneous.

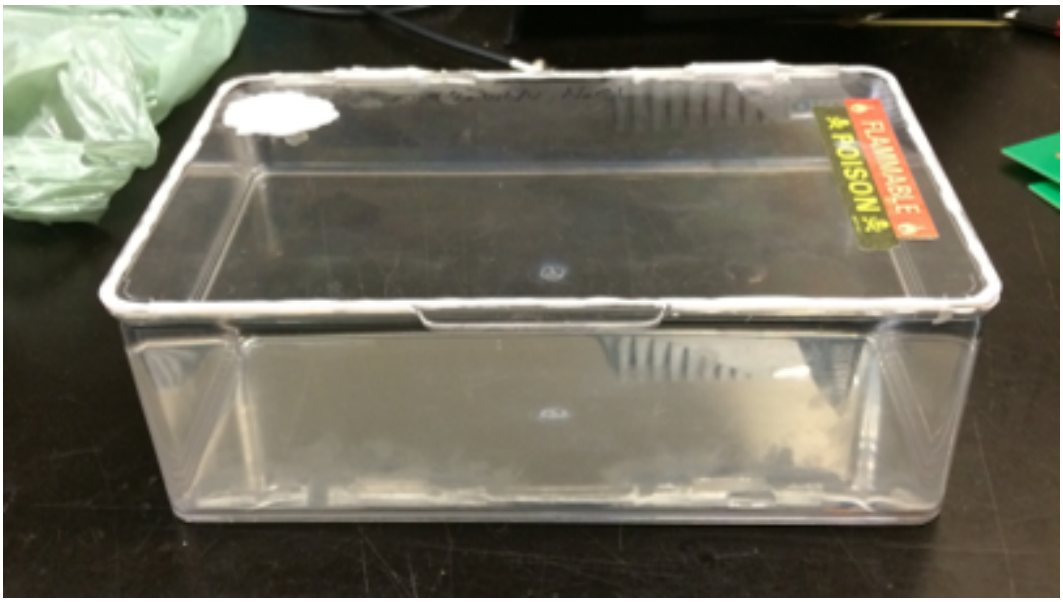

Figure 4.8: **Homogeneity Phantom**

Figure 4.9: **MRI Experimental Setup** The GE MR730 3T scanner with the circular surface coil connected to the MRI via the sodium T/R switch. The coil can be seen on top of the homogeneity phantom which is covered by a cloth. The phantom itself sits atop a foam riser which centers the coil in the isocentre of the magnet.

4.4 Pulse Sequences and Reconstruction

4.4.1 Multinuclear Spectroscopy (MNS) Prescan

Before any MRI scan begins, four of steps need to be performed in order for the scan to be successful:

1. Find ω_0,
2. Shim the magnet,
3. Set the centre frequency, and
4. Find the power required for a 90° RF pulse.

For a proton (i.e. routine clinical) scan, this happens automatically and in a matter of seconds using an optimization algorithm. But for non-proton MNS scans it is not so simple and needs to be done manually. The rationale for this is the fact that routine clinical scans are dominated by a water peak

which is easily optimized for. Often MNS scans show numerous metabolite peaks, all with similar magnitudes, resulting in difficulty for any routine solver. Although this is not true for sodium (only one peak) the scanner software still does not have the optimization routine in place (it's not pronto) and thus needs manual frequency and RF power selection. The magnet shimming can be done using a 3-plane localizer scan with hydrogen prior to MNS (i.e. magnetic field homogeneity is independent of nucleus to be probed), and the coils are already pre-tuned (see Section 4.2).

A GE Healthcare sequence called the "MNS Prescan", which is part of the MNS Research Pack (fidall PSD) developed by Dr. Rolf F. Schulte (GE Healthcare, Munich Germany) can be run in order to add some automation to the process. The full description of the scan can be found in [29]. This scan, iterated manually, allows one to determine initial values of ω_0 and RF coil transmit gain (TG) that would maximize the signal of a 90° RF pulse. This pulse sequence is manually run, each time changing values, until the output converges onto a gain and frequency. It is these final output values that need to be entered into the system before any other sodium scan can run.

Another GE-specific value that needs to be noted is a control variable (cv) called "xmtaddSCAN". This cv controls additional attenuation to the RF power before it is sent to the coil. The cv ranges from 0-200, each value representing 1/10 of a dB of attenuation. The default value depending on the sequence is between 0 and 20. However, because this project uses surface coils which are small with a limited FOV, the amount of power required is much smaller than that of a larger volume coil. A value of xmtaddSCAN=100 was determined to be effective in reducing the transmit RF power to an acceptable range in order to maintain safety as well as optimal image quality. Some additional sequence parameters are shown in Table 4.2.

TR (ms)	NEX	Flip Angle (°)	Pulse Type	FOV (cm)	Acq. Points
423.6	1	90	Soft	10	2048

Table 4.2: **MNS Prescan Parameters** Some of the pulse sequence parameters for the MNS Prescan.

4.4.2 B_1^+ Bloch-Siegert Mapping Sequence

B_1^+ mapping is a way to determine the strength of the transmit RF field produced by an RF coil in an MRI experiment. There are a few different pulse sequences and their respective calculation methods that could be used to obtain the B_1^+ map, and the method used in this project is a technique described by Sacolick *et al.* in their 2010 paper [30]. The method exploits an

effect called a Bloch-Siegert shift and results in the magnitude of the B_1^+ field strength encoded in the phase information of the resultant image.

A Bloch-Siegert shift is used to describe the phenomenon that if an off-resonance RF pulse, in the kilohertz range, is applied to the spins after normal excitation, the precessional frequency of the spins change [31]. This change in frequency, or shift, is proportional to the magnitude of the B_1^+ field squared.

The effective B_1^{eff} in the rotating frame is a constant and can be given by:

$$\gamma B_1^{eff} = \sqrt{\omega_{RF}^2 + \gamma B_1^2} \tag{4.4.1}$$

where γB_1 is the RF field and ω_{RF} is the frequency offset from Larmor frequency of the off-resonance RF pulse. By using simple trigonometrics on equation 4.4.1 the Bloch-Siegert shift (ω_{BS}) can be identified:

$$\omega_{BS} = \frac{(\gamma B_1)^2}{2\omega_{RF}} \tag{4.4.2}$$

and from that, the expected phase shift can be calculated:

$$\phi_{BS} = \int_0^T \omega_{BS}(t)dt = \int_0^T \frac{(\gamma B_1)^2}{2\omega_{RF}}dt \tag{4.4.3}$$

$$\phi_{BS} = B_{1,peak}^2 \int_0^T \frac{(\gamma B_{1,normalized})^2}{2\omega_{RF}}dt = B_{1,peak}^2 \times K_{BS} \tag{4.4.4}$$

where K_{BS} is a constant for a given RF pulse, and describes the phase shift of the pulse in radians/Gauss^2.

Generally when using phase to calculate any sort of parameter in MRI, a difference between two phase images should be taken, in order to remove any undesired or unintentional phase effects from the transmit, receive, and off-resonance B_0. By getting phase images with a $+\omega_{RF}$ and a $-\omega_{RF}$ off-resonance pulse, the B_1^+ field can be found as the subtraction of the two phase images produces a ϕ_{BS} image.

The pulse sequence used to produce the B_1^+ maps included a slice-selective soft RF pulse with a slice thickness of 1.0cm, followed by the off-resonance BS RF pulse with an ω_{BS} of 4kHz. Imaging gradients were implemented in a four arm spiral trajectory, as noted in Figure 4.10. The trajectory was designed using MATLAB code developed by Dr. Rolf F. Shulte (GE Healthcafe, Munich, Germany) and Dr. Brian Hargreaves (Stanford University). By inputting selected parameters into the .m function, a .wav file was produced along with a .mat file that was necessary for reconstruction. Some additional pulse sequence parameters are shown in Table 4.3.

There were 4 B_1^+ maps produced for each coil, the first was a sagittal slice through the centre of the coil shown in Figures 5.6 & 5.7 and the other 3 were

consecutive coronal slices centered at 1.5cm, 2.5cm, and 3.5cm away from the coil plane shown in Figures 5.8 & 5.9.

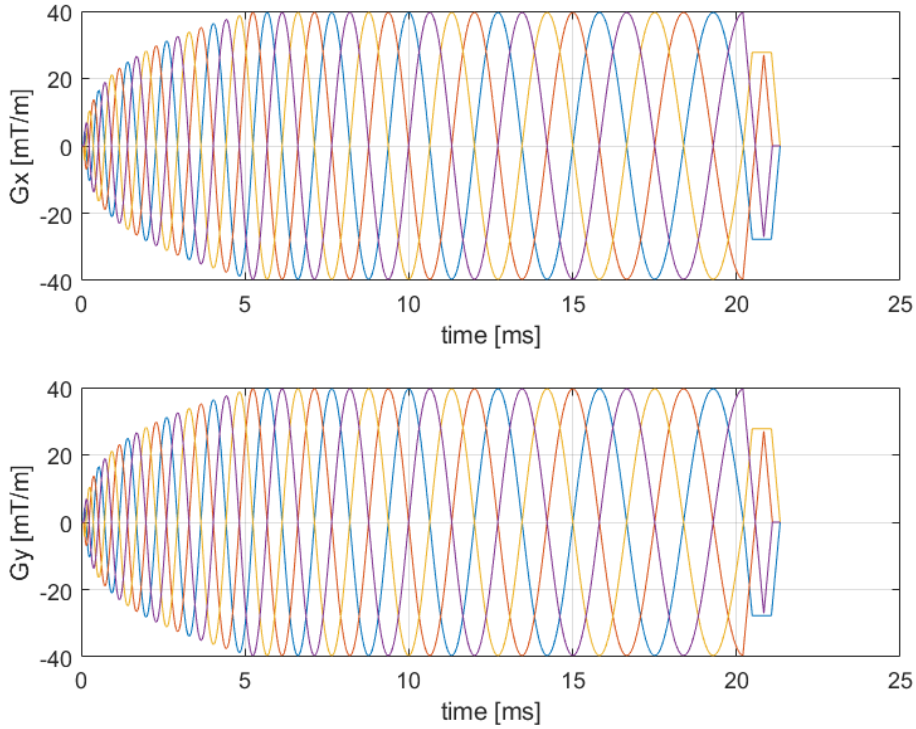

Figure 4.10: **B_1^+ Mapping Trajectory** Each unique coloured curve is the trajectory of one of the four arms in this sequence. The trapezoidal parts towards the end of the curve are re-winder gradients designed to remove any remaining magnetization before the next TR.

TR (ms)	NEX	Flip Angle (°)	Pulse Type	FOV (cm)	Acq. Points
86.0	150	90	Soft	15	5344

Table 4.3: **B_1^+ Mapping Parameters** Some of the pulse sequence parameters for the B_1^+ Mapping Sequence.

4.4.3 3D Radial Imaging Sequence

As Section 2.5 explained, the pulse sequences used to image sodium must be very fast in order to pick up the rapidly decaying sodium signal. UTE sequences with non-Cartesian k-space trajectories were used. The selected 3D radial sequence consists of:

1. A hard RF excitation pulse with a sufficiently large transmit bandwidth to excite the entire FOV. The hard pulse duration was 0.5ms with an amplitude determined by the TG determined in the MNS prescan.

2. In order to be an UTE sequence, this sequence forgoes a TE time and does not refocus the spins. Instead, directly after excitation the imaging gradients start, along with data acquisition. This is one example where FIDs are used in the imaging sequence.

3. The imaging gradients' trajectory is a radial spoke that starts at the centre of k-space and moves outwards towards the edge of k-space. The spoke extends for 15ms, with 64 samples along it.

4. There is one spoke per TR, and with each TR, the spoke extends along a different angle. This specific sequence has 7333 unique spokes, and therefore 7333 TRs. The sequence works by rotating a singular spoke by a phi and theta. The angles of rotation for each of the spokes is given in Figure 4.11.

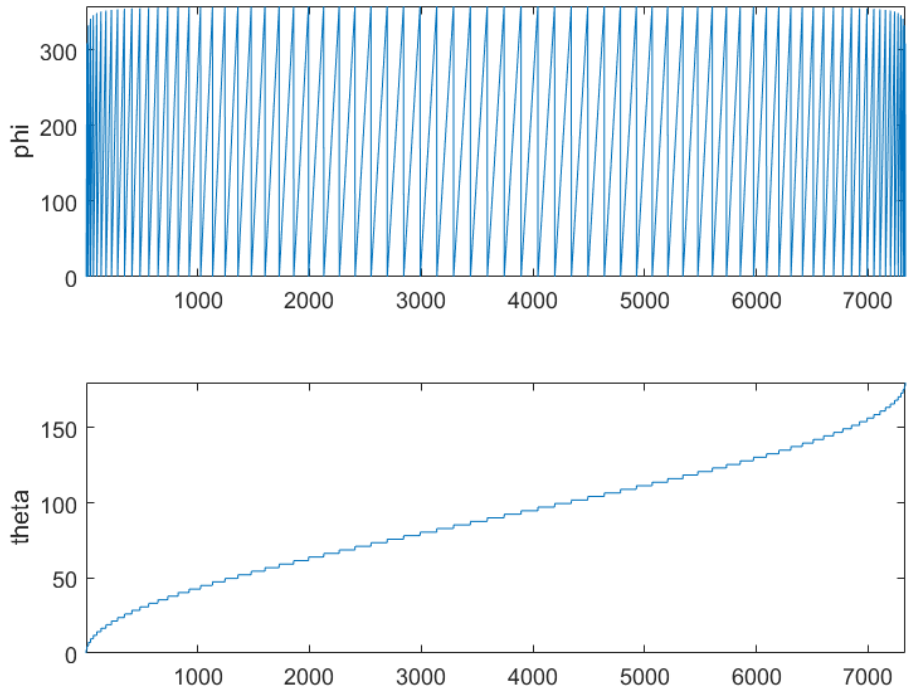

Figure 4.11: **3D Radial Phis and Thetas** The rotation angles of all 7333 spokes in the 3D radial sequence (in degrees).

TR (ms)	NEX	Flip Angle (°)	Pulse Type	FOV (cm)	Acq. Points
23.0	2	90	Hard	Variable	64

Table 4.4: **3D Radial Sequence Parameters** Some of the pulse sequence parameters for the 3D radial sequence.

The 3D radial imaging sequence was used in multiple experiments for this project, including:

- Signal-to-noise ratio measurements,
- Field strength and homogeneity measurements,
- Knee imaging, and
- Bandwidth homogeneity measurements.

and there were no changes to the sequence between experiments except for FOV. The various FOVs for each experiment are given in Table 4.5.

Experiment	SNR	Field Strength	Knee	BW
FOV (cm)	15.0	15.0	24.0	4.0-24.0

Table 4.5: **3D Radial Sequence FOVs** The field-of-views for the 3D radial sequence experiments.

4.4.4 2D and 3D K-Space Reconstruction

As introduced in Section 2.4.2, the raw data obtained from the MRI is in a spatial frequency domain called k-space. This k-space data needs to be transformed via an inverse FFT in order to get to image space. However, it is not as simple when dealing with non-Cartesian k-space.

Regridding is the most frequently used method when it comes to MRI image reconstruction of non-Cartesian data and the algorithm used for these experiments is described by Beatty *et al.* [32] and implemented for GE Healthcare by Dr. Rolf F. Shulte. Both the 2D spiral sequence and the 3D radial sequence follow the same reconstruction algorithm, with the obvious difference in that the mathematical functions and operations are expanded to three dimensions when dealing with the radial data, and reduced to two dimensions when dealing with the spiral data.

Regridding algorithms tend to require two stages, sample density compensation followed by an inverse FFT. The algorithm used forgoes the first stage (by assuming it to already be completed) and reduces the problem to a simple

NUFFT [19] in which the inverse Fourier transform is estimated through the following four steps [32]:

1. Convolve the assumed density compensated k-space data with a regridding kernel,
2. Sample the result onto a Cartesian grid,
3. Perform either the 2D or the 3D inverse Fourier transform
4. Perform a correction by multiplying by an apodization function.

The mathematical expression for the regridding algorithm if simplified to the 1D example (it is easy enough to implement it in 2&3D if the regridding kernel is separable) with the assumptions that the image is of unit size with pixels at $-N/2, -N/2+1, ..., N/2-1$ and that k-space is sampled at G spaced points in [-0.5 0.5] is:

$$\hat{m}_s[i] = \mathrm{IFT}\{[M_s(k_x) * C(k_x)]\mathbf{III}(Gk_x)\}(i)\frac{1}{c(i)} \tag{4.4.5}$$

where $\hat{m}_s[i]$ is the estimated image produced by the regridding alogorithm, $M_s(k_x)$ is the density compensated sampled k-space, $C(k_x)$ is the regridding kernel, and $1/c(i)$ is the apodization function, which is just the reciprocal of the inverse Fourier transform of the regridding kernel.

The regridding kernel used by the algorithm is a Kaiser-Bessel windowing function. Given are the expressions for both the kernel and its inverse Fourier transform:

$$C(k_x) = \frac{G}{W} I_0(\beta\sqrt{1-(2Gk_x/W)^2}) \quad \text{for} \quad |k_x| \leq \frac{W}{2G} \tag{4.4.6}$$

$$c(x) = \frac{\sin\sqrt{(\pi W x/G)^2 - \beta^2}}{\sqrt{(\pi W x/G)^2 - \beta^2}} \tag{4.4.7}$$

where $I_0(k_x)$ is a zero-order Bessel of the first kind and $\beta = \pi\sqrt{\frac{W^2}{\alpha^2}(\alpha - \frac{1}{2})^2 - 0.8}$ with α being the over sampling ratio G/N.

Both the 2D spiral and the 3D radial sequences were reconstructed using this algorithm but were reconstructed to different matrix sizes. The sizes of the reconstructed images are given in Table 4.6.

Experiment	B_1^+	SNR	Knee	BW
Matrix Size	80	48	48	48
Resolution (mm)	1.875	3.125	5	0.833-5

Table 4.6: **Reconstruction Parameters** The reconstruction matrix parameters, with the matrix size being either 2D or 3D depending on the sequence, and the corresponding resolution.

4.5 Experiments Performed/Data Analysis

There were six experiments performed using the aforementioned pulse sequences. The data sets were then analyzed using MATLAB (Mathworks, Natick MA) [33]. Each of these experiments and its purpose were:

- Simulation of magnetic field data for field strength and homogeneity measurements.
- Acquisition of four B_1^+ maps for field strength/homogeneity determination.
- 3D sodium MR imaging of the homogeneity phantom for SNR and field strength/homogeneity measurements.
- 3D MR imaging of the homogeneity phantom's edge, over 4 FOVs to assess transmit bandwidth homogeneity.
- 3D MR imaging of a geometrical phantom, over 4 FOVs, for assessment of geometric aberration that could arise due to variations in BW homogeneity.
- 3D MR imaging of a healthy human knee (both a 3D sodium and a 3D proton reference imaging scans) for the purpose of a direct coil comparison in a "clinical" setting.

4.5.1 Simulation Data

As stated in Section 4.1 the simulated magnetic field data were exported (from HFSS) as complex field values in A/m. The data was converted to field magnitude in μT. Magnitudes of resultant magnetic fields are shown in a sagittal view in Figure 5.1 and in three coronal slices in Figure 5.2. The circular and fractal coil magnetic fields were then analyzed and compared based on strength and homogeneity.

The first comparison involved how the field strength diminished as the distance from the coil plane increased. This was completed by calculating

the average magnetic field strength over a circular ROI for every coronal slice underneath the coil, from the bottom of the substrate up to one coil diameter away. Figure 4.12 illustrates the ROIs used in the calculation. The average field strength over each ROI was plotted versus distance away from the plane as shown in Figure 5.3. In addition, the maximum and minimum field values in each ROI were plotted to show field homogeneity with distance.

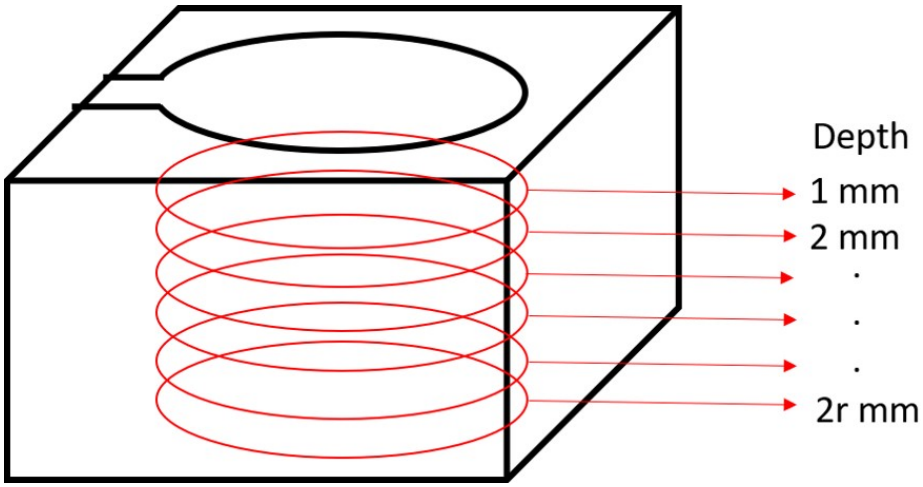

Figure 4.12: **ROIs as Distance Increases Axially** To visualize how the magnetic field strength of each coil decays as the distance away from the coil increases, the average field strength was calculated over a circular ROI centered on the coil, and as it moves away from the coil plane.

The field strength and homogeneity were also analyzed over volumes. As described in [11], the imaging "sweet spot" of an RF surface coil exists in the cylindrical region bounded by the radius of the coil, and between a distance of $r/2$ and r away from the coil. Figures 5.4 B & C show this sweet spot for the simulated fields. Thus, the average field strength, along with its standard deviation, were calculated over the volume of the sweet spot. A secondary ROI situated in the sweet spot, but with a radius of 25mm instead of 45mm was also used, as the fractal coil has two radii, an inner and outer. The results were plotted in Figure 5.4. Spherical ROIs were also used to calculate field strength and homogeneity. Six spheres of varying radii (6mm to 18mm) were placed in the centre of the sweet spot, with their lowest point fixed at the coil's radius away, and the average field strength and standard deviation were calculated (Figure 5.5).

4.5.2 B_1^+ Mapping

The B_1^+ maps were first generated from the phase images using the method outlined in Section 4.4.2, and then overlayed on top of the magnitude images

produced by the pulse sequence. Any data points containing a negative field value, or 0 were discarded. Only the data points that fell into the FOV of the coil were overlayed. The field maps can be seen in Figures 5.6, 5.7, 5.8, and 5.9. In addition, average field strength and standard deviation were determined and are included in each respective figure.

4.5.3 Homogeneity Phantom Data

With the FOV of surface coils being quite small, and the GE Healthcare stock B_1^+ mapping sequence requiring a 10mm thick slice, a high resolution B_1^+ map was out of the question. Thus the simulation analysis could not be compared one-to-one against experimentally determined B_1^+ mapping data. However, as MR signal strength is proportional to the sine of the flip angle, which in turn is proportional to RF field strength[1], the 3D imaging sequence can be used to perform strength and homogeneity calculations: the signal is directly related to field strength, and hence plots resembling the simulation analysis can be produced. Therefore, using the 3D imaging data of the sodium homogeneity phantom, the same analysis done on the simulation data was performed, including field strength and homogeneity over axial distance (Figure 5.10), and volume analysis for both cylindrical (Figure 5.11) and spherical (Figure 5.12) ROIs.

The 3D data was also used to perform SNR calculations. An SNR calculation requires two ROIs, one of the signal of interest, and the other of unstructured noise. The formula is given as:

$$SNR_{region} = \frac{\mu_{signalROI}}{\sigma_{noiseROI}} \tag{4.5.1}$$

Each ROI used in Figures 5.11 and 5.12 were also used as a signal ROI in an SNR calculation.This resulted in 5 different SNR values for each coil as there were 5 different signal ROIs used. The noise ROI was chosen to be spherical ROI above the phantom and coil and can be seen in the aforementioned figures as well. The calculated SNR values are given in Table 5.2.

4.5.4 The Effect of Varied BW on Imaging Quality

While not a directly valuable asset in ^{23}Na-MRI, another hypothesized benefit to a fractal geometry coil apart from an SNR increase, is increased homogeneity of the field over a wider bandwidth (BW), compared to a standard circular coil. Physiologically, sodium has just one narrow NMR resonance but there

[1]Note that because of reciprocity not only is signal $\propto B_1^+$, it is also $\propto B_1^-$, which is the field induced in the coil and so the homogeneity of the coil's field will effectively have double the affect on the signal, in both generation AND acquisition.

are other nuclei like ^{31}P and ^{13}C that have spectra that span over kilohertz. When performing proton-based imaging one mainly has only to consider the chemical shift difference between water and fat resonances, to have sufficient bandwidth per pixel (220Hz at 1.5T, 440Hz at 3T). For imaging non-proton nuclei the need for sufficient bandwidth across multiple voxels across an image is magnified. That means each voxel must have enough (homogeneous) BW in order to both maximize signal acquisition and also to ensure uniformity across the field of view.

Since sodium has only one NMR peak, the BW homogeneity must be calculated over an entire 3D volume as opposed to voxel-by-voxel. The ideal way to do this is to run a 3D acquisition multiple times, changing the receive bandwidth (RBW) each time, restricting the amount of BW across the FOV. As the receive BW decreases, there should be an increase in SNR (i.e. SNR is proportional to $1/\sqrt{RBW}$) albeit with a concurrent decrease in image quality [8]. A coil with a more homogeneous BW should have higher image quality as the BW decreases, compared to a coil that does not. Note that it is the receive BW that is altered as transmit BW tends to be fixed based on the RF pulse selected for the sequence.

While this would be the ideal way to test for BW homogeneity, the 3D radial sequence used in this project had limitations. A major limitation being that the RBW is set to 1.95kHz and cannot be changed. The only parameter in the sequence that the operator has control over is the FOV, which can be used in a "makeshift way" to test the BW homogeneity. Both the receive BW and the number of acquisition points per spoke of the 3D radial sequence are constant, which means each sample in k-space has the same BW regardless of FOV size. This means as the FOV in image space decreases, the FOV in k-space increases, and each sample has to represent more frequencies, which will stretch out the BW which should result in a poorer image.

It was decided that to test field homogeneity of both coils the edge of the homogeneity phantom would be imaged at decreasing FOVs, and the coil that could more accurately represent the edge as a step function would have the more homogeneous field over BW. The 3D radial sequence was used, and a sagittal slice was chosen, centered at the edge of the phantom and the centre of the slice was chosen such that it did not vary between varied FOV acquisitions. After data acquisition and image reconstruction, each FOV was analyzed with these steps:

1. A central sagittal slice was chosen (the same slice for each FOV) and the middle four rows through the image that bisect the edge of the phantom were selected, as shown in Figure 4.13.

2. The four rows were averaged together to make one vector that spanned the length of the image in order to help in noise reduction.

3. The section of this averaged row that spanned the phantom's edge, 10mm in each direction was plotted against the ideal representation of the edge, a heavy-side function, and normalized for easier analysis and comparison.

4. The 2cm long row of voxel intensities was then compared to the 2cm long heavy-side function and an R^2 coefficient was determined for how well the observed data represented the heavy-side.

$$R^2 = 1 - \frac{\Sigma(y_i - \hat{y}_i)^2}{\Sigma(y_i - \bar{y})^2} \tag{4.5.2}$$

5. This R^2 value was the metric used to compare the BW homogeneity of each coil.

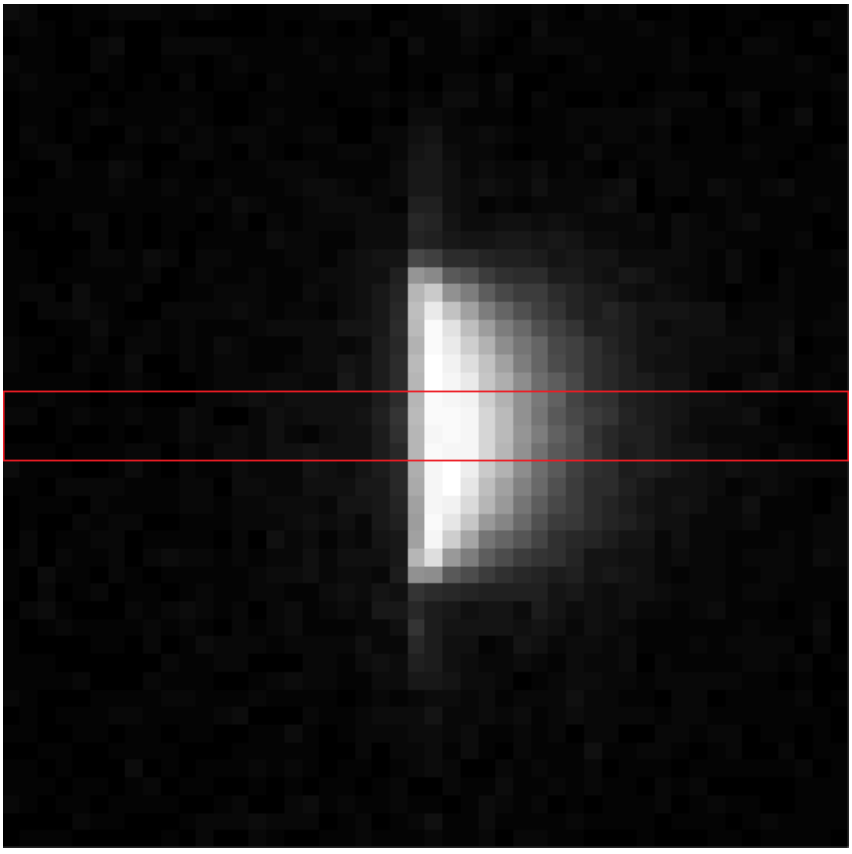

Figure 4.13: **Rows Selected for BW Homogeneity Measurements** The 4 rows between the two horizontal red lines were averaged together and used to measure the BW homogeniety of the two coils. All FOVs used the same four middle rows through the edge of the phantom.

Another by-product of a reduced RBW is an increase in geometric aberration in the resultant image, and so an experiment that measures the coil's ability to capture geometric truth as the FOV decreases should also be done. It is important to note that this effect will be much larger if imaging nuclei with broader spectra, ie. ^{31}P or ^{13}C, and so the result for this experiment may be negligible as ^{23}Na has quite a narrow spectrum but because it an issue in MNS generally, it is still worthwhile to explore. So a second experiment was performed to analyze the BW homogeneity of the coils, via quality of geometric truth. To perform this experiment a 3D-printed line-pair phantom was used (Thanks to Paul Polak who provided the phantom) (Figure 4.14). This phantom was designed to test resolution of ^{23}Na-MRI pulse sequences. It contains agar gel with 15mM NaCl, which was 1/10th the concentration of sodium used in the homogeneity phantom (which was 0.9%w/v, or 154mM).

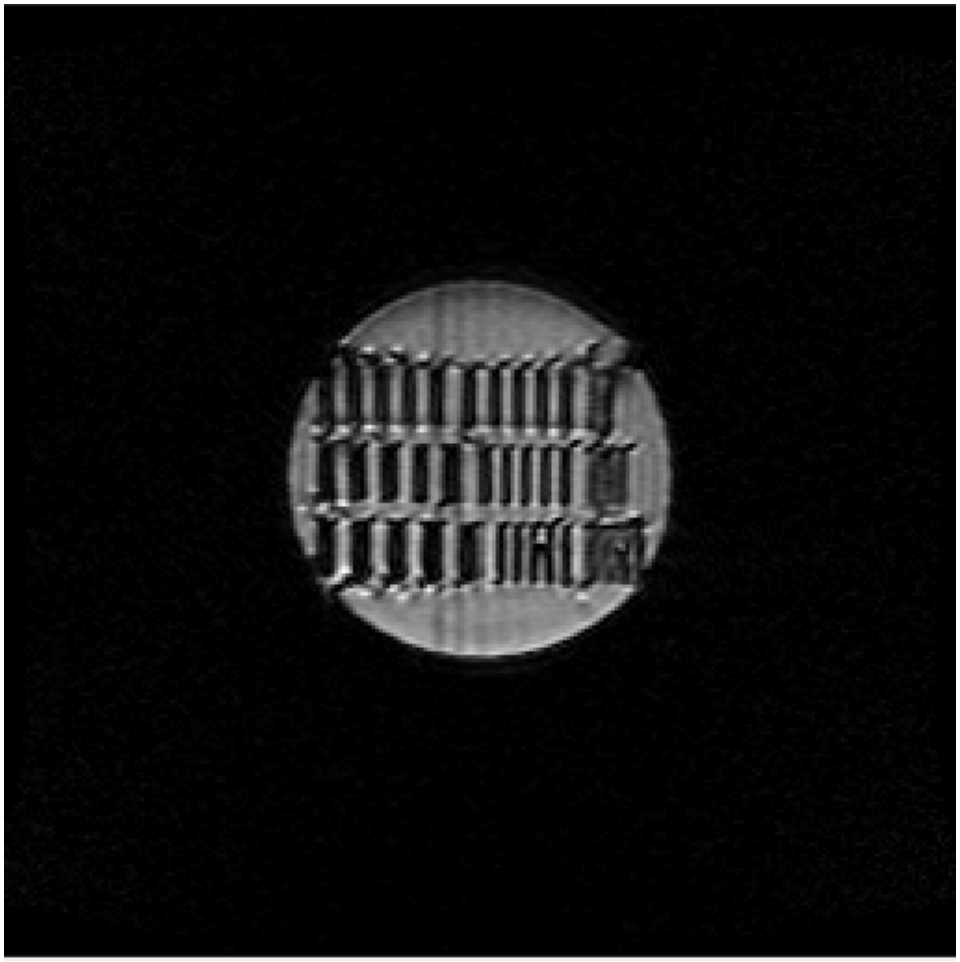

Figure 4.14: **Geometric Truth Phantom** A proton MRI image of the geometric truth phantom.

The phantom was imaged at four FOVs for both coils (8cm, 12cm, 16cm, and 24cm) as well as with a proton sequence to obtain "geometric truth"[2] and then once the images were reconstructed they were analyzed as such:

1. The centre 8cm FOV of a coronal slice was taken from each separate FOV, from both sodium and proton scans, in order for FOVs to be accurately compared. To ensure voxel volume consistency the entire 48x48 of the 8cm FOV was used, the centre 32x32 of the 12cm FOV was used, the centre 24x24 of the 16cm FOV was used, the centre 16x16 of the 24cm FOV was used, and finally the centre 42x42 of the proton image was used.

2. The slices were then resized to 48x48 voxels using the MATLAB function *imresize()* and normalized to provide easier comparison.

3. Each slice produced by an FOV was then subtracted from the proton image. In an ideal case of perfect geometric representation, the subtracted image would be a field of zeros. Any voxels with remaining signal would represent a voxel that did not accurately represent the structure.

4. The absolute value of the subtraction images were displayed for each coil (Figures 5.19 and 5.20) and any voxels in the subtraction image that were under 0.2 in value (0 being ideal representation, and 1 being perfect non-representation) were set to 0 as well in order to take into consideration random image noise.

5. As well as an intra-ocular comparison between the subtraction images, the percentage of voxels not zero, to the number of total voxels was calculated, to represent a sort of misrepresentation ratio, where the higher the percentage, the worse the representation of geometric truth there is.

An important caveat to both of these experiments is that while the reduction in FOV should cause a decrease in signal and therefore image quality, because the reconstructed image size for this sequence is a constant 48x48x48, the reduction in FOV will also reduce the voxel size. Signal is directly proportional to voxel size and so it is impossible to distinguish the decrease in image quality because of the "reduced" BW and because of the decreased voxel size. It is the hope that because both coils will experience the same (roughly) signal decrease because of voxel size, that a comparison can still be made due to the BW.

[2]Geometric truth is best done through the use of computer tomography (CT) scanning. However, to approximate this with MRI a phantom is placed at isocentre and minimum TE and TR are used to acquire images.

4.5.5 In Vivo Sodium Imaging

The goals of this were to (1) see if the two coils can actually image the low concentrations of sodium in the body, and (2) to do a direct comparison of performance of an *in vivo* scan. To make the comparison a healthy human knee was used to represent a potential clinical application in which the coils would be used in. For each coil, the experiment was run as such:

1. The sodium surface coil was placed on the lateral side of the right knee, with a 1cm foam pad separating the coil from the knee, and the coil was secured in place.

2. The body coil was used to obtain a proton density weighted image of 22 sagittal slices through the knee.

3. The 3D radial sequence was then used to image the sodium in the knee.

4. The reconstructed images were then analyzed.

The metrics used to compare the two sodium surface coils were the intra-ocular approach of a visual comparison, and then an SNR measurement was taken. The analysis was done with the following steps:

1. The proton images were obtained over a 16cm FOV while the sodium images were taken over a 24cm FOV and so the FOV of the sodium images were reduced by removing the excess rows, columns, and slices that did not contain "knee". This reduced the 48 slice 48x48 images to 14 slices of 32x32 images, each with a now 16cm FOV for a 1:1 size match with the proton images.

2. The sodium images were then registered to the proton images and then overlayed on top of them in order to show some reference as to what the sodium was representing.

3. The overlayed sodium images were then thresholded to the signal value of 10000, which is an arbitrary value that seemed to remove the noise from the image while retaining enough of the signal.

4. Composite images, shown in Figures 5.21 through 5.24, were used to visually compare the two coils.

5. To calculate SNR, the standard practice involves selecting a signal ROI and a noise ROI, however in these sodium knee images, there is no definite "signal" ROI other than a very elongated and weird shape and so a slightly different method was performed. The 14 slices that were determined to have "knee" in them were concatenated and a histogram of the

voxel count over voxel intensity ranges was created. The signal ROI was determined to be any voxel with a signal that was higher than 50% of the maximum signal, and the noise ROI was determined to be any voxel with a signal that was less than 25% of the maximum signal.

It is important to note that the SNR calculation is not a true representation of the SNR as it is possible for noise to have high signal, and for some signal to get lost in the noise but it does provide a decent enough metric to compare coils as both should experience a random distribution of noise intensity driven by the same stochastic process. The comparisons between coils should also be taken with "a grain of salt" as both coils are loaded differently by the knee as seen in Figure 4.15.

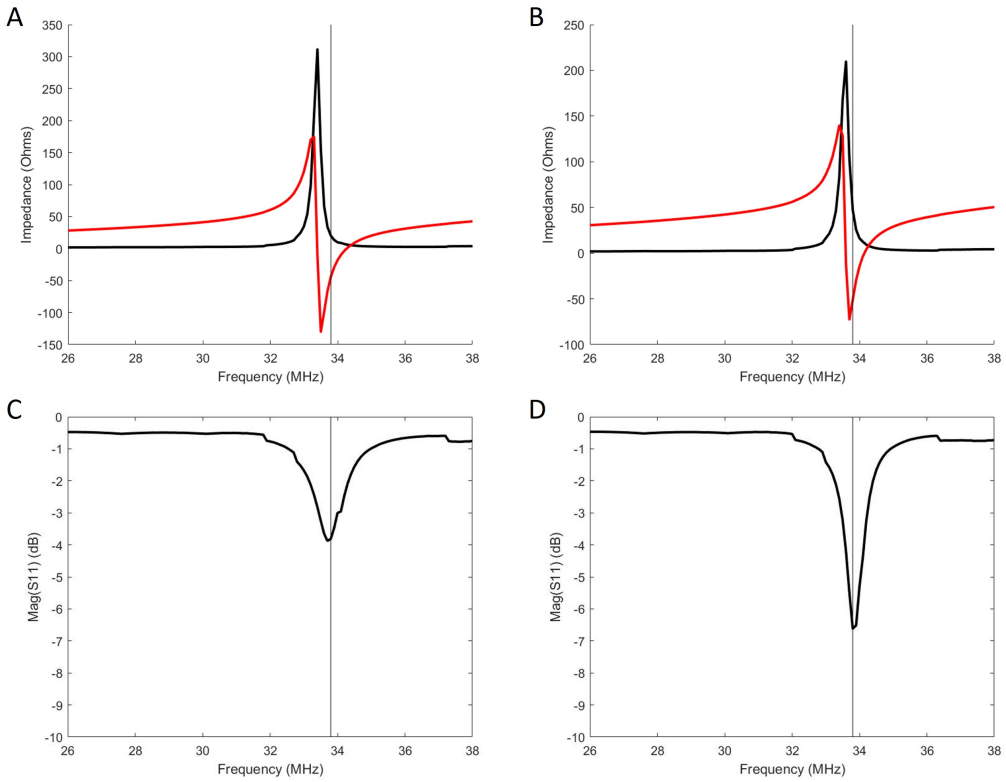

Figure 4.15: **Tune and Match of the Knee** The z_{11}-parameters (A,B) and the s_{11}-parameters (C,D) of the circular (A,C) and fractal (B,D) coils when loaded by the knee. The z_{11}-parameter plots are given in real (black) and imaginary (red) components while the s_{11}-parameter plots are given in just magnitude.

4.6 RF Coil Safety

4.6.1 Specific Absorption Rate (SAR)

It is important to comment on MRI RF coil safety before experiments are performed. The biggest concern with RF coils is the resultant electric (E) field produced by the coil. The E field can couple with the tissue and cause heating potentially leading to RF burns, if there is enough power deposited into the tissue. This is why on a surface coil there are multiple breaks with capacitors, in order to break up the E field and reduce the risk of burns. The highest risk for burns are when the coil is in direct contact with the tissue and so when imaging there is always an interface between the coil and the patient, usually both a plastic encasing of the coil, and foam pad between that casing and the skin.

The main parameter when it comes to MRI RF safety is the specific absorption rate (SAR) which measures the amount of RF energy in watts that is deposited in the tissue per unit mass, given in W/kg. The calculation of SAR is quite complex and involves many variables, but can be shown that:

$$\text{SAR} \propto \frac{r^2 \sigma \alpha^2 f_0^2 d}{\rho} \tag{4.6.1}$$

where r is the radius of the object, σ is tissue conductivity, α is the flip angle, f_0 is the transmit frequency, d is the duty cycle (average to peak RF power), and ρ is tissue density. A complete formula for the calculation of SAR is given as:

$$\text{SAR} = \frac{\sigma}{2\rho} \cdot |E|^2 \cdot (\frac{\tau}{TR}) N_P N_S \tag{4.6.2}$$

where $|E|^2$ is the magnitude of the electric field, τ is the RF pulse duration, TR is the repetition time, N_P is the number of pulses, and N_S is the number of slices.

A study in 1984 in rhesus monkeys found that the limit to RF exposure in terms of SAR was 4W/kg [34] and is equivalent to raising the entire body temperature by 1°C. Canadian Safety Code 6 [35] outlines the maximum exposure limitations of RF in both the internal electric field of excitable tissue, and in SAR. In a controlled environment, the maximum E field that a person can be exposed to at 33.8MHz is 53.8 V/m over a 6 minute period and the SAR over a 6 minute period is limited to 8W/kg if averaged over 1g of tissue. The method the MRI uses for calculating SAR is proprietary information, however the displayed SAR values are determined such that they are overly cautious estimates.

4.6.2 Coil Safety Experiment

There are a few things to consider when determining if the constructed coils can be deemed "safe to use". The coils constructed for this work would never be used in a clinical setting or research study as there are exposed conductors and electronics which would need to be covered and insulated before being used. However, for the imaging of the knee in this project, to limit the chances of injury, the coil was placed with the substrate facing the subject and between the substrate and the knee was a cotton scrub pant leg and a 1cm thick foam pad. Obviously the closer to the coil, the higher risk of burns. We wanted to determine if the RF being radiated from the coil would ever pose a threat of burns and so the following experiment was conducted.

A slab of pork belly was purchased to serve as the "patient". Four fibre optic temperature sensors from Neoptix (https://www.neoptix.com/t1-sensor.asp) with an accuracy of ± 0.2°C were placed strategically on and around the meat in order to measure how much the RF heated up the tissue and surrounding area. Shown in Figure 4.16, sensor 1 was used as a room temperature reference and was taped to the MRI bed, sensor 2 was used as the tissue temperature reference and was taped to the surface of the pork away from the coil, sensor 3 was taped directly of the surface of the tissue in the center of where the coil would be, and sensor 4 was taped directly to the tissue directly underneath where the coil feed point was. The coil was then placed directly on top of the meat with sensors 3 & 4 reflecting a 'worst-case-scenario' situation, where the only thing separating the coil from the tissue was the coil substrate.

There were three pulse sequences used to test tissue heating and for each sequence and coil the temperature from the sensors were recorded, along with the SAR displayed by the system. The first pulse sequence (PS1) was a modified MNS prescan sequence. The standard MNS prescan contains a 90° hard pulse followed by an off-resonance soft pulse and this repeats twice in 7 seconds, for a total of 4 pulses in the 7 seconds. The sequence was modified to use 180° pulses, which require 4 times the power, and the NEX was increased to 32, meaning the four pulses were repeated 32 times in a row. Additionally the TG was set to a liberal 85, a value that exceeds any TG used in the other experiments.

The next sequence was designed to push the limits more than what was used to acquire images. The TG remained at 85, however the RF pulse duty cycle was altered. For pulse sequence 2 (PS2), a 180° hard pulse was transmitted every 87ms, 1024 times over a course 1.5 minutes. This far exceeds any sort of RF pulse transmissions in any other the other sodium experiments performed.

The final sequence was selected to far exceed any sort of RF power required in the other experiments. The train of 1024 180° pulses was left the same, however the TG was set to the system maximum value of 200.

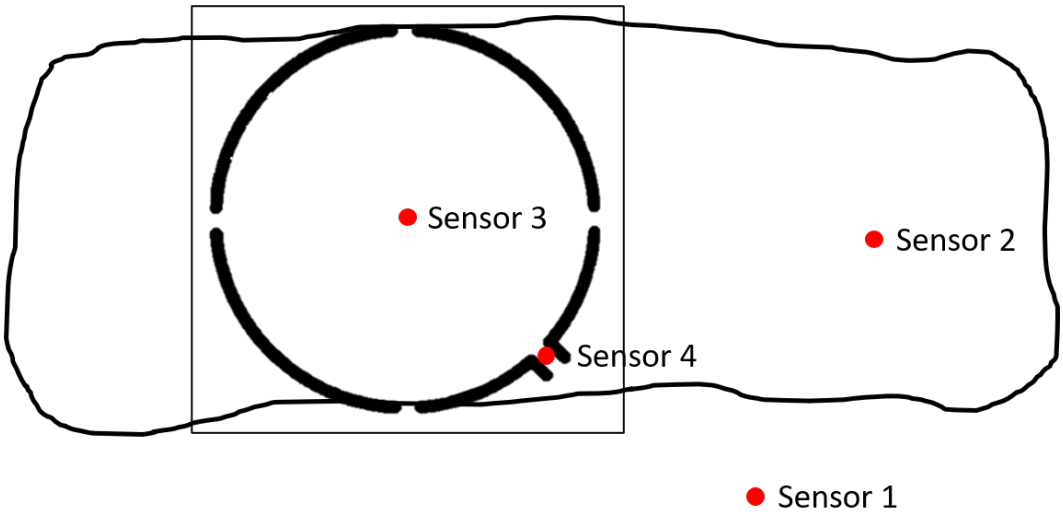

Figure 4.16: **Sensor Location in Tissue Heating Experiment** The locations of the sensors on and around the meat.

Chapter 5

Results

5.1 Simulation Results

Example cross-sections of simulated magnetic fields are shown in Figures 5.1 and 5.2. It can be seen that the fractal coil has a stronger field that appears to penetrate deeper into the phantom. The circular coil however has a larger field of view, in terms of field coverage, per plane. It can also be seen that at a distance of around a radius, the two fields are quite similar in strength. The fractal coil also "fills up" the center space in slices closer to the coil much more effectively than that of the circular coil, due to more coil elements being closer to the center of the design (seen in Figure 4.1).

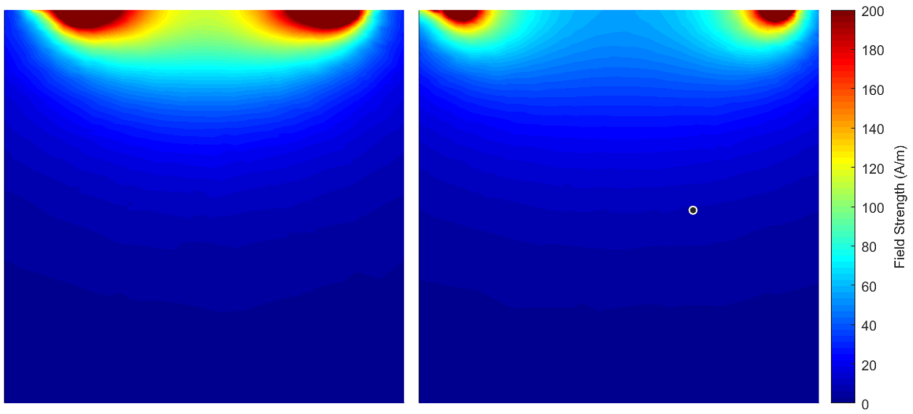

Figure 5.1: **Simulated B Fields (Sagittal)** A sagittal slice of the simulated fields, passing through the center of the coil, with the coil sitting at the top of the slice.

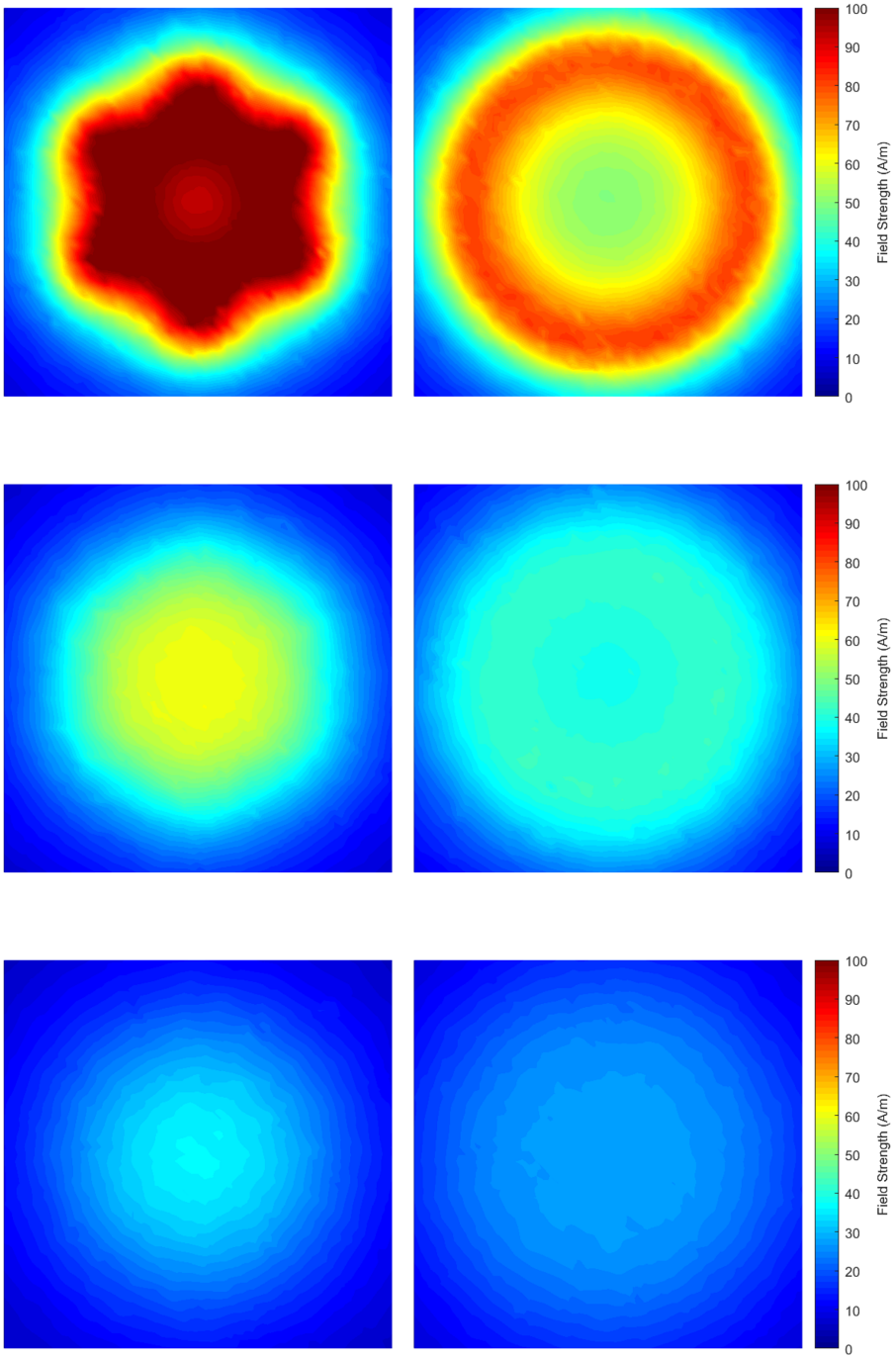

Figure 5.2: **Simulated B Fields (Coronal)** Three coronal slices of the simulated fields with the fractal on the left and the circle on the right. The slices' distance away from the coil plane from top to bottom are 1.5cm, 2.5cm, and 3.5cm

The simulated magnetic field behaviour, with distance from the coil, increases as shown in Figure 5.3. A circular ROI parallel to the coil was used to calculate the average, and maximum/minimum, of the field strength for each millimetre away from the coil, as explained in Section 4.5.1. There were two sizes of ROI used, 24mm in radius (Figure 5.3 A and B) and 45mm in radius (Figure 5.3 C and D). The resultant analysis corroborates the visual analysis of the displayed fields above, that the fractal coil has a stronger field than the circular coil, closer to the coil plane, but by a radius away (45mm) the fields converge in strength. While the fractal's field may be stronger, the lighter bands in Figure 5.3 B and D, which represent the maximum and minimum field values at that distance, show the circular coil has a less drastic variation in field strength indicating a higher field homogeneity. Inside the coils' "sweet spot" indicted by the vertical lines, shows the fractal coil has a greater change in field strength from 24 to 45mm than the circular coil.

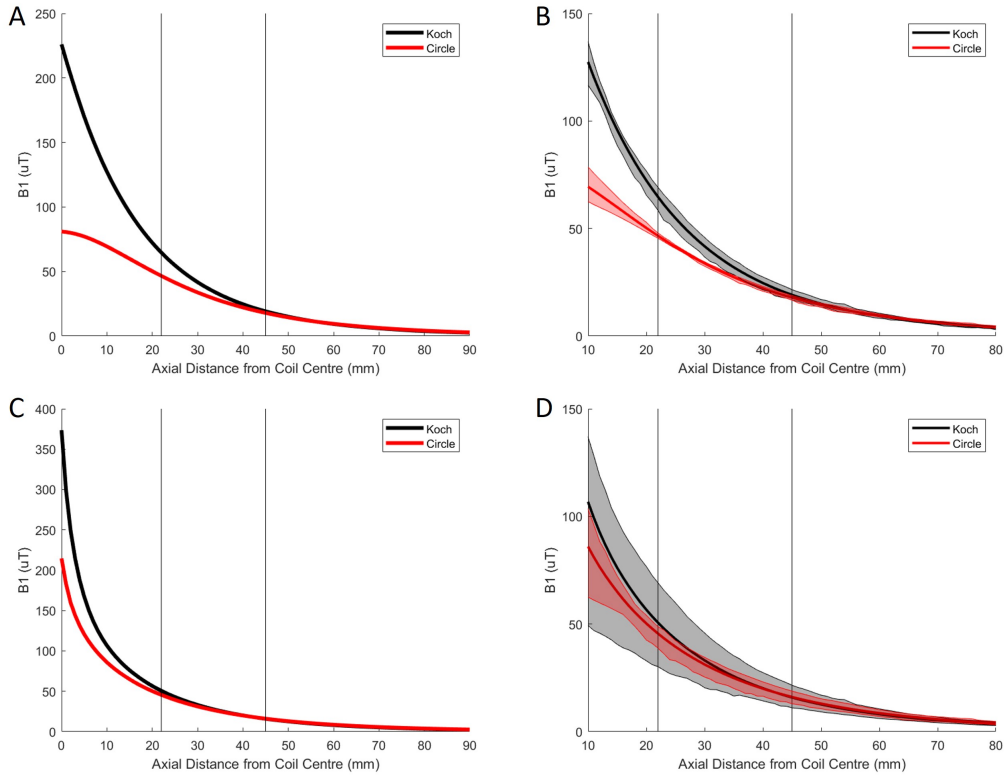

Figure 5.3: **Simulated Field Strength as a Function of Axial Distance** A and B use a circular ROI of radius 24mm to show the average field strength as distance from the coil increases. C and D show the same, but with a circular ROI of 45mm. The lighter bands in B and D show the maximum and minimum field values of each coil at each millimetre away from the coil. The vertical lines in each plot contain the region of the coil's "sweet spot".

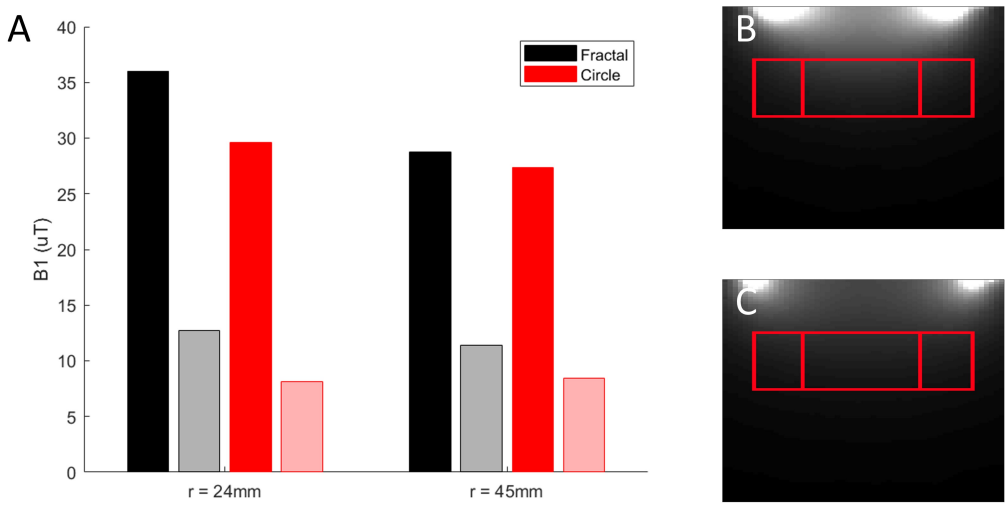

Figure 5.4: **Simulated Field Strength and Homogeneity in Cylindrical ROIs** The average (solid colour bars) and standard deviation (lighter coloured bars) of the magnetic field strength of the two coils (A) over two cylindrical regions of radii 24mm and 45mm. The fractal coil ROIs are shown in B and the circular coil ROIs are shown in C.

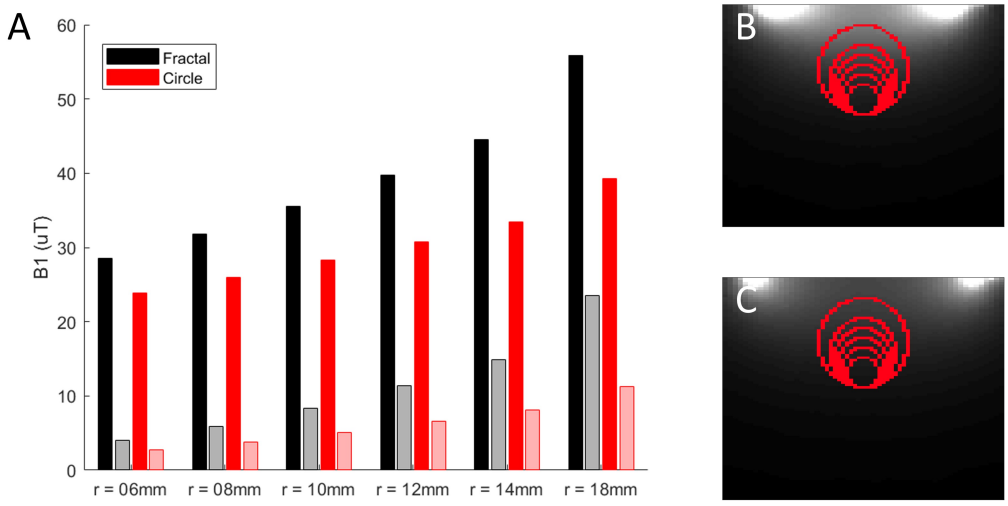

Figure 5.5: **Simulated Field Strength and Homogeneity in Spherical ROIs** The average (solid colour bars) and standard deviation (lighter coloured bars) of the magnetic field strength of the two coils (A) over six spherical regions of radii 6, 8, 10, 12, 14, and 18mm. The fractal coil ROIs are shown in B while the circle coil ROIs are shown in C.

The field strength and homogeneity, based on simulations, were also analyzed over volume ROIs, including two cylindrical (Figure 5.4) and six spherical ROIs (Figure 5.5). The cylindrical regions are located in the coil's "sweet spot". The two cylinders had radii of 45mm - the radius of the coils, and 24mm - a radius that just fit inside the centre of the Koch geometry. The spherical regions all had their lowest point fixed at a radius away from the centre of the coil, and the radii varied from 6mm to 18mm.

In the cylindrical regions, the larger ROI resulted in a weaker average field strength for both coils. The fractal coil had a stronger field in both regions however more so in the smaller ROI. The circular coil had a smaller standard deviation in field strength compared to the fractal coil, in both regions.

In the spherical regions, the larger the ROI, the stronger the average field strength, however the larger the standard deviation - for both coils. The circular coil consistently had a weaker average field strength than the fractal coil for each ROI, but also had a smaller standard deviation in field strength than the fractal coil at each ROI.

5.2 B_1^+ Field Maps

4 B_1^+ maps were made of each coil, and are shown in Figures 5.6 through 5.9. Comparing the sagittal slice of the B_1^+ map of the two coils (Figures 5.6 and 5.7), it can be seen that the fractal coil had a higher average field strength over the FOV compared to that of the circular coil. However, the circular coil had a smaller standard deviation, which can be interpreted as being more homogeneous. The field values can be seen in the bottom right corner of each figure, and are summarized in Table 5.1.

When comparing the coronal slices of the B_1^+ maps (Figures 5.8 and 5.9), it was noted that the circular coil had both a higher average field strength in each of the first two slices, as well as a lower standard deviation across all slices, compared to that of the fractal coil. This indicates both a wider, and more homogeneous FOV produced by the circular coil. The third slice should be taken with "a grain of salt" as the data is clearly quite noisy. But the higher field in the fractal coil with this instance could indicated a slightly deeper field penetration.

	Sagittal	Coronal (1)	Coronal (2)	Coronal (3)
Circular	26.91±10.99	33.37±7.15	25.96±9.30	29.73±12.19
Fractal	31.37±11.80	31.82±7.61	25.64±9.72	30.00±13.18

Table 5.1: **B_1^+ Field Measurements** The average and standard deviation of the B_1^+ fields in each map of each coil given in μT. The three coronal slices are at depths 15mm, 25mm, and 35mm away from the coil respectively.

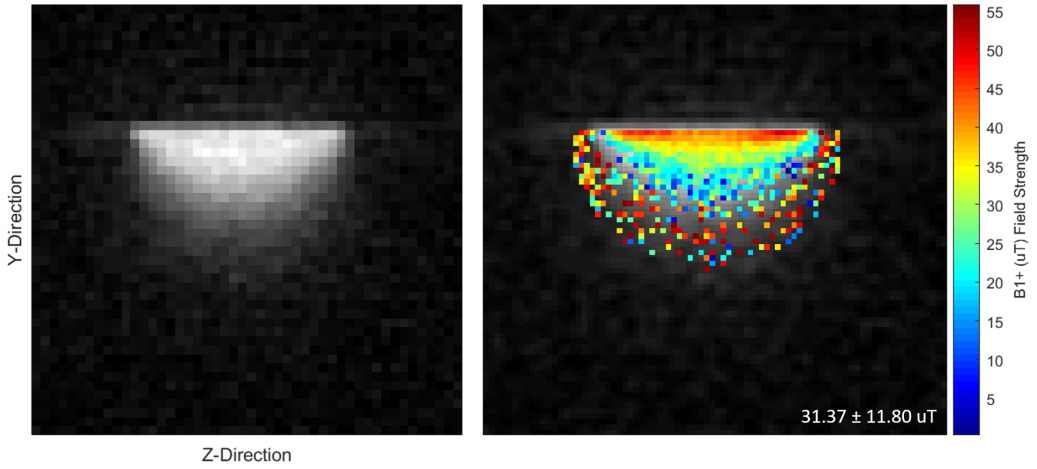

Figure 5.6: **Sagittal B_1^+ Map Overlay (Fractal)** A 1cm thick sagittal slice B_1^+ map of the field produced by the fractal coil. The left image shows the magnitude image, and the map on the right shows the strength of the field. Mean and standard deviation of the shown field given in the bottom right corner.

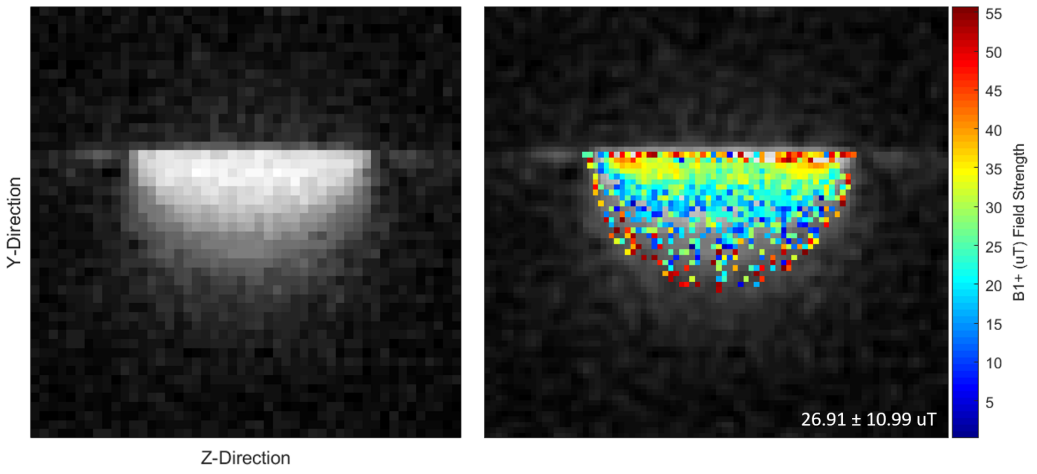

Figure 5.7: **Sagittal B_1^+ Map Overlay (Circle)** A 1cm thick sagittal slice B_1^+ map of the field produced by the circular coil. The left image shows the magnitude image, and the map on the right shows the strength of the field. Mean and standard deviation of the shown field given in the bottom right corner.

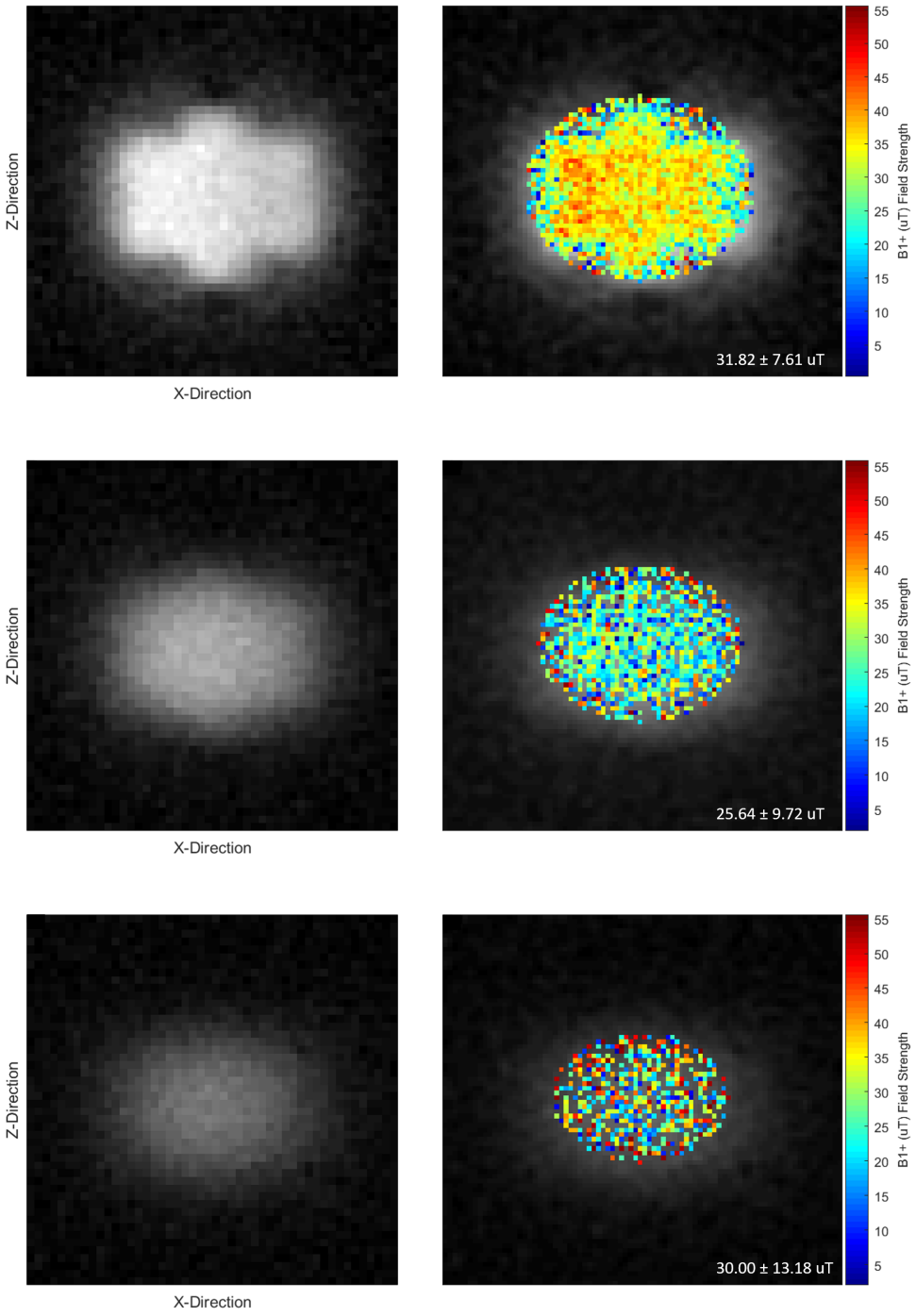

Figure 5.8: **Coronal B_1^+ Map Overlay (Fractal)** Three 1cm thick coronal slices of the fractal coil's B_1^+ map centred at depths (top to bottom) 15mm, 25mm, and 35mm. The left image shows the magnitude image, and the map on the right shows the strength of the field. Mean and standard deviation of the shown field given in the bottom right corner of each map.

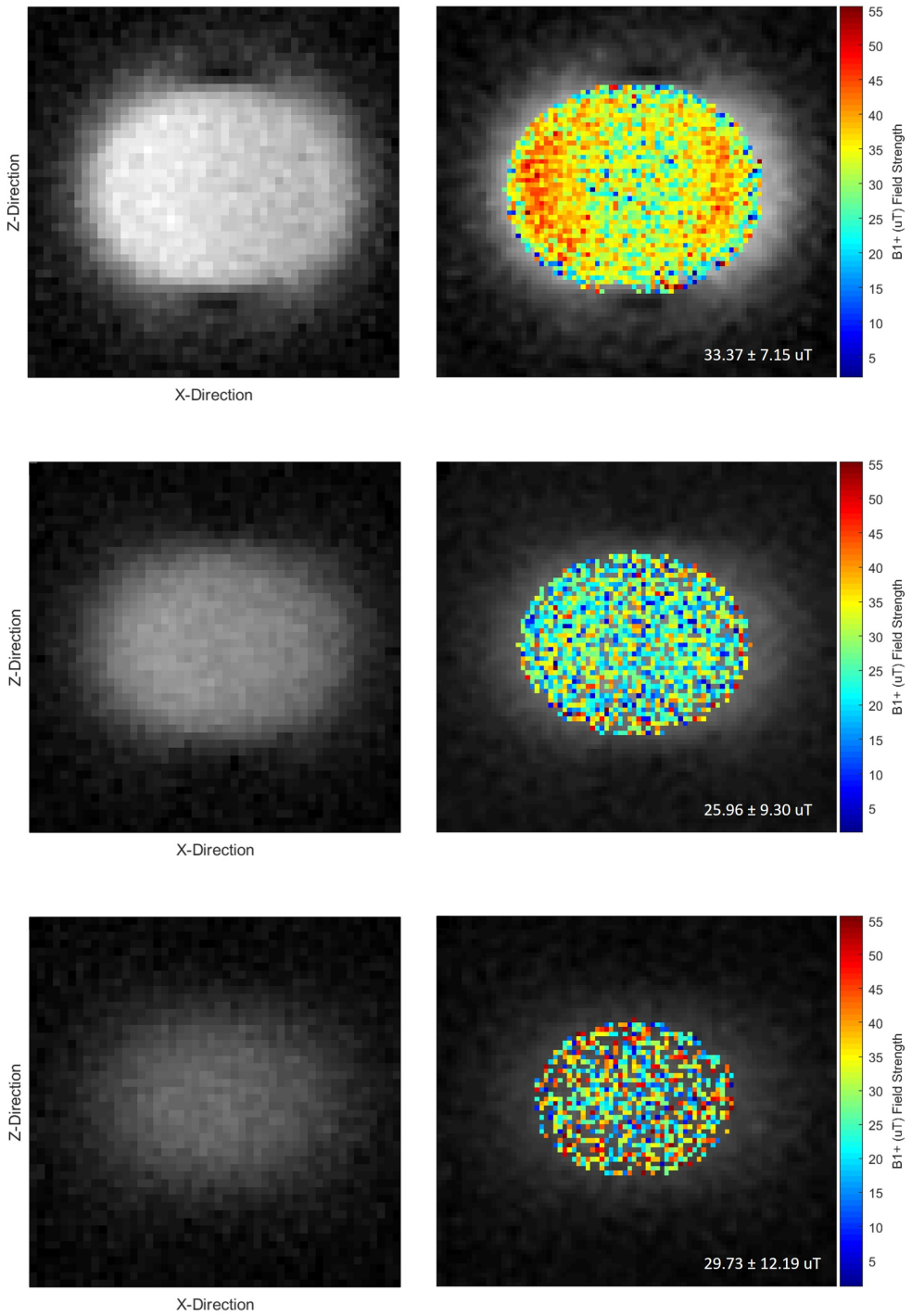

Figure 5.9: **Coronal B_1^+ Map Overlay (Circle)** Three 1cm thick coronal slices of the circular coil's B_1^+ map centred at depths (top to bottom) 15mm, 25mm, and 35mm. The left image shows magnitude and the map on the right shows field strength. Field mean and standard deviation are given in the bottom right corner of each map.

5.3 SNR Measurements

A comparable analysis of experimentally determined magnetic fields (from coils) to that of simulated data, could not be performed with B_1^+ maps as they were not volumetric in nature. However, because MR signal is proportional to sine of the flip angle, and flip angle is proportional to B_1^+, the data acquired using the 3D radial pulse sequence could be used as a surrogate. Figures 5.10 through 5.12 show relatively the same information as Figures 5.3 through 5.5, but on the acquired 3D data instead. Note that instead of B_1^+ on the y-axis of the plots, it is now "signal".

Figure 5.10 shows magnetic field behaviour as distance from the coil increases. Unlike simulation, the curves are fairly similar in strength as the pulse sequence used the same RF flip angle (90°) located at the same distance away from the coils (10mm). When the circular ROI used to calculate the field had a radius of 25mm, the homogeneity of the two coils looked similar (Figure 5.10 B). However, when that ROI expands to a 44mm radius, the circular coil curvature has a tighter band around it, meaning a more homogeneous field (Figure 5.10 D) at that size and thus a larger FOV than that of the fractal.

Figure 5.11 shows the calculated mean and standard deviation of the signal in the "sweet spot" of each coil. It is noted that the circular coil has a higher mean signal, and smaller standard deviation, compared to the fractal coil, over both ROIs. Figure 5.12 shows the calculated mean signal and standard deviation in spherical ROIs. In simulation 6 different sized spheres were used in analysis but due to the resolution of the images, only 3 spheres of different radii were used here: 9.3mm, 12.5mm, and 18.75mm. When analyzing spherical ROIs, the fractal coil consistently had the higher average signal, but the circular coil remained having the lower standard deviation of signal in each of the three ROIs.

Finally SNR for each coil was calculated using ROIs shown in Figures 5.11 and 5.12. The SNR values are presented in Table 5.2 and demonstrate the circular coil consistently had the higher SNR compared to the fractal coil.

Coil / ROI Radius (mm)	9.0	12.5	19.0	25.0	44.0
Circular	17.39	19.31	21.90	17.66	15.09
Fractal	15.46	17.87	21.45	15.30	11.43

Table 5.2: **SNR Calculations** The SNR values of each ROI shown in Figures 5.11 and 5.12. The noise ROI is the ROI shown above the coil FOV. The first three columns of the table are the spherical ROIs and the last two are of the cylindrical ROIs.

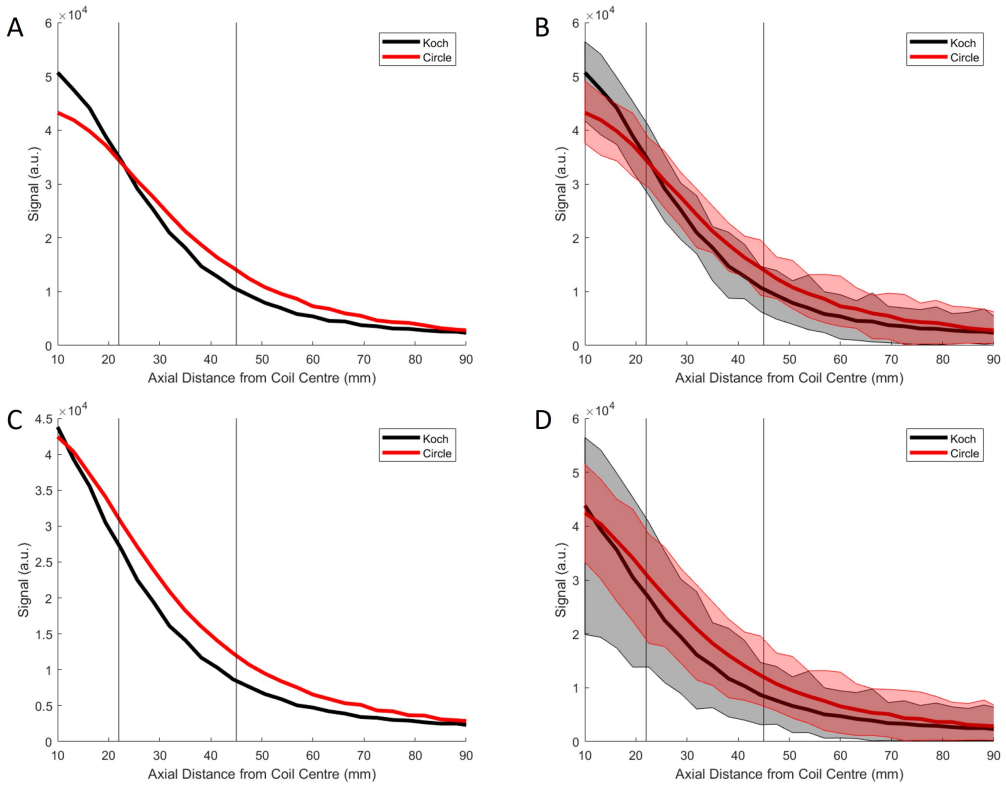

Figure 5.10: **Signal Strength as a Function of Axial Distance** A and B use a circular ROI of radius 25mm to show the average field strength as distance from the coil increases. C and D show the same, but with a circular ROI of 44mm. The lighter bands in B and D show the maximum and minimum field values of each coil at each millimetre away from the coil. The vertical lines in each plot contain the region of the coil's "sweet spot".

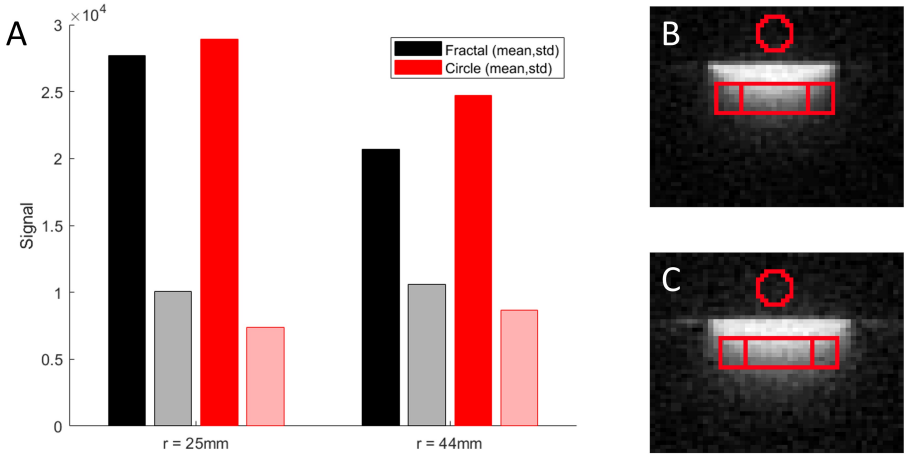

Figure 5.11: **Signal Strength and Homogeneity in Cylindrical ROIs** The average (solid colour bars) and standard deviation (lighter coloured bars) of the signal from the two coils (A) over two cylindrical regions of radii 25mm and 44mm. The fractal's ROIs shown in B and the circle's ROIs shown in C. The spherical ROI above the signal is the noise ROI used in SNR calculations.

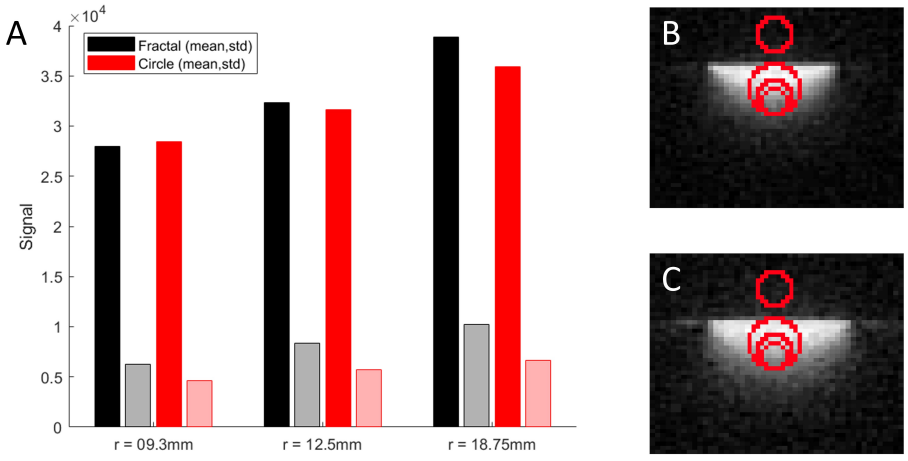

Figure 5.12: **Signal Strength and Homogeneity in Spherical ROIs** The average (solid colour bars) and standard deviation (lighter coloured bars) of the signal from the two coils (A) over three spherical regions of radii 9.3mm, 12.5mm, and 18.75mm. The fractal's ROIs shown in B and the circle's ROIs shown in C. The spherical ROI above the signal is the noise ROI used in SNR calculations.

5.4 Bandwidth Homogeneity

Figures 5.13 and 5.14 show a sagittal slice through the edge of the homogeneity phantom taken with a 3D acquisition with 4 FOVs of both coils. Signal strength along a path from the centre of the phantom edge, 10mm on each side of the phantom edge, is plotted in Figure 5.15, along with the ideal representation of the signal (i.e. a heavy-side function). By calculating the R^2 of the real data to the ideal model, the homogeneity of the coils' field over bandwidth was compared. Table 5.3 shows the R^2 of each FOV of each coil fitted to the ideal heavy-side function. It is seen that the fractal coil has a better fit over all FOVs.

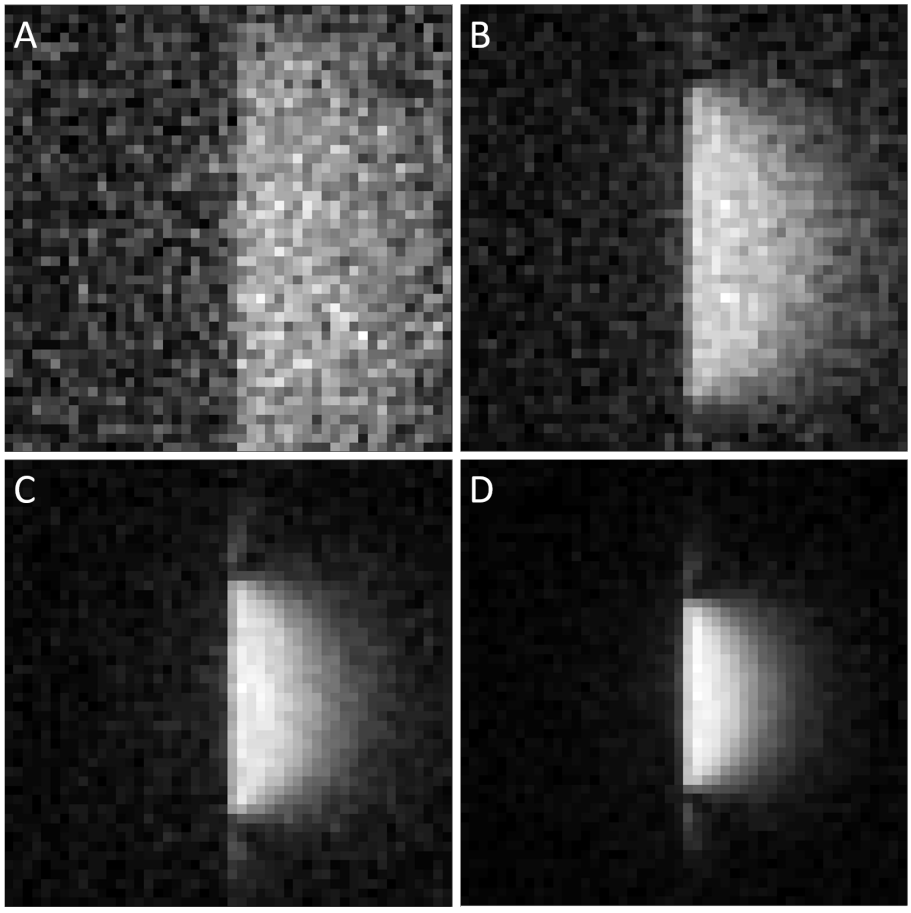

Figure 5.13: **BW FOVs of the Circular Coil** A sagittal slice through the homogeneity phantom using the circular coil, acquired with the 4 different FOVs of: (A) 8cm, (B) 12cm, (C) 16cm, and (D) 20cm.

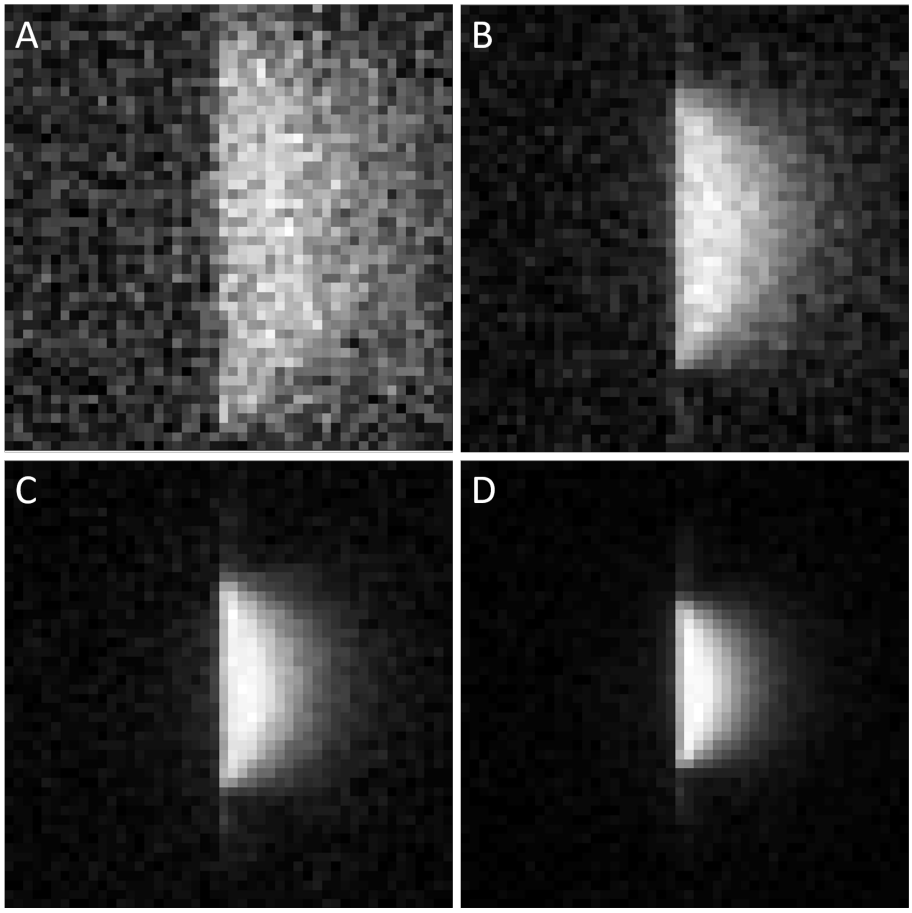

Figure 5.14: **BW FOVs of the Fractal Coil** A sagittal slice through the homogeneity phantom using the fractal coil, acquired with the 4 different FOVs of: (A) 8cm, (B) 12cm, (C) 16cm, and (D) 20cm

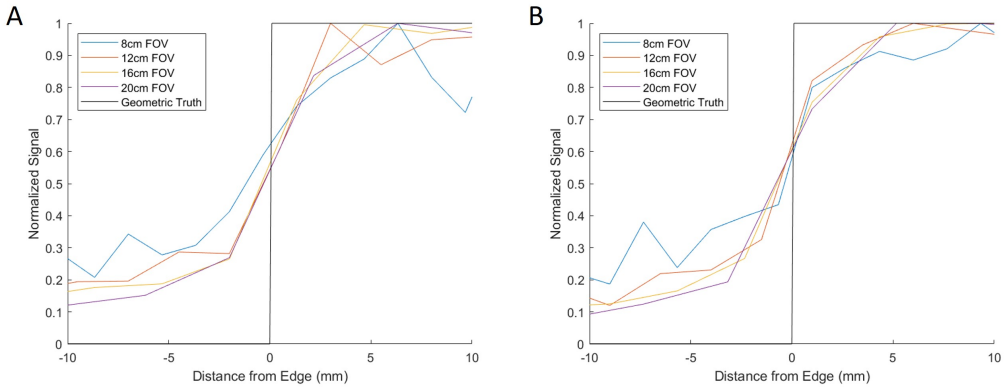

Figure 5.15: **Edge Step Curves for BW Homogeneity** The voxel signals that cross perpendicular to the center of the phantom's edge 10cm before and after the edge at the 4 different FOVs for the (A) circular and (B) fractal coil.

Coil / FOV (cm)	8	12	16	20
Circular	0.0118	0.5235	0.7477	0.8446
Fractal	0.2231	0.7526	0.7843	0.8654

Table 5.3: **R^2 Values of Edge Step Curves** The calculated R^2 values of each FOVs' edge step function compared to the ideal heavy-side function.

For a coil comparison of the ability to represent geometric truth over varying bandwidths, the following figures (5.16 through 5.20) are shown. The centre 8cm FOV of the proton image of the geometric phantom is shown in Figure 5.16 and is, for this comparison, the "ground truth" the images produced at varying FOVs (from both coils) were subtracted against. Seen in Figures 5.17 and 5.18 are the centre 8cm images of the four FOVs, resized to 48x48 and normalized, of the circular and fractal coil respectively. These are the images that were subtracted from the "geometric truth" in the previously mentioned figure. The resultant subtraction images of the circular and fractal coil FOV images are presented in Figures 5.19 and 5.20 respectively. It is noted that both 8cm FOV acquisitions of the coils have no real geometric representation at all, the signal was too weak and images noise dominated. The larger FOVs all show a little more geometrical representation but a comparison between both coils seemed moot as both have quite similar subtraction images, at least at first inspection. However, by comparing the calculated metric of "percentage misrepresentation" in Table 5.4, it can be seen (ignoring the noisy, low signal 8cm FOV) that the fractal had a lower percentage than that of the circular coil for each of the other three FOVs.

Coil / FOV (cm)	8	12	16	24
Circular	49.00	50.95	52.60	55.03
Fractal	49.13	45.62	44.23	51.17

Table 5.4: **Percentage of Bad Pixels** The percentage of pixels for each coil that did not line up with the geometric truth for each respective subtraction image of the 4 different FOVs.

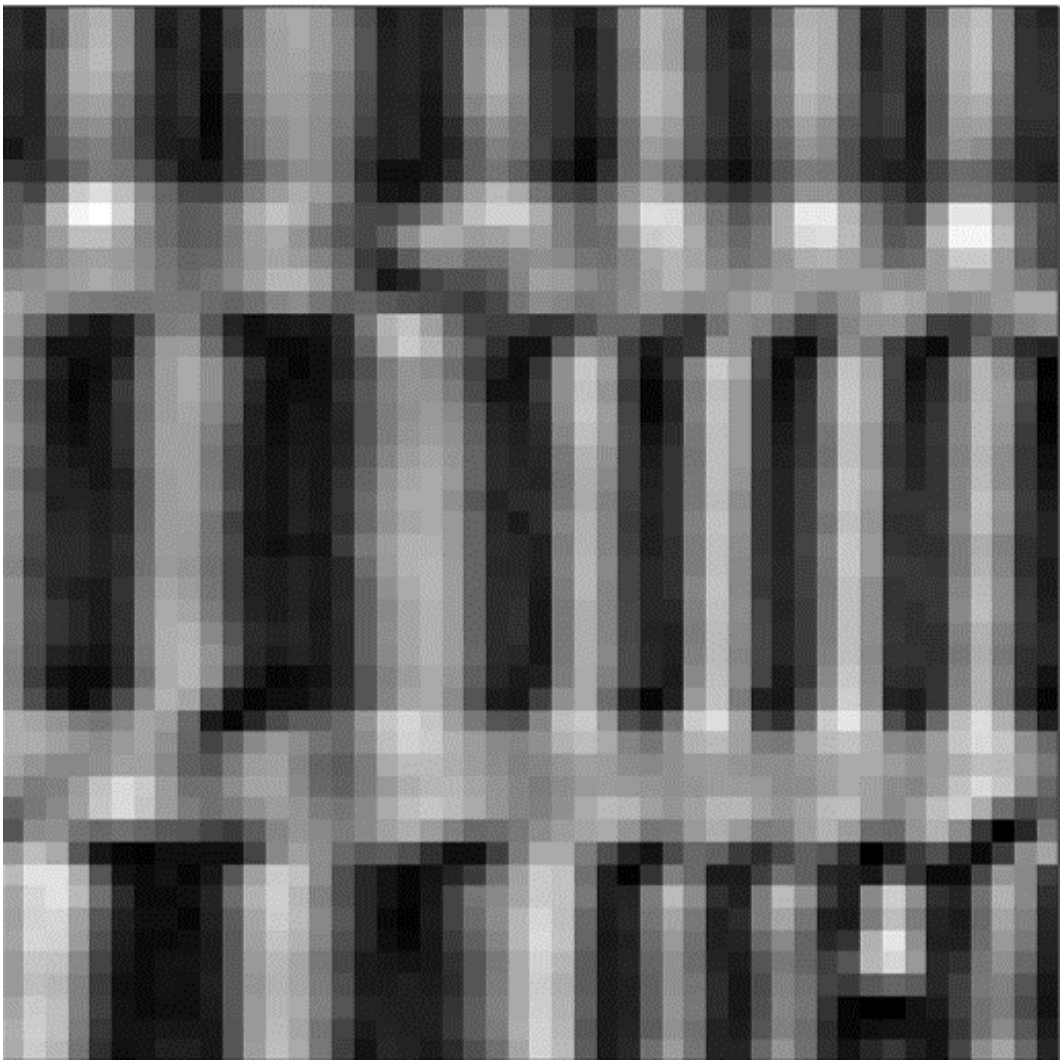

Figure 5.16: **BW Geometrical Truth Phantom** The centre 8cm FOV of the proton image of the geometric phantom used as a representation of geometric truth. Image was resized from 42x42 to 48x48.

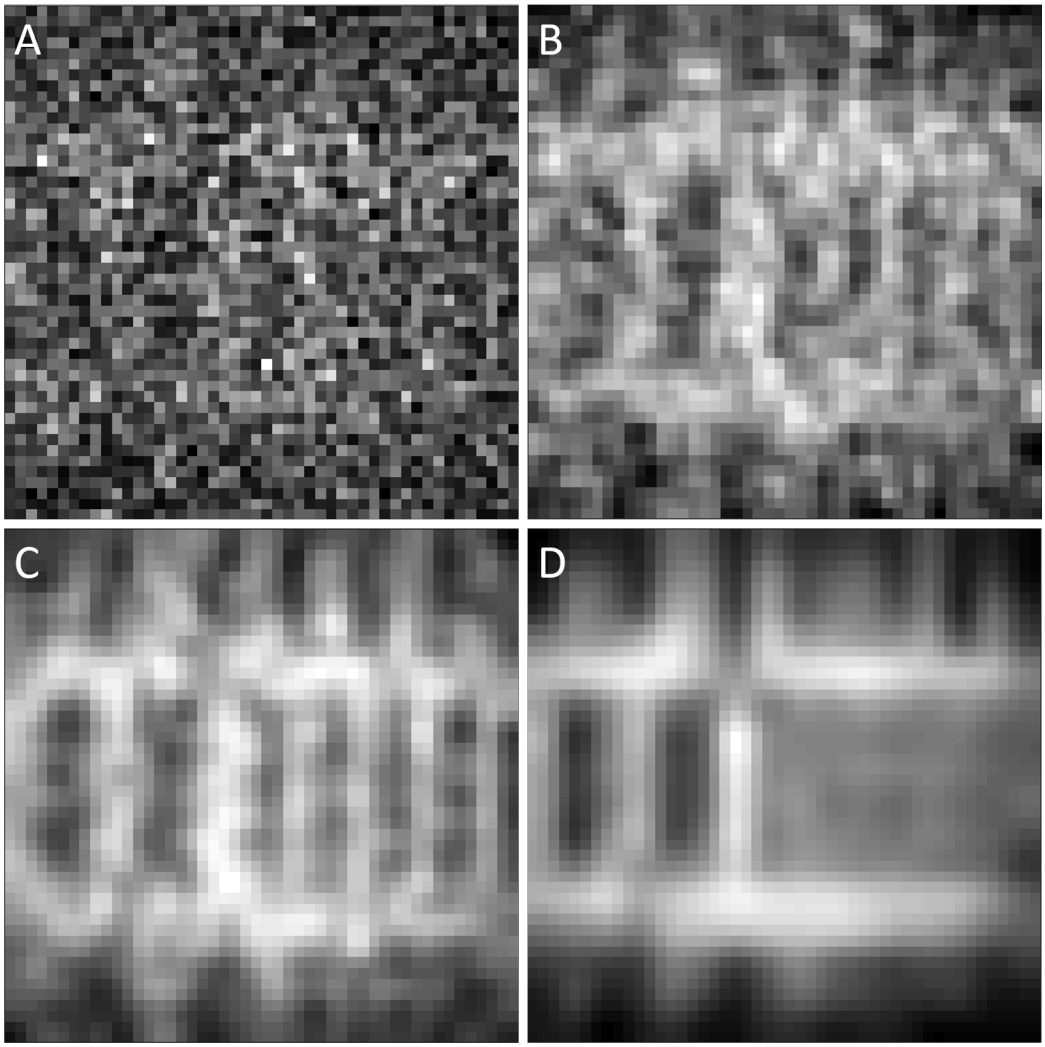

Figure 5.17: **Geometric BW FOVs of the Circular Coil** The centre 8cm FOV of the four coronal slices of the geometric phantom imaged with the 3D radial sodium sequence and the circular coil with an FOV of (A) 8cm, (B) 12cm, (C) 16cm, and (D) 24cm. B,C,and D were resized from 32x32, 24x24, and 16x16 respectively to 48x48.

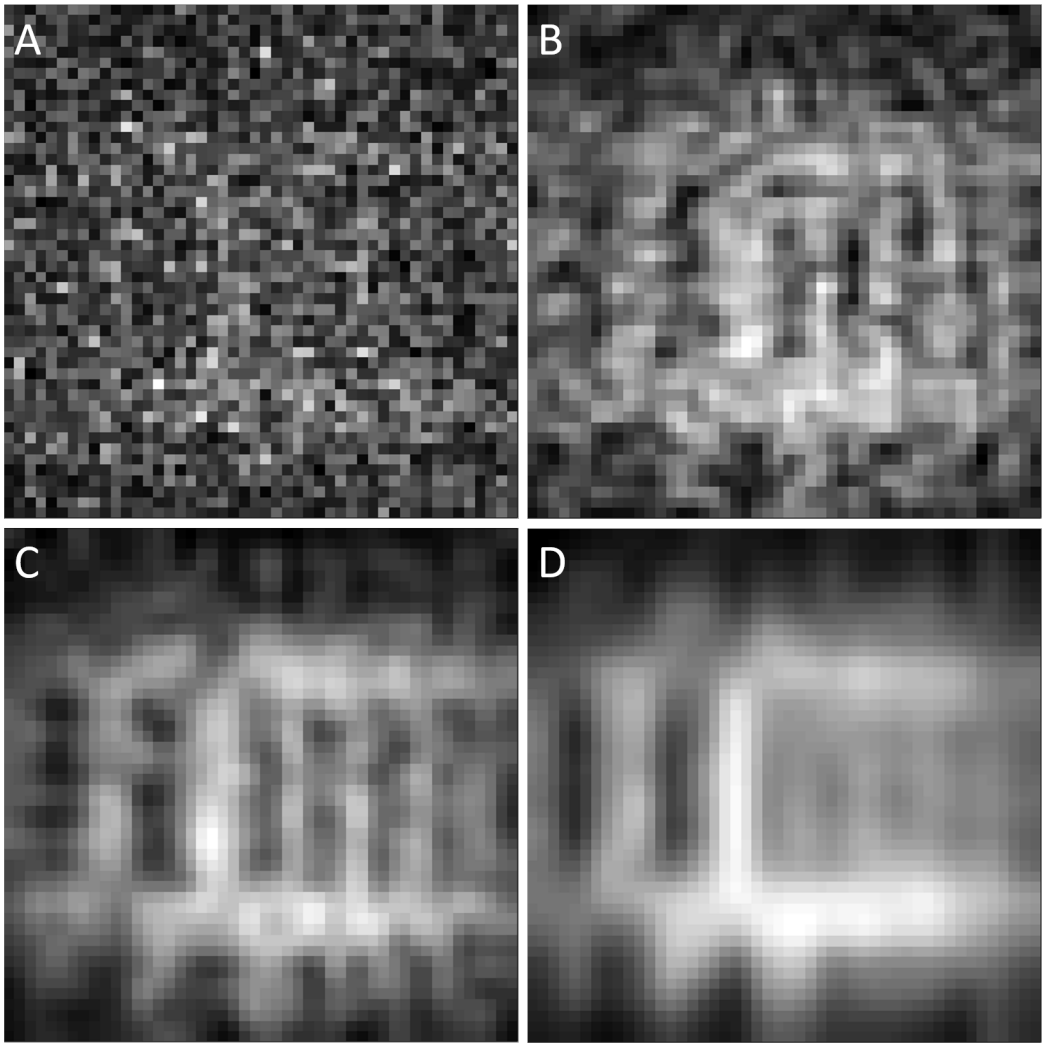

Figure 5.18: **Geometric BW FOVs of the Fractal Coil** The centre 8cm FOV of the four coronal slices of the geometric phantom imaged with the 3D radial sodium sequence and the fractal coil with an FOV of (A) 8cm, (B) 12cm, (C) 16cm, and (D) 24cm. B,C,and D were resized from 32x32, 24x24, and 16x16 respectively to 48x48.

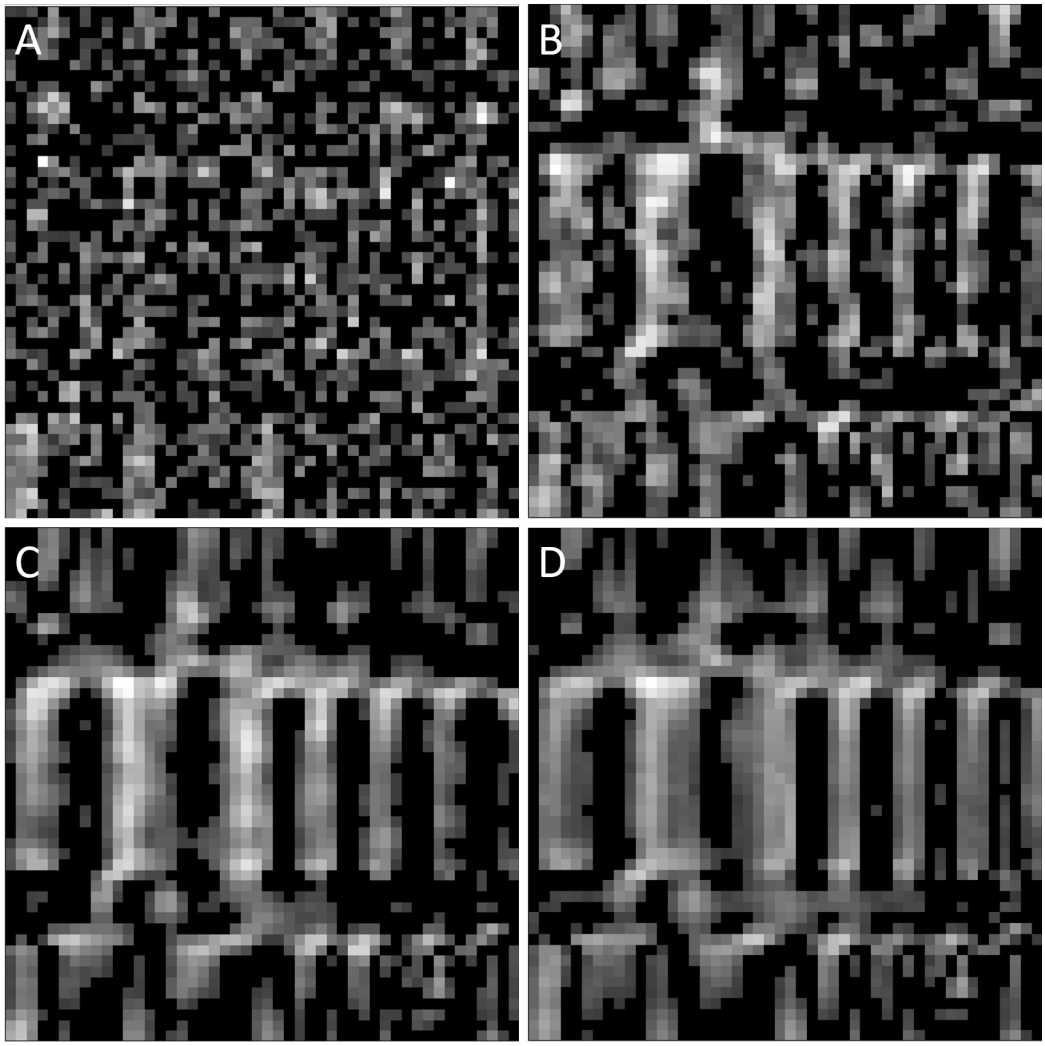

Figure 5.19: **BW Subtraction Results of the Circular Coil** The resultant subtraction image of the circular coil's FOV images of (A) 8cm, (B) 12cm, (C) 16cm, and (D) 24cm from the geometric truth image.

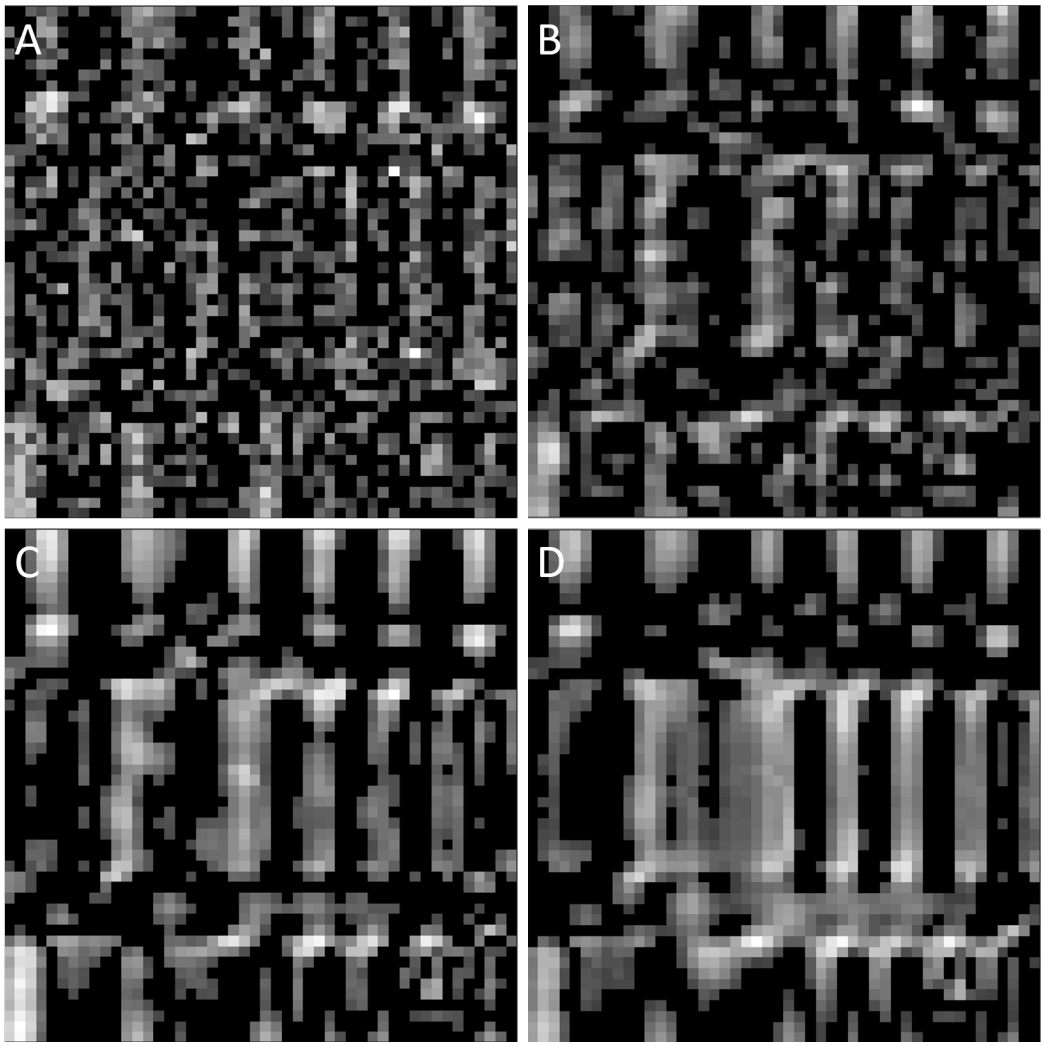

Figure 5.20: **BW Subtraction Results of the Fractal Coil** The resultant subtraction image of the fractal coil's FOV images of (A) 8cm, (B) 12cm, (C) 16cm, and (D) 24cm from the geometric truth image.

5.5 Sodium imaging of a Healthy Human Knee

Figure 5.25 shows the sodium voxel intensity distribution through a 3D volume of the knee obtained with both the circular and fractal coils. By using the method described in Section 4.5.5, the SNR of knee volumes from each of the two coils was calculated and is presented in Table 5.5. For this application the fractal coil had notably higher SNR.

Figures 5.21 through 5.24 show a selection of knee sodium images alone and overlayed on their corresponding proton knee images. It is clear that the majority of signal comes from the cartilage and synovial fluid surrounding the head of the femur. Interestingly the circular coil looks as though it has more signal, but since the SNR is higher in the fractal it implies the fractal coil images are less noisy. Comparing the coils visually, both produce images that "make anatomical sense" and fit the knee correctly. Although from a qualitative standpoint the circular coil appears more anatomically appropriate.

Coil	SNR	μ_{signal}	σ_{noise}
Circular	13.9283	19892	1428
Fractal	14.8859	19450	1307

Table 5.5: **SNR of the Knee** The SNR of each coil's knee image as calculated from Figure 5.25.

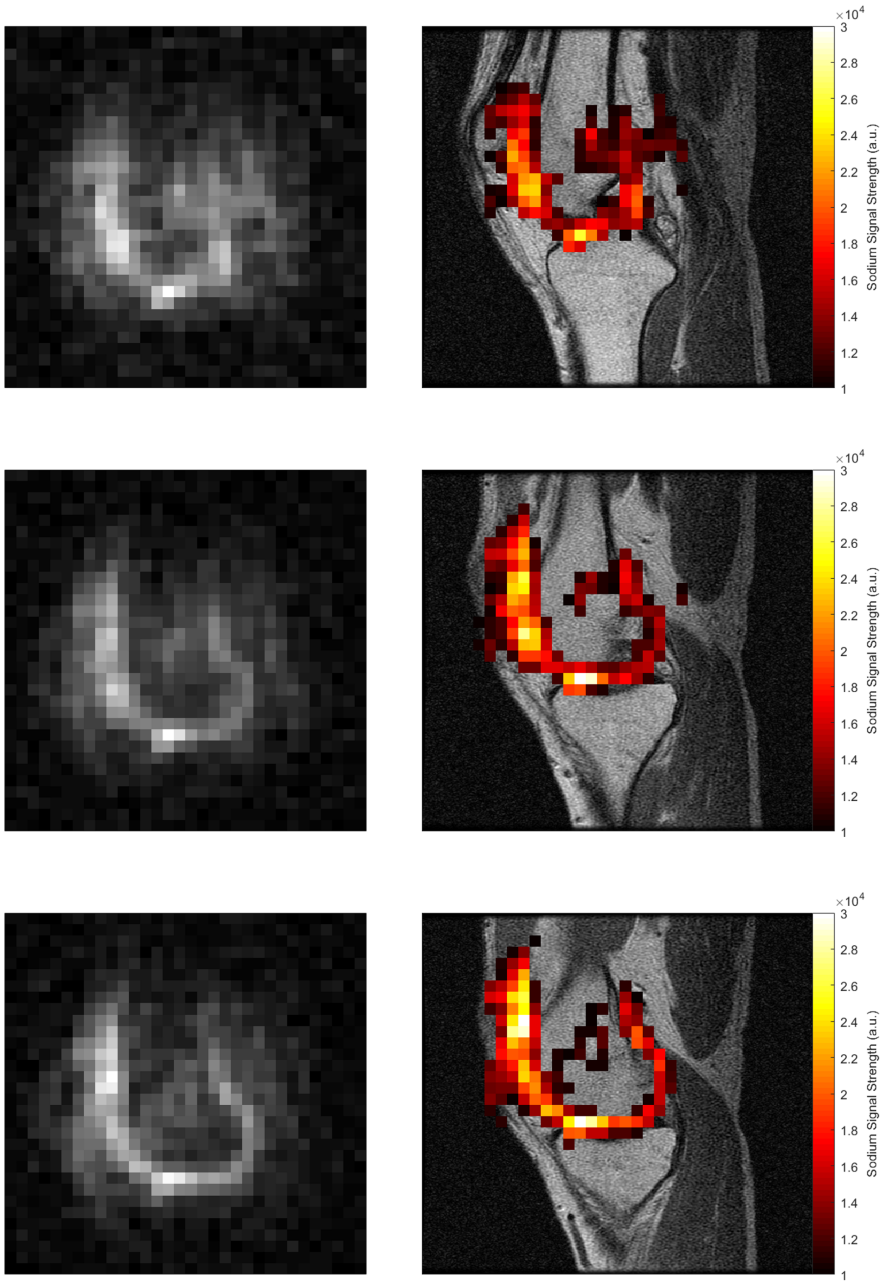

Figure 5.21: **Sodium of the Knee Slices 11-13 (Circular Coil)** Three selected sagittal slices of the sodium image produced by the circular coil. The left images in each pair show the raw sodium image, and the right image shows the sodium overlayed on top the proton image, with a signal threshold of 10000 (arbitrary units).

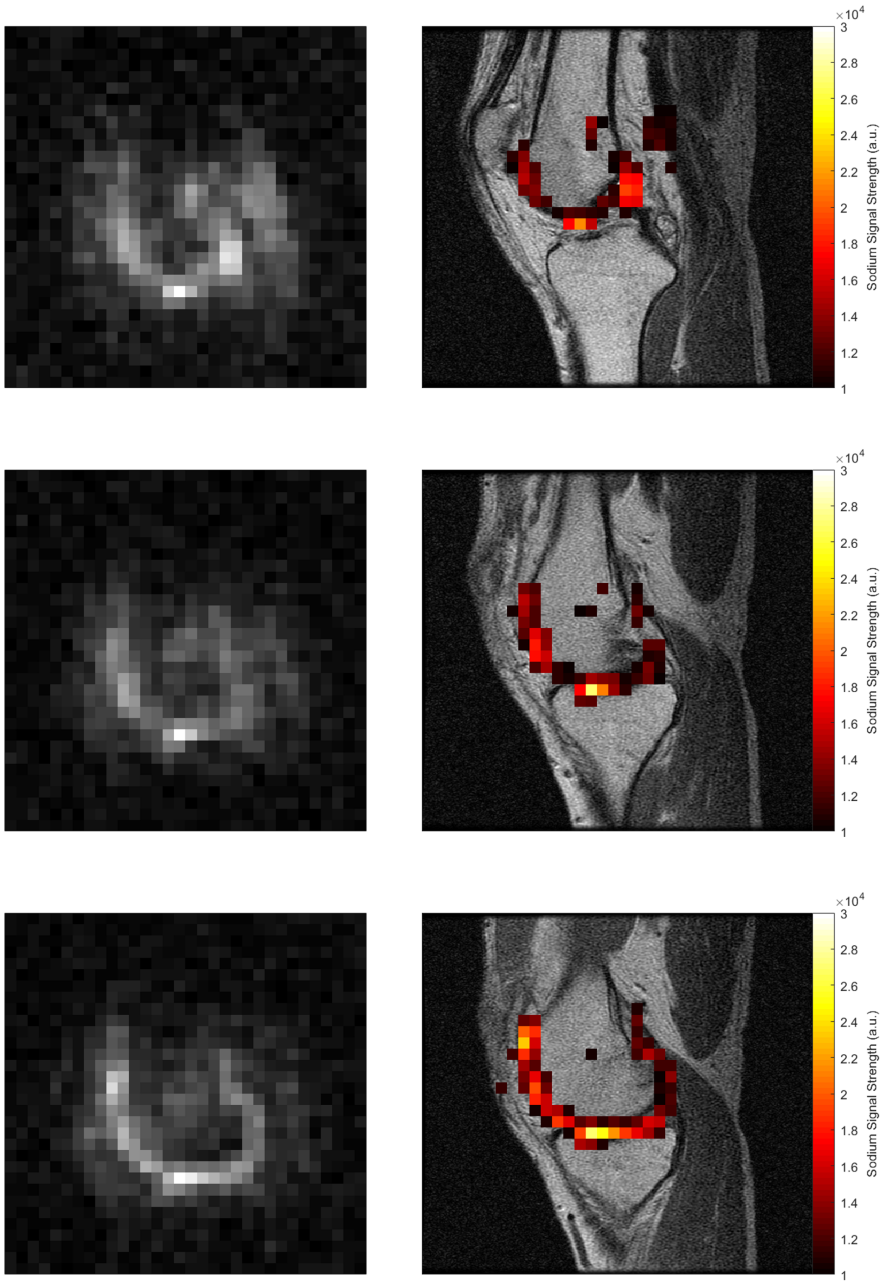

Figure 5.22: **Sodium of the Knee Slices 11-13 (Fractal Coil)** Three selected sagittal slices of the sodium image produced by the fractal coil. The left images in each pair show the raw sodium image, and the right image shows the sodium overlayed on top the proton image, with a signal threshold of 10000 (arbitrary units).

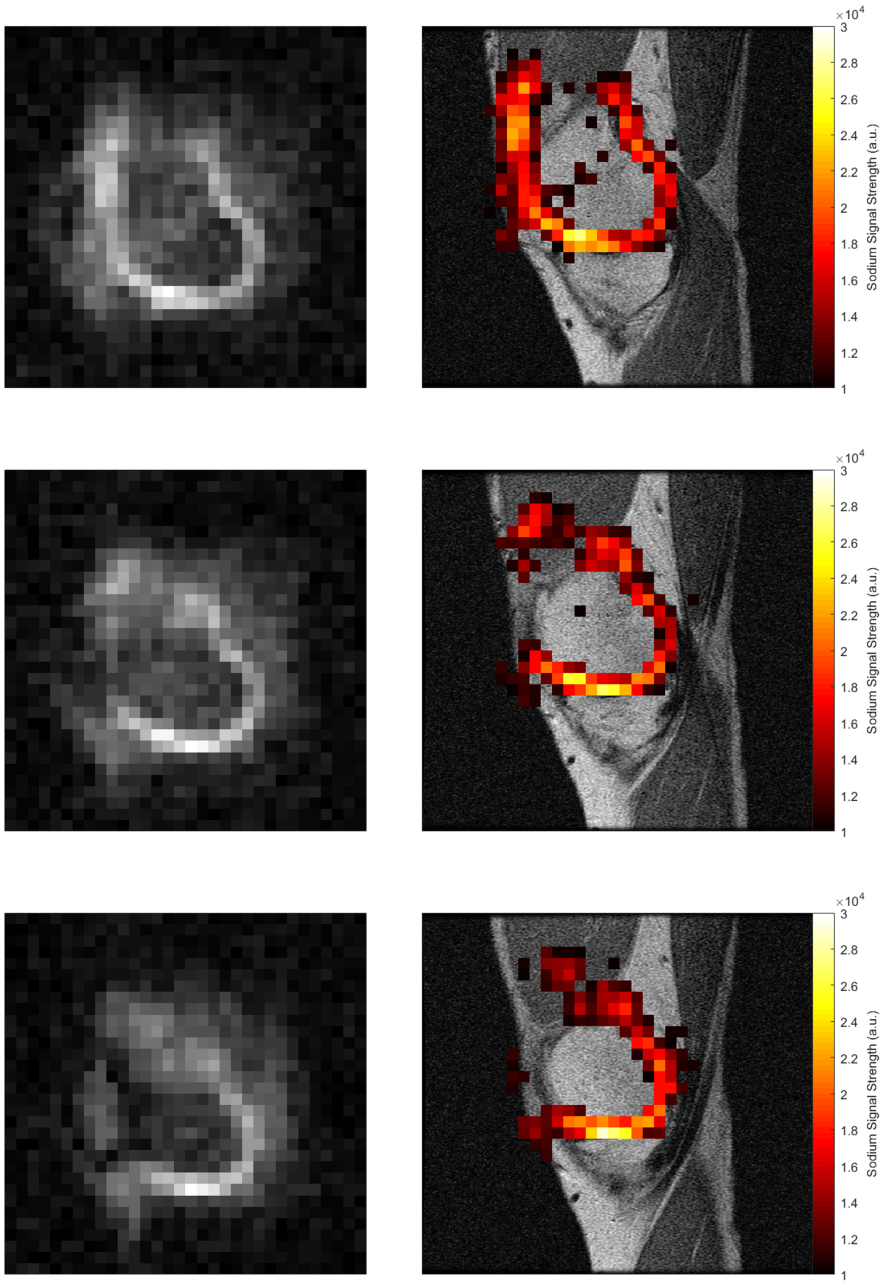

Figure 5.23: **Sodium of the Knee Slices 14-16 (Circular Coil)** Three selected sagittal slices of the sodium image produced by the circular coil. The left images in each pair show the raw sodium image, and the right image shows the sodium overlayed on top the proton image, with a signal threshold of 10000 (arbitrary units).

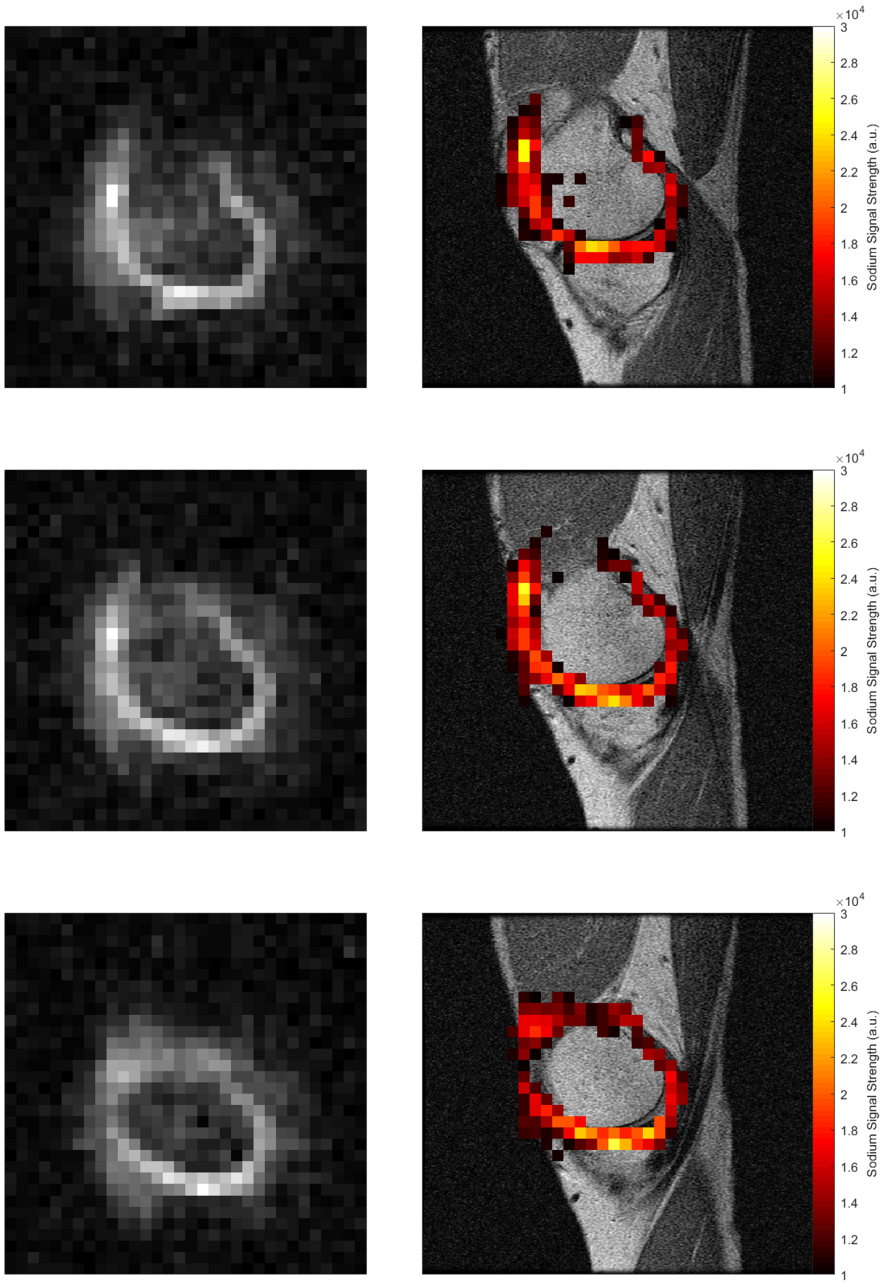

Figure 5.24: **Sodium of the Knee Slices 14-16 (Fractal Coil)** Three selected sagittal slices of the sodium image produced by the fractal coil. The left images in each pair show the raw sodium image, and the right image shows the sodium overlayed on top the proton image, with a signal threshold of 10000 (arbitrary units).

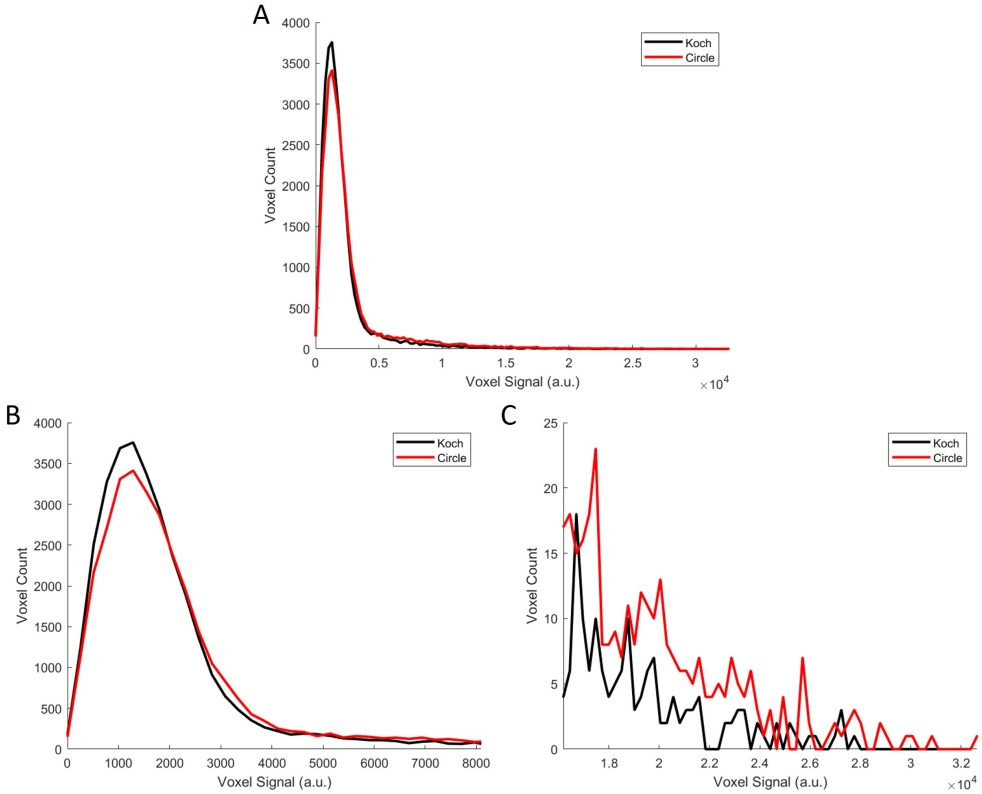

Figure 5.25: **Knee Voxel Signal Distribution** (A) The number of voxels at each intensity over the full range of intensities in the 3D volume. (B) The range of intensities used for the noise ROI. (C) The range of intensities used for the signal ROI.

5.6 Coil Safety

Table 5.6 shows the recorded temperatures of each optical sensor during the three pulse sequences tested on each coil. Pulse sequence 1 showed no change in temperature or any measurable SAR for both coils. Pulse sequence 2 also did not result in any change in temperature, but there was a registered SAR, as calculated by the MRI system, of 0.1W/kg over 10 seconds. Both coils had the same reported SAR values. The final pulse sequence showed heating (of the pork meat), but just by the sensor located underneath the feed point of the coil. The circular coil increased temperature by 2.4°C and the fractal coil increased the temperature by 2.6°C. The SAR calculated by the system was 0.9W/kg and 1.1W/kg, for each respective coil, over the 1.5minutes of the experiment. It should be noted that the third sequence was an extreme case that would not be done under any clinical circumstance but rather was done to determine whether any tissue heating could occur.

		PS1				PS2				PS3			
Sensor→		1	2	3	4	1	2	3	4	1	2	3	4
Circle	Before (°C)	17.6	12.7	12.1	12.6	17.6	13.1	12.7	13.2	17.6	14.2	13.9	14.2
	After (°C)	17.5	12.8	12.1	12.6	17.6	13.2	12.8	13.3	17.7	14.2	13.3	16.6
	ΔT (°C)	0.1	0.1	0.0	0.0	0.0	0.1	0.1	0.1	0.1	0.0	0.0	2.4
	SAR (W/kg)	0.0				0.1				0.9			
Fractal	Before (°C)	17.5	12.6	12.1	12.7	17.5	12.8	12.1	12.7	17.7	14.7	13.9	15.1
	After (°C)	17.6	12.6	12.2	12.6	17.6	12.9	12.1	12.9	17.7	14.8	13.9	17.7
	ΔT (°C)	0.1	0.0	0.1	0.1	0.1	0.1	0.0	0.2	0.0	0.1	0.0	2.6
	SAR (W/kg)	0.0				0.1				1.1			

Table 5.6: **Coil Tissue Heating and SAR** The changes in temperature measured by optical thermal sensors for the three pulse sequences, and the calculated SAR (averaged over a 10s period) given by the MRI system.

Chapter 6

Discussion and Future Research

6.1 Conclusions

The goal of this project was to investigate the potential advantages of having a fractal geometry RF surface coil for ^{23}Na-MRI as opposed to a standard circular geometry. The overlying hypothesis was that the fractal would produce a more homogeneous B_1^+ field in both space and frequency, which would correlate to higher SNR and therefore improved image quality. Through both simulation, construction and implementation, with a number of different pulse sequences, the fields and signal generation of a fractal and circular surface coil were measured.

From simulation results it is noted that over the eight ROIs examined, the fractal coil had a stronger average magnetic field, but the circular coil had a lower field standard deviation across all ROIs. This implies the circular coil produces a more homogeneous field than that of the fractal coil. While not the hypothesized result, simulation needed experimental validation via construction and testing coils in the MRI environment.

The first coil experiment was B_1^+ mapping. While it varied which coil had the higher average field in each map, both sagittal and coronal, the circular coil consistently had the lower standard deviation of field strength which agreed with the conclusions made from the simulations. The data from the B_1^+ mapping sequences however, should be taken with a slight grain of salt as the resultant images had high noise levels and were obtained over a 1cm thick slice. This made comparison with ROI analysis of simulated data more difficult and necessitated average field strength and homogeneity to be calculated over the entire field of view.

While the B_1^+ maps could not be directly compared to the fields produced in simulation, the fields could be compared indirectly, in a round about way, using the 3D images produced by the coils. Since MR signal is proportional to the sine of the flip angle, and flip angle is proportional to B_1^+ field strength, the

signal in each voxel of the 3D sodium images could be a representation of the field strength within that voxel. And while limited by resolution, the same kind of ROI analysis that was performed on the simulation data could be performed on the 3D images. The analysis of simulations showed that the fractal had a higher average field, but when analyzing the experimental data the strength of the field, with both fractal and circular coils, was depending on the ROI. This was most likely due to the fact that the 90° flip angle did not have a known exact location, and the TG of each coil was different based on prescan results. However, what was consistent between simulation and experiment, was that the circular coil had a lower standard deviation over all ROIs which lead to the conclusion that the circular coil had a more homogeneous field. The 3D images were also used to calculate the SNR of the 3D images produced by each coil. As expected from the previous experiments, the coil with the more homogeneous field, the circular coil, had the higher SNR.

A more homogeneous field in space was only half of the hypothesis, and experiments needed to be performed to test the homogeneity of the two coils' fields over frequency, i.e. a wider bandwidth. Two experiments to test this were performed. The first test was to see how well the coils could represent a sharp edge over a changing FOV size, to emulate a changing transmit bandwidth. By calculating the R^2 value of the resultant images compared to an ideal case, showed that the fractal coil better represented the edge step. A consequence of poor BW homogeneity would be geometric aberrations as the BW gets restricted. Thus, a second experiment was done to test how well the coils could represent intricate geometry as the FOV changed. This experiment also showed the fractal coil performing better than the circular coil. This would lead to one to conclude the fractal coil superior over a circular coil, over a wider BW. However, because the transmit bandwidth couldn't actually be changed, no definitive conclusions could be drawn. The results show promise and a more robust experiment needs to be performed to either confirm or contradict what is reported here.

The final experiment was to test the coils *in vivo*, to see how well they would perform in a clinical setting. The coils were used to image a knee, and while the results were quite noisy and low resolution, both coils produced accurate images of the knee's synovial fluid and cartilage. The circular coil appeared to have a bit more information in its images, but the fractal coil had better SNR. This was surprising based on the previous results (i.e. the circular coil should have had better SNR). But this is most likely due to variation in coil loading from the phantoms to the knee, and between coils. Regardless, it was shown that both coils worked, although in a somewhat limited fashion, on human anatomy.

In conclusion, the results of this thesis can be summarized (see Table 6.1) by stating that a circular RF coil produces a more homogeneous B_1^+ field over

space, with higher SNR, than that of a similarly sized fractal coil. Furthermore, there is some evidence suggesting a more uniform transmit bandwidth with the fractal coil. However, further research needs to be conducted to test this concept.

Coil	Sim. H.	B_1^+ H.	Signal H.	SNR	BW1	BW2	Knee SNR
Circular	X	X	X	X			
Fractal					X	X	X

Table 6.1: **Summary of Results** A summary of which coil performed better in each experiment run. "H." stands for homogeneity.

6.2 Future Research

Although there was a great deal of progress made to assess a fractal based RF coil design for sodium MRI, the work led to a need for further experimentation. First, a more robust and conclusive experiment needs to be conducted to investigate bandwidth homogeneity of the fractal coil. The results presented in this thesis show enough promise that this is unquestionably worth further investigation. Because of the single resonant peak this may not have as big of an application in sodium MR imaging. However, other nuclei like ^{31}P and ^{13}C have signal spectra that are kilohertz in width and a more homogeneous B_1^+ field over a wider bandwidth would prove to be immensely beneficial for increasing the quality of those types of MR scans.

It has also been shown that fractal RF coil geometry, specifically the Koch snowflake, has application in phased-array volume coil designs [24]. The fractal geometry results in a decrease in the amount of mutual inductance between overlapping coils. Phased-array coils are more prevalent in MRI applications than single surface coils, but prove to be quite tedious to construct - especially to tune and match. When two coils are coupled together, every change in capacitance on one coil will affect the tune and match of the other. If fractal geometries can reduce the mutual inductance, than the effect that one coil has on the other will be reduced and as such, tuning and matching will become easier. This would be quite beneficial and worth investigating in the future.

6.3 Challenges and Limitations

6.3.1 In Simulation

The goal of the simulations were to replicate the conditions in which the two coils would be used as accurately as possible. However there were a few differences between simulation and implementation due to computational limitations and time restraints.

- The coil was simulated as infinitesimally thin copper to avoid the mesh having to reduce its smallest dimension to what would be an insignificant thickness and lengthen the run time substantially.
- To avoid any boundary issues such as reflectance, the sodium load, air box, and substrate were increased until the change in the s_{11} was negligible. However this required the tune and match to change with every increase in geometry size as well as the run time would increase as well. Finally it was decided to set the boundaries at three coil diameters away in all directions.
- The biggest challenge posed was the run time of the simulations. Each took over 3 hours to run, and tuning and matching required 10's of runs and so some leniency's towards some of the mesh parameters such as number of adaptive passes and ΔS were taken, resulting in fields that, while still accurate, were not as accurate as they could have been. (Note: computer specs were an Intel i5-7200U processor @ 2.50GHz with 8GB of RAM)

6.3.2 In Coil Construction

The goal in coil construction was to tune and match both coils as accurately as possible not only to the 33.8MHz and 50Ω requirements, but also to each other so the comparisons between the two coils would be entirely based on geometry and nothing else, however, there were a few obstacles that prevented perfect tune and match.

- The capacitors used to tune MRI coils must not contain any ferromagnetic material such as nickel and so expensive, high quality capacitors were used. This limited the options for the values of the capacitance at each break which in turn made it more challenging to tune and match as accurately as possible.
- Initially the imaging phantom was going to be a saline IV bag and this posed as a matching problem because it loaded the coils differently every time (due to it's varying geometry).

- As mentioned in Section 4.2, the coaxial cable should be $\lambda/2$ in length to avoid affecting the tune and match, however a 15 foot cable is too long to implement in the MRI and so a smaller cable was chosen and this resulted in a shift in the resonant frequency.

6.3.3 In Sequence Implementation

Pulse sequences design and implementation was not the focus of the project and so the decisions around the pulse sequences were made out of necessity and chosen for ease of implementation rather than performance. Even still, there were some challenges when trying to get some of the sequences to work, as well as functional limitations due to the chosen sequences.

- The field produced by a surface coil is intrinsically heterogeneous which means when trying to implement the MNS prescan, the sequence would never converge on a TG. This is because an increase in power would just move the 90° flip further away from the coil but the signal from the FOV would always be increasing. The default state on the prescan is to use a hard pulse. However once switching to a slice selective soft pulse the prescan was able to converge on a TG.

- The default FOV of the B_1^+ mapping sequence was too large to get a readable resolution of the produced field. As surface coils tend to produce a field that decays away after a radius (if 90° is at the coil plane) the result would correspond to a field under 5cm in size in a 24cm FOV. A new spiral trajectory had to be designed in order to reduce the FOV to a more reasonable 15cm. However, a reduction in FOV lengthened the scan time which is not desired in a UTE sequence. To compensate, the number of acquired data points was reduced and so the number of pixels in the reconstructed data had to go from 100x100 to 80x80.

- As mentioned, the receive bandwidth on the 3D radial sequence was fixed and so the ideal way to test BW homogeneity was not possible and so some modifications had to be made to the experiment resulting in a less reliable metric.

6.3.4 In Imaging

The biggest challenge when it came to imaging was what was being imaged, whether it be a phantom or a piece of anatomy.

- As previously mentioned the first choice of phantom was of a saline IV bag. However this did not work consistently as it would load the coils

differently with each use. Also the IV bag was too small to allow for the full FOV of the coils to be imaged. The standard phantom for sodium imaging tends to be a box filled with agar gel and a sodium additive. This could not be accomplished due [recent] lab access restrictions. So it was found that lime Jello (Kraft Foods Global, Inc. Northfield IL, USA) worked well enough as a sodium imaging phantom (95mg NACl per 125mL). It turns out, while good for imaging, the jello did not provide enough signal for the B_1^+ mapping, and so the final saline phantom was created: a sealed box with 0.9% wt/v saline.

- The knee did not load the coils as intended which resulted in less signal than in a case of ideal loading. This played a major role in a wrist imaging experiment run, where the match was so bad that the signal was completely hidden in the noise and the images could not be used. It should be noted that proton coils are tuned and matched with phantoms in the factory and not subsequently altered. Even though a wide variety of anatomy is used in these clinical coils the signal strength is so high there is no complicating issue around inaccuracy with loading and tune and match. These coils are 'good enough' for clinical use. Because X-nuclei have so little signal they would be ideally tuned and matched, while inside the MRI, to the anatomy of interest. This, although doable, was beyond the scope of this thesis.

- Initially it was thought that a proton knee coil could be used in conjunction with the sodium surface coil to get a better reference proton image of the knee, however the MRI would not allow for the knee coil to be used when the sodium T/R switch was connected, and so the body coil needed to be used for the reference proton image. This made it quite difficult to match up the sodium scan FOV exactly with the proton one making it harder for registration in post-processing and analysis. This limitation was that of the MRI. A "fix" likely exists but was beyond the scope of the work presented.

6.3.5 In Experimental Data Analysis

The challenges with data analysis mostly stemmed from restrictions arising from sequence parameters.

- Because the B_1^+ mapping sequence required a slice thickness of 10mm to obtain enough signal to produce a reasonable B_1^+ map, there was not a good way to get a high enough resolution in all directions for a volume ROI to do analysis on, and a 2D plane had to suffice.

- Even with a 10mm slice and a NEX of 150, the B_1^+ mapping sequence produced very noisy images and as can be seen in Figures 5.8 and 5.9, by slice three (which was a coronal slice 35mm away from the coil) the B_1^+ map was just noise. This lead to an unreliable metric to compare field strength and homogeneity and another method needed to be used: the 3D imaging sequence.

- The challenge with the 3D imaging sequence was it produced low resolution images at only 48x48x48 in size and so Figures 5.10 through 5.12 created to compare to simulation were not on the same spatial resolution as simulation and some of the smaller ROIs could not be produced.

- The geometric phantom used in one of the BW experiments had a low sodium concentration of 15mM in it which resulted in quite low signal which made analysis and comparison quite difficult due to the low SNR.

- The noise played a role in geometric image comparisons too. A published method for image comparison based on structural similarity by Wang *et al.* [36] could not be implemented due to poor image quality.

- Because the proton knee slices and the sodium knee slices had different thicknesses, registration was far from perfect. Along with the lack of distinct features in the sodium images, only a three degrees of freedom translation (in x, y, and z) could be done and so the potential yaw, pitch, and roll of the images could not be corrected for. Motion, which would have broadened the image point spread function (PSF) could also not be accounted for. This made the sodium overlays on the proton reference images less than ideal. Quantitative analysis could not be reliably performed and as such was used more so to give context to what the sodium images were representing.

Bibliography

[1] Michel Burnier. *Sodium in Health and Disease*. New York: Informa Healthcare, 2008. 457 pp. ISBN: 978-0-8493-3978-3.

[2] Guillaume Madelin and Ravinder R. Regatte. "Biomedical applications of sodium MRI in vivo: Biomedical Applications of Sodium MRI". In: *Journal of Magnetic Resonance Imaging* 38.3 (Sept. 2013), pp. 511–529. DOI: 10.1002/jmri.24168.

[3] Donald Voet, Judith G Voet, and Charlotte W Pratt. *Fundamentals of Biochemistry: Life at the Molecular Level*. Hoboken, New Jersey: John Wiley & Sons, Inc., 2014. ISBN: 978-0-471-72085-0.

[4] Elizabeth Murphy and David A. Eisner. "Regulation of Intracellular and Mitochondrial Sodium in Health and Disease". In: *Circulation Research* 104.3 (Feb. 2009), pp. 292–303. DOI: 10.1161/CIRCRESAHA.108.189050.

[5] A M Rose and R Valdes. "Understanding the sodium pump and its relevance to disease". In: *Clinical Chemistry* 40.9 (Sept. 1994), pp. 1674–1685. DOI: 10.1093/clinchem/40.9.1674.

[6] Bernhard Gruber et al. "RF Coils: A Practical Guide for Nonphysicists". In: *Journal of Magnetic Resonance Imaging* 48 (2018), pp. 590–604. DOI: 10.1002/jmri.26187.

[7] Malcolm H Levitt. *Spin Dynamics: Basics of Nuclear Magnetic Resonance*. West Sussex, UK: John Wiley & Sons, Inc., 2013. ISBN: 978-0-470-54784-7.

[8] E. Mark Haacke et al. *Magnetic resonance imaging: physical principles and sequence design*. Second edition. Hoboken, New Jersey: John Wiley & Sons, Inc, 2014. 1 p. ISBN: 978-1-118-63397-7 978-1-118-63398-4.

[9] Donald W McRobbie et al. *MRI From Picture to Proton*. 2nd. New York, New York: Cambridge University Press, 2003. ISBN: 978-0-521-86527-2.

[10] Matt A. Bernstein, Kevin Franklin King, and Ziaohong Joe Zhou. *Handbook of MRI pulse sequences*. Amsterdam ; Boston: Academic Press, 2004. 1017 pp. ISBN: 978-0-12-092861-3.

[11] Joel Mispelter, Mihaela Lupu, and Andre Briguet. *NMR Probeheads for Biophysical and Biomedical Applications*. London, UK: Imperial College Press, 2015. ISBN: 978-1-84816-662-2.

[12] David M Pozar. *Microwave Engineering*. Hoboken, New Jersey: John Wiley & Sons, Inc., 2011. ISBN: 978-0-470-63155-3.

[13] Herman J. C. Berendsen and Hommo T. Edzes. "The Observation and General Interpretation of Sodium Magnetic Resonance in Biological Material". In: *Annals of the New York Academy of Sciences* 204.1 (Mar. 1973), pp. 459–485. DOI: 10.1111/j.1749-6632.1973.tb30799.x.

[14] Greg J. Stanisz et al. "T1, T2 relaxation and magnetization transfer in tissue at 3T". In: *Magnetic Resonance in Medicine* 54.3 (Sept. 2005), pp. 507–512. DOI: 10.1002/mrm.20605.

[15] Jolanda M. Spijkerman et al. "T2 mapping of cerebrospinal fluid: 3T versus 7T". In: *Magnetic Resonance Materials in Physics, Biology and Medicine* 31.3 (June 2018), pp. 415–424. DOI: 10.1007/s10334-017-0659-3.

[16] Rachel W. Chan et al. "Temporal stability of adaptive 3D radial MRI using multidimensional golden means". In: *Magnetic Resonance in Medicine* 61.2 (Feb. 2009), pp. 354–363. DOI: 10.1002/mrm.21837.

[17] Ernesto Staroswiecki et al. "In vivo sodium imaging of human patellar cartilage with a 3D cones sequence at 3 T and 7 T". In: *Journal of Magnetic Resonance Imaging* 32.2 (July 2010), pp. 446–451. DOI: 10.1002/jmri.22191.

[18] Frank Riemer et al. "Sodium (23Na) ultra-short echo time imaging in the human brain using a 3D-Cones trajectory". In: *Magnetic Resonance Materials in Physics, Biology and Medicine* 27.1 (Feb. 2014), pp. 35–46. DOI: 10.1007/s10334-013-0395-2.

[19] A Dutt and V Rokhlin. "Fast Fourier Transforms for Nonequispaced Data". In: (1993), p. 26.

[20] Benoit B Mandelbrot. *Fractal Geometry of Nature*. New York, New York: W. H. Freeman, 1983. ISBN: 978-0-7167-1186-5.

[21] N. Cohen. "Fractal antenna applications in wireless telecommunications". In: *Professional Program Proceedings. Electronic Industries Forum of New England*. Professional Program Proceedings. Electronic Industries Forum of New England. Boston, MA, USA: IEEE, 1997, pp. 43–49. ISBN: 978-0-7803-3987-3. DOI: 10.1109/EIF.1997.605374.

[22] Nathan Cohen. "Tuning Fractal Antennas and Fractal Resonators". Pat. 6,104,349. Aug. 2000.

[23] Hans Lauwerier and Sophia Gill-Hoffstadt. *Fractals: Endless Repeated Geometrical Figures*. Princeton, NJ: Princeton University Press, 1991. ISBN: 978-0-691-02445-5.

[24] Seunghoon Ha, Orhan Nalcioglu, and Werner W Roeck. "Fractal RF Coils for Magnetic Resonance Imaging". U.S. pat. 2015/0048828 A1. Feb. 2015.

[25] Olga M Dona Lemus, Norman B Konyer, and Michael D Noseworthy. "Micro-strip Surface Coils Using Fractal Geometry for 129Xe Lung Imaging Applications". In: *ISMRM Annual Meeting Proceedings*. ISMRM. June 2018, p. 2. URL: http://archive.ismrm.org/2018/1713.html.

[26] *Electronics Desktop HFSS*. Version R19.2. 2018.

[27] Klaus-Jürgen Bathe. *Finite Element Procedures*. 2nd ed. Englewood Cliffs, N.J: Prentice-Hall, 2014. 1043 pp. ISBN: 978-0-9790049-5-7.

[28] KiCad Developers Team. *KiCad*. Version 5.1.4. 2019.

[29] Rolf F. Schulte et al. "Transmit gain calibration for nonproton MR using the Bloch-Siegert shift". In: *NMR in Biomedicine* 24.9 (Nov. 2011), pp. 1068–1072. DOI: 10.1002/nbm.1657.

[30] Laura I. Sacolick et al. "B1 mapping by Bloch-Siegert shift". In: *Magnetic Resonance in Medicine* 63.5 (May 2010), pp. 1315–1322. DOI: 10.1002/mrm.22357.

[31] F. Bloch and A. Siegert. "Magnetic Resonance for Nonrotating Fields". In: *Physical Review* 57.6 (Mar. 1940), pp. 522–527. DOI: 10.1103/PhysRev.57.522.

[32] P.J. Beatty, D.G. Nishimura, and J.M. Pauly. "Rapid gridding reconstruction with a minimal oversampling ratio". In: *IEEE Transactions on Medical Imaging* 24.6 (June 2005), pp. 799–808. DOI: 10.1109/TMI.2005.848376.

[33] *MATLAB*. Version R2018b. 2018.

[34] John O. de Lorge. "Operant behavior and colonic temperature of Macaca mulatta exposed to radio frequency fields at and above resonant frequencies". In: *Bioelectromagnetics* 5.2 (1984), pp. 233–246. DOI: 10.1002/bem.2250050211.

[35] Government of Canada. *Limits of human exposure to radiofrequency electromagnetic energy in the frequency range from 3 kHz to 300 GHz*. Place of publication not identified, 2015. ISBN: 978-0-660-02466-0.

[36] Z. Wang et al. "Image Quality Assessment: From Error Visibility to Structural Similarity". In: *IEEE Transactions on Image Processing* 13.4 (Apr. 2004), pp. 600–612. DOI: 10.1109/TIP.2003.819861.